Institut für Chemie
Arbeitskreis Angewandte Polymerchemie

New Inverse Opal Hydrogels as Platform for Detecting Macromolecules

Dissertation
zur Erlangung des akademischen Grades
„doctor rerum naturalium" (Dr. rer. Nat.)
in der Wissenschaftsdisziplin Kolloid- und Polymerchemie

eingereicht an der
Mathematisch-Naturwissenschaftlichen Fakultät
der Universität Potsdam

von
Ing. Jean-Philippe Couturier
Potsdam, im März 2016

This work is licensed under a Creative Commons License:
Attribution – Noncommercial 4.0 International
To view a copy of this license visit
http://creativecommons.org/licenses/by-nc/4.0/

Published online at the
Institutional Repository of the University of Potsdam:
URN urn:nbn:de:kobv:517-opus4-98412
http://nbn-resolving.de/urn:nbn:de:kobv:517-opus4-98412

J’ai plus de souvenirs que si j’avais mille ans.

Un gros meuble à tiroirs encombré de bilans,
De vers, de billets doux, de procès, de romances,
Avec de lourds cheveux roulés dans des quittances,
Cache moins de secrets que mon triste cerveau.
C’est une pyramide, un immense caveau,
Qui contient plus de morts que la fosse commune.
– Je suis un cimetière abhorré de la lune,
Où comme des remords se traînent de longs vers
Qui s’acharnent toujours sur mes morts les plus chers.
Je suis un vieux boudoir plein de roses fanés,
Où gît tout un fouillis de modes surannées,
Où les pastels plaintifs et les pâles Boucher,
Seuls, respirent l’odeur d’un flacon débouché.

Rien n’égale en longueur les boiteuses journées,
Quand sous les lourds flocons des neigeuses années
L’ennui, fruit de la morne incuriosité,
Prend les proportions de l’immortalité.
– Désormais tu n’es plus, ô matière vivante !
Qu’un granit entouré d’une vague épouvante,
Assoupi dans le fond d’un Saharah brumeux ;
Un vieux sphinx ignoré du monde insoucieux,
Oublié sur la carte, et dont l’humeur farouche
Ne chante qu’aux rayons du soleil qui se couche.

– Charles Baudelaire (1821-1867)

To my parents…, and to my friends…, who never left me, in spite of the travel.

Acknowledgements

First of all I would like to thank Prof. Fink for having let me carry out my PhD at the Fraunhofer Institute for applied polymer science (IAP). More generally, I thank all the coworkers of the department of Prof. Laschewsky. I also greatly thank my "*Doctor-chef*", Prof. Laschewsky, for being a great idea-catalyst, for his guidance but also the freedom he gave me all long my thesis. This obliges me to follow my own ideas, to face my own problems, and to solve them on my own. All of that, by being present, and all the time by opening my mind to more complex problems, and the necessity in science to have a board view of problems. I thank him for his confidance all long my thesis and the opportunities he gave me to present my results on international conferences. Additionally, I thank him for its erudition that often led to fascinating (non-scientifically) related discussion. Moreover, I would like to thank Dr. Wischerhoff, head of the department "*Materials for Life Science*" (FB 4.1) also for its supervision, particularly at the beginning of my thesis, but also for the freedom he gave me, once he judged me autonomous.

I would like to thank all the amazing peoples I had the chance to meet. All my colleges, without them, I could have not found the strength to continue. Thanks to Jens and Martin, who introduced me to polymer hydrogels, without who I might have survived only a couple of hours in the lab. Thank Frank, Robert, Jonas, Eric, Viet, Noverra and Laura for being so nice all this hours. Thanks to Sandor, who helped me to learn "*Hochbayerische*", and also who made the lab work pleasant. Thanks for him for having helped me all the time even outside of the lab. Thanks to Anne, who distracted me when I was in the office. Basically thanks to both of you that gave me the impression of having German big brother and sister.

A particular big thank to Robert N., who first was a pleasant project partner, and later became a friend, who always tried to find the words to convince me that "*bad*" results were actually "*good*".

I also thank Gergana, your company really help me, notably during the final step of my thesis.

I would like to thank too particularly, Clara for her daily pleasant mood. Thanks for being so sunny, with you around even Golm looks like Italy. I have particular think for Sandra, my soul mate, and my small lab-sister. I would like to thank her for pushing me to German and to Italian classes, for listening to me complaining in the bad days, and celebrating glory ones. Thanks, for enjoying old French songs without complaining, for your help and your comments in this thesis.

More generally I sincerely would like to thank all the peoples I met during this amazing parenthesis. I actually did not completely realized the chance it was to meet all of you, but now that I am at the autumn of my studies, I realize that the most precious thing I gained during this times, was our memories.

J'ai une pensée toute particulière pour mes camarades d'internat du lycée Lavoisier, sans doute, est-ce là que tout a commencé. Lucas, Julien, Fabien, je vous remercie pour ces années passées et celles à venir.

Je remercie également mes parents et mon frère, pour m'avoir soutenu toutes ces années. Si j'ai d'une certaine manière été un bon fils, ce ne fut pas difficile avec des parents comme eux.

Je dédie cette monographie à celle sans qui je ne serais pas devenu celui que je suis. Par delà les années, par delà le voyage, son souvenir n'a cessé de peupler ma mémoire. De Mulhouse à Potsdam en passant par Lille, elle est ma seule explication, la seule de mes réponses à toutes mes questions.

Abstract

In this thesis, a route to temperature-, pH-, solvent-, 1,2-diol-, and protein-responsive sensors made of biocompatible and low-fouling materials is established. These sensor devices are based on the sensitive modulation of the visual band gap of a photonic crystal (PhC), which is induced by the selective binding of analytes, triggering a volume phase transition.

The PhCs introduced by this work show a high sensitivity not only for small biomolecules, but also for large analytes, such as glycopolymers or proteins. This enables the PhC to act as a sensor that detects analytes without the need of complex equipment. Due to their periodical dielectric structure, PhCs prevent the propagation of specific wavelengths. A change of the periodicity parameters is thus indicated by a change in the reflected wavelengths. In the case explored, the PhC sensors are implemented as periodically structured responsive hydrogels in form of an inverse opal.

The stimuli-sensitive inverse opal hydrogels (IOHs) were prepared using a sacrificial opal template of monodispersed silica particles. First, monodisperse silica particles were assembled with a hexagonally packed structure *via* vertical deposition onto glass slides. The obtained silica crystals, also named colloidal crystals (CCs), exhibit structural color. Subsequently, the CCs templates were embedded in polymer matrix with low-fouling properties. The polymer matrices were composed of oligo(ethylene glycol) methacrylate derivatives (OEGMAs) that render the hydrogels thermoresponsive. Finally, the silica particles were etched, to produce highly porous hydrogel replicas of the CC. Importantly, the inner structure and thus the ability for light diffraction of the IOHs formed was maintained.

The IOH membrane was shown to have interconnected pores with a diameter as well as interconnections between the pores of several hundred nanometers. This enables not only the detection of small analytes, but also, the detection of even large analytes that can diffuse into the nanostructured IOH membrane.

Various recognition unit – analyte model systems, such as benzoboroxole – 1,2-diols, biotin – avidin and mannose – concanavalin A, were studied by incorporating functional comonomers of benzoboroxole, biotin and mannose into the copolymers. The incorporated recognition units specifically bind to certain low and high molar mass biomolecules, namely to certain saccharides, catechols, glycopolymers or proteins. Their specific binding strongly changes the overall hydrophilicity, thus modulating the swelling of the IOH matrices, and in consequence, drastically changes their internal periodicity. This swelling is amplified by the thermoresponsive properties of the polymer matrix. The shift of the interference band gap due to the specific molecular recognition is easily visible by the naked eye (up to 150 *nm* shifts).

Moreover, preliminary trial were attempted to detect even larger entities. Therefore anti-bodies were immobilized on hydrogel platforms *via* polymer-analogous esterification. These platforms incorporate comonomers made of tri(ethylene glycol) methacrylate end-functionalized with a carboxylic acid. In these model systems, the bacteria analytes are too big to penetrate into the IOH membranes, but can only interact with their surfaces. The selected model bacteria, as *Escherichia coli*, show a specific affinity to anti-body-functionalized hydrogels. Surprisingly in the case functionalized IOHs, this study produced weak color shifts, possibly opening a path to detect directly living organism, which will need further investigations.

Zusammenfassung

Periodisch strukturierte, funktionelle responsive Hydrogel wurden in Form von inversen Opalen (IOH) aufgebaut und als Basiselement für Temperatur-, pH-, lösungsmittel-, 1,2-diol- oder protein-sensitive Sensorsysteme entwickelt. Dazu wurden aus biokompatiblen Bausteinen funktionelle photonische Kristalle aufgebaut, deren optische Bandlücke durch selektive Bindung eines Analyten moduliert wird, indem dieser einen Volumen-Phasenübergang induziert. Mittels solcher responsiver photonische Kristalle ist es möglich, Analyte ohne aufwendige Geräte durch Farbänderung einfach zu detektieren. Die entwickelten Systeme zeigen nicht nur eine hohe Empfindlichkeit gegenüber kleinen Biomolekülen, sondern auch gegenüber größeren Analyten wie z.B. Glycopolymeren und Proteinen, was bisher nicht bekannt war.

Die stimuli-sensitiven inversen Opal Hydrogele (IOHs) wurden in mehreren Stufen hergestellt. Als erstes wurden dafür kolloidale Kristalle mit hexagonal gepackten Strukturen aus monodispersen SiO_2-Partikeln auf Glasträgern aufgebaut ("Opal"). Die Opale mit charakteristischen Strukturfarben wurden anschließend in eine polymere Hydrogelmatrix eingebettet. Diese wurde aus Oligo(ethylenglycol)methacrylaten (OEGMAs) hergestellt, so dass die Hydrogele sowohl thermosensitives als auch "low-fouling" Verhalten zeigen. Im letzten Schritt wurden die SiO_2-Partikel entfernt und so eine hochporöse Hydrogel-Replika der Opale erhalten unter Erhalt deren innerer Struktur und Strukturfarbe. Die miteinander verbunden Poren der IOH Membran besitzen einen Durchmesser von einigen hundert Nanometern. Dies ermöglichte nicht nur die Detektion von kleinen Analyten, sondern auch die Detektion von deutlich größeren, makromolekularen Analyten, die ebenfalls in die Nanostrukturen der IOH Membran diffundieren können.

Modellsysteme bestanden immer aus einer Erkennungsgruppe und einem Analyten, beispielsweise aus Benzoboroxol – 1,2-Diol, Biotin – Avidin und Mannose – Lectin (Concanavalin A). Für diese Modellsysteme wurden OEGMAs mit Monomeren copolymerisiert, die mit Benzoboroxol, Biotin bzw. Mannose funktionalisiert waren. Die so im Polymer eingebauten Erkennungsgruppen binden spezifisch an bestimmte Biomoleküle unterschiedlicher Molmassen, wie z.B. niedermolekulare Saccharide oder Catechin, als auch hochmolekulare Glycopolymere oder Proteine. Der spezifische

Bindungsvorgang moduliert die Gesamthydrophilie, so dass sich der Quellgrad der IOH-Matrix ändert. Dies wiederrum verändert die innere Periodizität und damit die Strukturfarbe. Dabei wird der Quelleffekt durch die Thermosensitivität der Hydrogele massiv verstärkt. Eine spezifische Molekülanbindung lässt sich so optisch, z.T. sogar mit dem Auge, erkennen aufgrund der deutlichen Verschiebung der Strukturfarbe um bis zu 150 *nm*.

Des Weiteren wurden auch erste Versuche zur Detektion von noch größeren Analyten unternommen. Dafür wurden Antiköper durch nachträgliche Modifizierung der Polymerseitenketten auf den Hydrogeloberflächen immobilisiert. Mit diesem Modellsystem konnten unterschiedliche Bakterienarten durch Antikörper spezifisch gebunden werden. Die verwendeten Bakterienarten sind zwar zu groß, um in die Membran des IOH Systems einzudringen, können jedoch mit der IOH-Oberfläche wechselwirken. Insbesondere das Modellsystem mit Escherichia coli zeigte eine starke, spezifische Affinität zu dem Antikörper-funktionalisierten IOH. Überraschenderweise zeigte sich bei den Versuchen in Gegenwart des Analyten eine kleine Farbänderung der funktionalisierten IOH. Damit eröffnet sich u.U. die Möglichkeit, mit solchen responsiven photonischen Kristallen auch lebende Organismen spezifisch und einfach zu detektieren, was in weiterführenden Arbeiten zu klären sein wird.

List of Abreviations

a_0	length of the edge of a cube
Abs.	absorbance
AcA	acrylic acid
AFM	atomic force microscopy
a_{hkl}	interplanar distance
AIBN	2,2'-azobisisobutyronitrile
APF	atomic packing factor
bcc	body-centered cubic
BHT	2,6-di-*tert*-butyl-4-methylphenol
biotin-MA	biotin methacrylate
biotin-NHS	biotinyl-N-hydroxysucinimide ester
boroxol-	benzoboroxole
MAm	methacrylamine
BSA	bovine serum albumine
C	concentration
C_0	silicic acid concentration where the nucleation stop
C_N	silicic acid concentration where the nucleation start
C_n	characteristic constant
C_S	silicic acid solubility
CC	colloidal crystal
ConA	concanavalin A
CP	cloud point
cryo-SEM	cryogenic scanning electron microscopy
χ	effective crosslinker content
d	diameter of particles
d_{C-C}	length of C-C bond
d_s	distance between two surfaces
D	diffusion coefficient
DLS	dynamic light scattering
DMF	N,N-dimethylformamide
DMSO	dimethyl sulfoxide
DSC	differential scanning calorimetry
δ	chemical shift
δ_t	total cohesion (solubility) parameter
δ_d	dispersion cohesion (solubility) parameter
δ_p	polar cohesion (solubility) parameter
δ_h	hydrogen bonding cohesion (solubility) parameter
ΔCP	cloud point difference
ΔG_{mix}	free enthalpy of mixing
ΔH_{mix}	enthalpy of mixing
ΔS_{mix}	entropy of mixing
dn	refractive index contrast
η	viscosity
fcc	face-centered cubic
FWHM	full width at half maximum
$G(q;\tau)$	intensity-correlation function
H-	non-structured hydrogel
hcp	hexagonal close-packed
HEMA	2-hydroxyethyl methacrylamide
hkl	Miller-indexes
HLB	hydrophilic-lipophilic balance
I	light intensity
IOH / **IOH-**	inverse opal hydrogel
IR	infra-red (light)

List of Abreviations

J	coupling constant
k	Boltzmann's constant
LCST	lower critical solution temperature
LSM	laser scanning microscopy
λ	wavelength
m	mass
$m_{\mathbb{N}}$	a natural number
mannose-A	acetylated mannose acrylate
MEOMA	ethylene glycol methylether methacrylate
MEO_2MA	di(ethylene glycol) methylether methacrylate
MEO_3MA	tri(ethylene glycol) methylether methacrylate
M_n	molar mass in number
M_n^{app}	apparent molar mass in number
M_w	molar mass in weight
M_w^{app}	apparent molar mass in weight
n	refractive index
NiPAm	N-isopropylacrylamide
NMR	nuclear magnetic resonance spectroscopy
OEG	oligoethylene glycol
OEGDMA	oligoethylene glycol dimethacrylate
OEGDMA550	oligoethylene glycol dimethacrylate (M_n= 550 $g{\cdot}mol^{-1}$)
OEGMA	oligoethylene glycol methylether methacrylate
OEGMA300	oligoethylene glycol methylether methacrylate (M_n= 300 $g{\cdot}mol^{-1}$)
OEGMA475	oligoethylene glycol methylether methacrylate (M_n= 475 $g{\cdot}mol^{-1}$)
OP-	silica opal
P-	linear polymer
PBS	phosphate buffered saline
PEG	polyethylene glycol
PhC	photonic crystal
PMA	maltopentaose
P-MEO_2MA-co-OEGMA475	poly(di(ethylene glycol) methylether methacrylate-co-oligoethylene glycol methylmethacrylate)
PMMA	poly(methylmethacrylate)
P-NiPAm	poly(N-isopropylacrylamide)
P-NiPMAm	poly(N-isopropylmethacrylamide)
P-OEGMA	poly(oligoethylene glycol methylether methacrylate)
PS	polystyrene
PVA	poly(vinyl alcohol)
P-VCL	poly(N-vinyl-ϵ-caprolactam)
P-VME	poly(vinylmethylether)
PXM-1	glycopolymer derived xylitol and N-methylmaleimide
PXM-2	glycopolymer derived xylitol and N-ethylmaleimide
PXM-3	glycopolymer derived xylitol and N-phenylmaleimide
φ	volume fraction
ϕ_{hkl}	angle between the plane (hkl) and the plane (111)
q	wave scattering vector
r^2	coefficient of determination
R_h	hydrodynamic radius
SD_{abs}	absolut standard deviation
SD_{rel}	relative standard deviation

SEC	size exclusion chromatography
SEM	scanning electron microscopy
SiO_2-	silica particles
SR	swelling ratio
t	time
T	temperature
$T_{1/2}$	temperature at half transmittance
TEOS	tetraethyl orthosilicate
TMS	tetramethylsilane
Trans	transmittance
τ	time difference
θ	light angle
UCST	upper critical solution temperature
UV	ultra-violet (light)
UV-vis	ultra-violet - visible (light)
V	volume
V_A	attractive van der Waals potential
V_R	repulsive electrostatic potential
ξ	mesh size

Contents

Acknowledgements **i**

Abstract (English/Deutsch) **iii**

List of Abreviations **vii**

1 Introduction **1**
1.1 Butterfly and Peacock Wings 1
1.2 Opals 3
1.3 Inverse Opals 4
1.4 Structural Color Modulation 5
1.5 Aim and Outline 6

2 Silica Particles **11**
2.1 Pyrogenic/Fumed Silica 12
2.2 Precipitation from Water Glass 13
2.3 Stöber Process 13
  2.3.1 LaMer Model 16
  2.3.2 Coagulative Mechanism 17
2.4 Stability of the Particles 17
2.5 Dynamic Light Scattering 19
2.6 Conversion 21
2.7 Synthesis of Stöber Particles 22

3 Silica Opals **27**
3.1 Assembly 27
3.2 Structural Color 31
  3.2.1 Structure 31
  3.2.2 Scattering and Diffraction 33
3.3 UV-vis Spectroscopy 35
3.4 Vertical Deposition Assembly 36
3.5 Electron Microscopy 39

3.6 Atomic Force Microscopy 41
3.7 Light Interference 43

4 Linear Polymers and Hydrogels 49
4.1 Thermoresponsive Polymers 49
4.2 Energetic Considerations 50
4.3 Classical Thermoresponsive LCST-type Polymers 54
4.4 LCST Determination 56
4.4.1 Turbidity Measurement 57
4.4.2 Swelling Ratio 58
4.5 Thermoresponsive Polymers as Analyte Sensor 59
4.6 Functional Recognition Unit Monomers 61
4.6.1 Benzoboroxole – 1,2-Diols 61
4.6.2 Biotin – Avidin 62
4.6.3 D-Mannose – Concanavalin A 64
4.7 Linear Copolymers 65
4.7.1 Analyte Tests 68
4.8 Hydrogels 75
4.8.1 Synthesis 75
4.8.2 Swellability and Mechanical Stability 77
4.8.3 Functionalized Hydrogels 80

5 Inverse Opal Hydrogels 83
5.1 Opal *vs.* Inverse Opal 83
5.2 Synthesis 85
5.3 Cryo-SEM Characterization 87
5.4 UV-vis Spectroscopy Analysis 89
5.4.1 non-Functionalized IOH 90
5.4.2 Functionalized IOH 93

6 Further Systems 107
6.1 Anti-Bodies Immobilization on Hydrogel Surfaces 107
6.2 Anti-Body – Bacteria as Model Systems for IOH 110

7 Summary and Conclusion 115

8 Experimental Part 117

8.1 Chemicals . . . 117
8.2 Methods . . . 119
  8.2.1 UV-vis Spectroscopy . . . 119
  8.2.2 Turbidimetry . . . 119
  8.2.3 Dynamic Light Scattering . . . 119
  8.2.4 Atomic Force Microscopy . . . 120
  8.2.5 Scanning Electron Microscopy . . . 120
  8.2.6 Laser Scanning Microscopy . . . 121
  8.2.7 Optical Microscopy . . . 121
  8.2.8 Size Exclusion Chromatography . . . 121
  8.2.9 NMR Spectroscopy . . . 121
  8.2.10 Mass Spectrometry . . . 122
  8.2.11 Elemental Analysis . . . 122
8.3 Synthesis of Silica Nanoparticles . . . 122
8.4 Assembly of Silica Opals . . . 123
8.5 Synthesis of Functional Monomers . . . 124
  8.5.1 Benzoboroxole Methacrylamide . . . 124
  8.5.2 Biotin Methacrylate . . . 124
  8.5.3 Mannose Acrylate . . . 125
8.6 Synthesis of Polymers . . . 126
8.7 Synthesis of Hydrogels and Inverse Opal Hydrogels . . . 128
8.8 Preparation of the Cell Cultures . . . 132
  8.8.1 *Escherichia Coli* and *Pseudomonas Putida* . . . 132
  8.8.2 *Salmonella Thyphimurium* . . . 132

A NMR Spectra I

B Solubility Parameters VII

List of Figures IX

List of Tables XIX

List of Publications XXI

Declaration XXV

Bibliography XXXVIII

1 Introduction

1.1 Butterfly and Peacock Wings

Structural color has arisen scientific interest for centuries. Such a coloration involves selective reflectance of incident light provoked by the particular object's structure in contrast to classical pigment and dye based colors, which are due to an energetical consumption of selective wavelengths. In 1665, Hooke revealed in his famous book "*Micrographia*" the structure of the feathers of peacocks and ducks.[1] Yet, it was necessary to wait until the achievement of the electron microscope to study precisely the complex microstructure of feathers of *ivory-breasted pitta* or the dorsal wings of *Morpho* butterflies.[2, 3] Examples of structural color have been present in the nature since long, resulting from millions of years of evolution.[4] Nature is full of species, such as butterflies, beetles, cuttlefishes, sea mice, pigeons, and peacocks which manifest structural color. Iridescence phenomena exemplified by the dorsal wings of *Morpho* butterfly (Figure 1.1) revealed to be one of his characteristics to survive to predator birds, to mark is territory or even to arise the attention of the other sex.[5]

As early as 1665, Hooke reported that the color of the feathers of birds vanished when they were soaked into water.[1] Later, in 1730, Newton allows in "*Optiks*" to understand and explain the mechanism of iridescence in the specific case of peacock feathers.[6] It was necessary to wait until 1873 for the establishment of the electromagnetic theory by Maxwell, as well as for the work of Michelson and Rayleigh on light interference, to describe completely the properties of light.[5, 7] They confirmed by their theories the inner dependency of the resulting reflected wavelength – that in certain conditions lead to color – and the angle between the incident light and the reflecting surface. In other terms, the reflected wavelength is correlated to the orientation of the *Morpho* butterfly wings, as illustrated below (Figures 1.1a, 1.1b and 1.1e : front view and

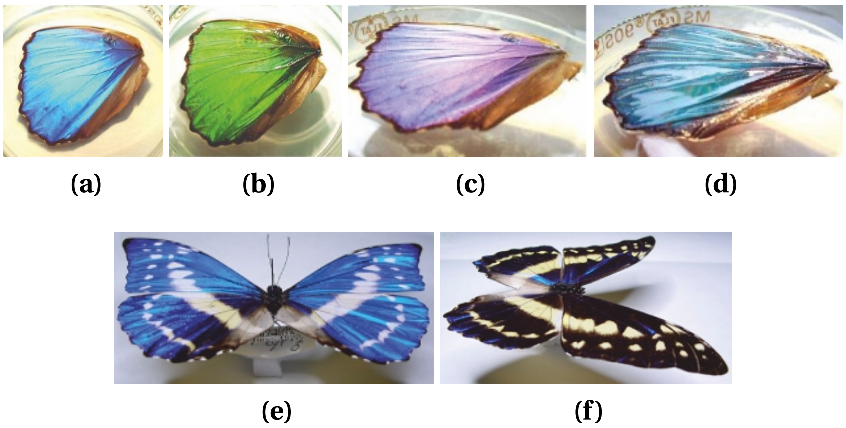

(a) (b) (c) (d)

(e) (f)

Figure 1.1: Front and oblique views of *Morpho didius* wings in different refractive index media: (a) and (c) in air (n_{air} = 1.00), (b) and (d) in ethanol ($n_{ethanol}$ = 1.36). Perpendicular (e) and parallel (f) view of *Morpho cypris* wings.[5]

Figures 1.1c, 1.1d and 1.1f: oblique view). The first observation made by Hooke in "*Micrographia*" was explained in great detail by another distinctive feature of structural color: their link with the surrounding refractive index (in air, Figures 1.1a and 1.1c and in ethanol, Figures 1.1b and 1.1d). This color produced by iridescence can also be called Bragg color. By contrast to a classical source of color such as the presence of a chromophore, the Bragg color is only due to the microarchitecture of the material. A detailed description was finally achieved in 1942 by Anderson and Richard,[2] and Gentil [3] after improvements realized in electron microscopy.
The origin of the iridescence of butterfly wings is illustrated below (Figure 1.2). Their lamellar architecture produces periodic domains with distinct dielectric constants, which create the Bragg diffracted wavelength. The periodical refractive index contrast between the lamellar material and the surrounding media (here: air) leads to interferences that provoke the disappearance of the non-coherent wavelengths and the reflection of the coherent color (see Chapter 3). The observed reflected color depends on the lamellar structure and the refractive index contrast.

In summary, this Bragg reflection phenomenon requires materials with nanoarchitectures, which provide periodic domains with distinct dielectric constants. The periodic structure is not necessarily made of lamellae, as for the butterfly wings, but can also be made, for instance, of spheres as described in the next section for the case of inorganic materials named opals.

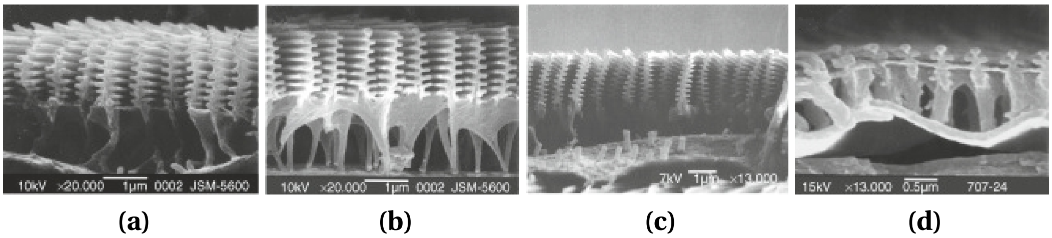
10kV ×20.000 1µm 0002 JSM-5600
10kV ×20.000 1µm 0002 JSM-5600
7kV 1µm ×13.000
15kV ×13.000 0.5µm 707-24
(a)
(b)
(c)
(d)

Figure 1.2: Scanning electron micrographs for the cross-section of ground scales of (a) *M. didus*, (b) *M. sulkowskyi*, and (c) *M. rhetenor*, and for a cover scale of (d) *M. adoni*; the bars are (a–c) 1 and (d) 0.5 μm.[8]

1.2 Opals

Opals are gemstones, that similarly to butterfly wings, exhibit a color induced by Bragg diffraction (Figure 1.3a). The mystery behind their color has always aroused people's interest. Some religious believed that these colored stones were dropped from heaven as a gift of the gods.[9] Following the great progress in microstructure determination due to the development of the electron microscopy in the 1960s, Sanders *et al.* elucidated most of the opal's shadow.[9–13]
In contrast to most of the animals' microstructures that are made of a superposition of lamellae (Section 1.1), natural opals are composed of assembled amorphous uniform spherical particles (Figure 1.3b). These particles are most commonly made of silica, but can be composed of titanium dioxide or even artificially built up with polystyrene (PS) or polymethylmethacrylate (PMMA).[14–19]

That way, the assembly of these particles leads to the apparition of a regular crystal lattice and thus of two repetitive zones with different refractive indexes: the space filled by the silica particles ($n_{\mathrm{SiO}_2} = 1.44 - 1.46$) and the void. Natural opals are partially hydrated so that their chemical structures can simply be written $\mathrm{SiO_2} \cdot x\mathrm{H_2O}$, as the silicon dioxide and as a variable amount (indicated by x) of bound molecules of water. The complexity of their fascinating color resides in different and subtle parameters such as the degree of hydration but also the crystal structure (see Chapter 3).[9]

Such materials – natural or artificial opals – are also called photonic crystals (PhCs) because of their similitude with classical atomic crystals in terms of structure, as well as their aptitude to diffract electromagnetic waves such as X-rays. Whereas atomic crystals diffract X-rays (Ångstrom scale), the size of the particles that constitute opals (hundred nanometer scale) shift the diffracted wave to the visible range of the electromagnetic spectrum. In nature, the self-organization processes that provide color to opals, are the result of long and slow deposition and sedimentation over time. This explains their rarity and their high prices, and also the thrive for new techniques to build and create artificial PhCs. This topic will be addressed in detail in Chapter 3.

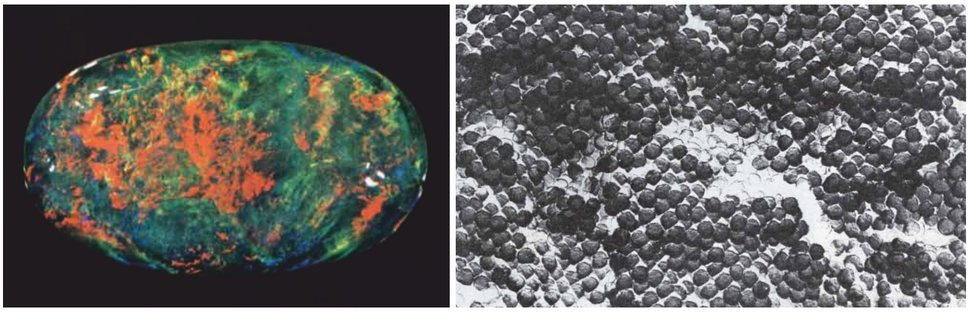

(a) **(b)**

Figure 1.3: (a) black opal photograph by John Cubitto of the Gemological Institute of America, (b) electron micrograph of the surface of a precious opal (after etching by hydrofluoric acid) made of spherically shaped particles ranging from 150 *nm* to 300 *nm* in diameter (magnifition 19,000 ×).[12]

Normally, color is produced by mechanisms such as absorption or emission of light. Most of them are due to the chemical nature of the materials that can absorb, separate or emit light. To control the color it is a priori necessary to control the chemical nature of the material and the interaction with light on the atomic or molecular level. However, the quantized exchange of energy transition limits the color possibilities, whereas structural color materials allow a broad variation of the perceived color. Because their color is directly correlated to their geometry, the possibility to tune the color is almost unlimited compared to the chemical modifications that are required in the first case. That way, PhC materials have high potential in sensors, wave-guides or pigments based on dynamic color changes.[7]

1.3 Inverse Opals

PhCs can be defined as materials containing periodic arrays of high and low dielectric zones that form photonic Bragg diffraction planes. The diffraction produced by these planes prevents the propagation of photons of specific wavelengths through the material. That way, the structure of PhCs such as opals can be inverted: the void volume can be filled by a material with a high refractive index and the silica particles could be then etched, creating the negative of the opal structure, a so called inverse opal (Figure 1.4).

As long as the lattice and a sufficient refractive index contrast — between the filled and the void volume — are respected, inverse opals act as PhCs, and so their optical properties are maintained. Moreover, if the voids are connected, inverse opals can be seen as porous membrane materials. This aspect allows them to combine the optical properties of PhCs and the high specific surface that can help the infiltration and diffusion of the medium (liquid, gas . . .) through them. Inverse opals made of hydrogel materials will be discussed in detail in the Chapter 5.

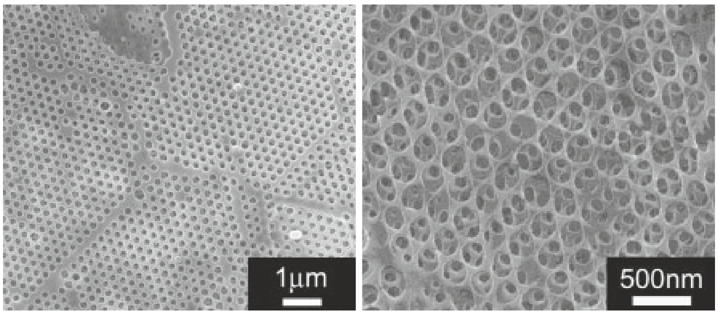

(a) **(b)**

Figure 1.4: Inverse opal hydrogel pH sensors (a) scanning electron microscope images of an inverse opal hydrogel made of acrylic acid (AcA) and 2-hydroxyethyl methacrylate (HEMA), (b) high-magnification of the same hydrogel showing the interconnected void structure.[20]

1.4 Structural Color Modulation

Nature has not finished to surprise us: some species develop the capacity to control and change their structural color on demand. Thus the fish *Paracheirodon innesi* displays a structural color of cyan produced by interference of the light on periodically stacked microplatelets of skin cells.[7, 21, 22] Under stress *Paracheiron innesi* modulates the inflow of water between its skin platelets, which increases their distance. Consequently its color turns to yellow, by change of the refractive index and also by change of the lamellar distance (Figure 1.5a). Another example of color control in nature is the beetle *Charidotella egregia*.[7, 22–24] By mastering the amount of fluid between its platelets, it can modulate the distance of the platelets and their refractive index, thus changing its color from yellow to red (Figure 1.5b).

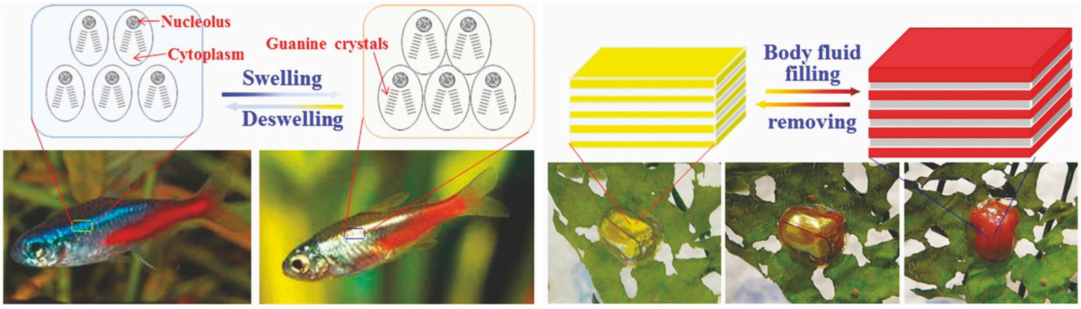

(a) (b)

Figure 1.5: Natural species with structural color modulation: (a) the fish *Paracheirodon innesi* displays normally a color of cyan, but after swelling their iridophores, its color changes to yellow,[22] (b) the beetle *Charidotella egregia* changes its color from gold to red after touching its wings, presumably to prevent predation.[23]

1.5 Aim and Outline

As mentioned before, materials with PhC structures that exhibit a Bragg color have a great potential for autonomous sensor devices. The principle for such sensors is inspired by what the nature is capable to realize. Therefore, like fish *Paracheirodon innesi* and beetle *Charidotella egregia*, the Bragg color of artificial inverse opals may be modified on demand *via* the change of their structures. These modifications can happen according to three different scenarios:

- destruction of the periodicity,
- diminution of the interplanar crystal distance (expansion of the structure),
- augmentation of the interplanar crystal distance (contraction of the structure).

In practice, these geometric modifications are translated by the disappearance of the color, or by a blue/red-shift due to the decrease/increase of the reflected wavelength.

With the perspective to build a sensor, it is indispensable to use a sufficiently flexible material to enable deformation for the color modification; often, hydrogels are used. Hydrogels consist of polymers that are cross-linked, in most cases covalently, which are highly swollen by water. Some of these polymers have shown the ability to change their volumes or their geometries by uptake or release of water upon a stimulus such as temperature, pH, solvents or gases.[25, 26] Some recent studies underlined the fact that hydrogels implemented in a form of inverse opal can be used as sensors for various stimuli. Indeed, stimulus responsive hydrogels, also called "*smart*" hydrogels, were shown to drastically shrink or swell upon a small change of environment.[25]

A great number of opal/inverse opal hydrogels have been developed as sensor devices for several stimuli, such as solvent,[27–29] temperature,[30] ions,[31, 32] pH,[20, 33] biomolecules [34–38] and pressure.[39]

Nevertheless, such simple and fast sensor systems did not exist for the detection of large molecules.[40, 41] The detection of big molecules such as proteins or macromolecules are a much greater challenge than the detection of small analytes, because of their sizes and so their limits to diffuse into the polymeric matrix. Thus, inverse opal hydrogels (IOHs) "*efficiency*" in terms of binding and volume concentration is dramatically reduced for big molecules.

In this thesis, new inverse opal hydrogels will be introduced and discussed, as autonomous diagnostic platforms not only for small molecules such as glucose, but also for large molecules as macromolecules or proteins.

More generally, this work aimed at exploring new approaches toward fast and selective diagnostic platforms for pathogen detection with an easy optical read-out, which does not require complex equipment or specifically trained operators.

The goal of this work was to give a proof of concept for inverse opal hydrogels (IOHs) made of stimulus responsive polymers, which are able to interact specifically with proteins and macromolecules to provoke a change of their reflected color. To reach this point, it was necessary to consider a polymer matrix that inhibits unspecific adsorption by choosing a polymer network with low-fouling properties.[42–44] Additionally, the polymer matrixes had to contain specific recognition units that can specifically interact with the corresponding analyte targets. The strategy of using a stimulus resposive matrix was motivated by their strong ability to drastically change their swelling properties upon a marginal variation of environment. Therefore, these properties should confer good sensitivity and selectivity to IOHs in terms of Bragg reflected wavelength variation in the presence of the target analytes.

Hydrogels with an inverse opal form were chosen against opal hydrogels due to their a priori higher porosity. Stimulus responsive materials may be more sensitive, if the molecules can easily infiltrate the material.[45] Additionally, these IOHs target to be used under physiological conditions. Accordingly, biocompatible materials were used, and analyte assays were carried out in phosphate-buffered saline.

In the following four chapters, the multistep procedure for the synthesis of the IOHs will be described and discussed subsequently. All chapters will contain their own fundamental and discussion parts, describing each step of the IOHs synthesis separately. The general procedure of the IOHs synthesis can be summarized as following (Figure 1.6):

Chapter 2	silica nanoparticle synthesis,
Chapter 3	colloidal crystal assembly,
Chapter 4	design of biocompatible stimulus responsive polymers for analyte sensing,
Chapter 5	synthesis of stimulus responsive IOHs for analyte sensing.

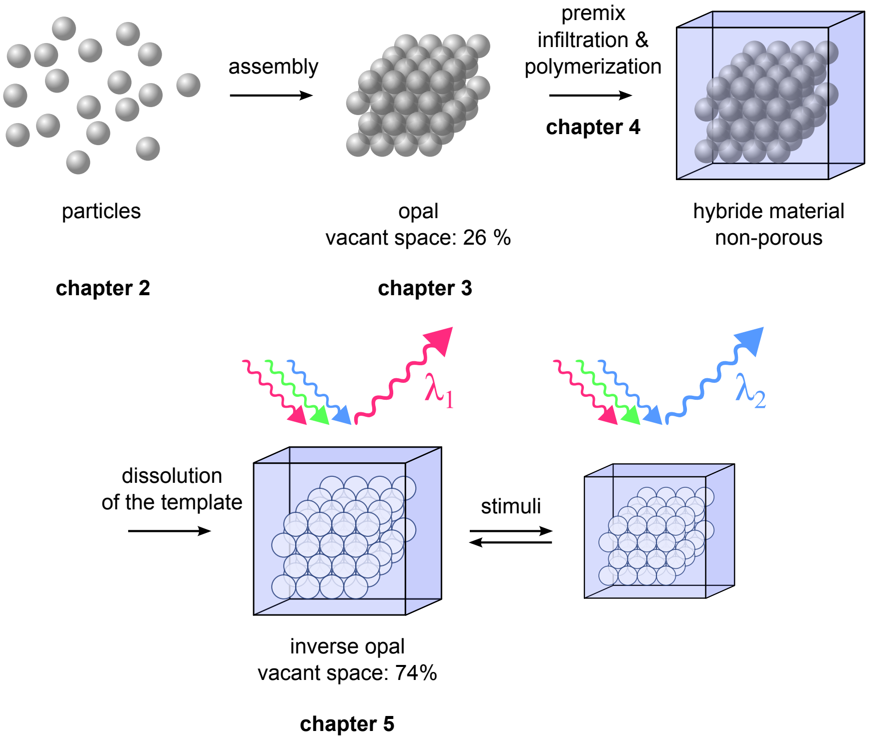
assembly
premix
infiltration &
polymerization
chapter 4
particles
opal
vacant space: 26 %
hybride material
non-porous
chapter 2
chapter 3
λ1
λ2
dissolution
of the template
stimuli
inverse opal
vacant space: 74%
chapter 5

Figure 1.6: Pathway leading to IOHs as autonomous sensor platforms.

Accordingly, the Chapter 2 is focused on the synthesis and the characterization of silica nanoparticles with low polydispersity, in order to build sacrificial opal templates for the IOHs. Chapter 3 describes the method used to self-assemble the monodisperse colloid dispersion in a face cubic centered lattice. The quality in terms of regularity and order is characterized using high resolution microscopies, such as scanning electron microscopy (SEM) and atomic force microscopy (AFM). At this step, the optical properties of the opal templates are characterized *via* UV-vis spectrometry at different incident angles.
In parallel, Chapter 4 presents the studies on the formulation of the responsive hydrogels. This chapter is subdivided onto three main sections: the synthetic part of the recognition unit monomers and the functional linear polymers, the phase transition studies of these polymers (using turbidimetry) in presence and in absence of the target analytes, and finally, the translation of these smart linear polymers from a soluble state to a crosslinked platform. Different hydrogel compositions will be presented, considering several sensitive parameters, such as the crosslinking density and thus, the degree of swellability.

Chapter 5 combines the previous results from Chapters 2 to 4 for making inverse opal hydrogels, which exhibit structural color. The structure of the IOHs is resolved *via* cryo-SEM. Finally, their surprising high sensitivity to large analytes, such as proteins or other macromolecules, is revealed *via* UV-vis spectrometry (up to 100 *nm* shifts and higher).

2 Silica Particles

The first step for building the photonic crystals is the synthesis of spherical particles with narrow size distribution. Thus, in this chapter, the synthesis of silica nanoparticles and their size characterization using dynamic light scattering (DLS) will be described. Then, Chapter 3 will describe how to assemble these silica particles onto opal to be used as template.

Requirements for nanoparticles building blocks for opals:

- regular size and form, high uniformity,
- regularly charged surface,
- high purity,
- good dispersability of the particles.

As a prerequisite for regular packing during the self-assembly of the opal crystal, it is essential to obtain uniform spherical particles. If the sizes are not uniform enough, too many defects will be formed into the crystal. In the worst case, defects can provoke the disappearance of the color due to the loss of the interference pattern.[46]

The second and the third criteria refer to the stability of the charged particles, considering the balance of *electrostatic repulsion* and *van der Waals attraction* due to the electrical double layer (charged) around the particles. The theory behind this phenomenon will be described later. If the particle solution is not pure enough, it may happen that ionic impurities disturb the charged double layer and so endanger their stability.
Finally, to obtain a regular opal film, homogenous dispersion of the particles in volatile solvents should be easy.

Since the opal is intended to be used as a template for IOHs, the nanoparticles should be stable only initially, but need to be decomposable by a treatment, which leaves the embedding hydrogel intact. For this reason, cross-linked latex particles cannot be used, because they can only be removed by calcination at high temperature, which will damage the IOHs. On the other hand, non-crosslinked organic polymer particles are easy to remove by simple dissolution in a good solvent. Yet, they may not be stable enough due to their softness, which might provoke irreversible coalescence during separation procedures such as centrifugation. Therefore, silica particles were chosen: they provide high stability, but can be selectively etched using hydrofluoric acid without damaging the organic IOHs. Moreover, silica particles can easily be synthesized with a regular shape using the Stöber process.[47] While the strong and robust properties of silica particles confer to them the ability to resist mechanical stress, *e.g.* by the centrifugation, they can be easily redispersed in solvents such as water or ethanol.

Monodisperse colloidal silica spheres are attractive materials for many fields, such as ceramics, glass making, catalysis and chromatography.[48] There exist several techniques to produce silica nanoparticles, such as pyrogenic/fumed silica, precipitation from water glass and Stöber synthesis.

2.1 Pyrogenic/Fumed Silica

The term pyrogenic silica refers to highly dispersed silicas formed from the gas phase at high temperature. The most important production process is flame hydrolysis. Other techniques such as plasma processes exist, but they are marginal. The flame hydrolysis (also named vapor-phase hydrolysis) was developed in the 1930s. Most industrial processes use silicon tetrachloride ($SiCl_4$) as raw material. The silicon precursor is continually vaporized into a flame using oxygen (O_2) and hydrolyzed by water that is produced by combustion of hydrogen (H_2) or methane (CH_4). At the outflow of the reaction chamber, the silica is expelled as aerosol.[49, 50]

$$\mathrm{SiCl_4 + 2\,H_2O \rightarrow SiO_2 + 4\,HCl}$$

Figure 2.1: Overall reaction of silicon tetrachloride hydrolysis and condensation, in the flame hydrolysis process.

2.2 Precipitation from Water Glass

Precipitated silicas have been commercially produced since 1940s from alkaline metal silicate solutions such as sodium silicate. Silica is precipitated by mixing acid, commonly sulfuric acid, hydrochloric acid or carbon dioxide, to sodium silicate to reduce the pH value. The precipitation is carried out in alkaline conditions, whereas silica gels are synthesized under acidic conditions. Moreover, stirring and the increase of the temperature of the reaction mixture avoid the formation of coherent networks such as macroscopic gels.[49, 50]

Although these techniques lead to inexpensive silica particles, they cannot be used as precursors for opal templates, as both produce particles with a too high dispersity. It is usually considered in the literature that standard deviations lower than 5% are required to obtain sufficiently ordered opal structures.[46] A common alternative to produce silica particles with a truly controlled shape and size is the so called "*Stöber process*".

2.3 Stöber Process

A widely used method for the synthesis of silica particles, developed by Stöber et al., is the hydrolysis and subsequent condensation of organoalkoxysilanes in a mixture of water and alcohol under basic conditions.[47] This process results in nearly monodisperse spherical silica particles. Therefore, the Stöber procedure is arguably the most known colloidal reaction. In literature, terms such as "*Stöber process*" or "*Stöber particles*" are commonly used referring to monodisperse silica particles made from organoalkoxysilanes in water/alcohol mixture, with ammonia as catalyst.
Whereas the experimental procedure is a priori rather simple, the mechanisms for the formation and the growth of the silica spheres are not. No general scheme has been successfully proposed yet.[51] Therefore only partial models will be presented in this chapter.

The Stöber synthesis is an inorganic reaction, where the amorphous silica particles dispersed in a liquid generally form a so-called *sol*. The dispersion is called organosol when an organic solvent is used. Analogously, the terms *aquasol* or *hydrosol* are used referring to water. The simplified overall hydrolysis and condensation reactions using tetraethyl orthosilicate (TEOS), can be respectively written as

$$n\,\mathrm{Si(OC_2H_5)_4} + 4n\,\mathrm{H_2O} \rightarrow n\,\mathrm{Si(OH)_4} + 4n\,\mathrm{C_2H_5OH}$$
$$n\,\mathrm{Si(OH)_4} \rightarrow (\mathrm{SiO_2})_n + 2n\,\mathrm{H_2O}$$

Figure 2.2: Overall reaction of TEOS hydrolysis and condensation in aqueous media.

Typically, the reaction mixture contains TEOS, ethanol, water and ammonia. While ethanol is used as a solvent for TEOS, water is employed as hydrolysis agent and ammonia as catalyst.

In more detail, the Stöber process with organoalkoxysilanes in basic conditions is generally described using three reactions: hydrolysis, alcohol condensation (alcoxolation) and water condensation (oxolation) (Figure 2.3).

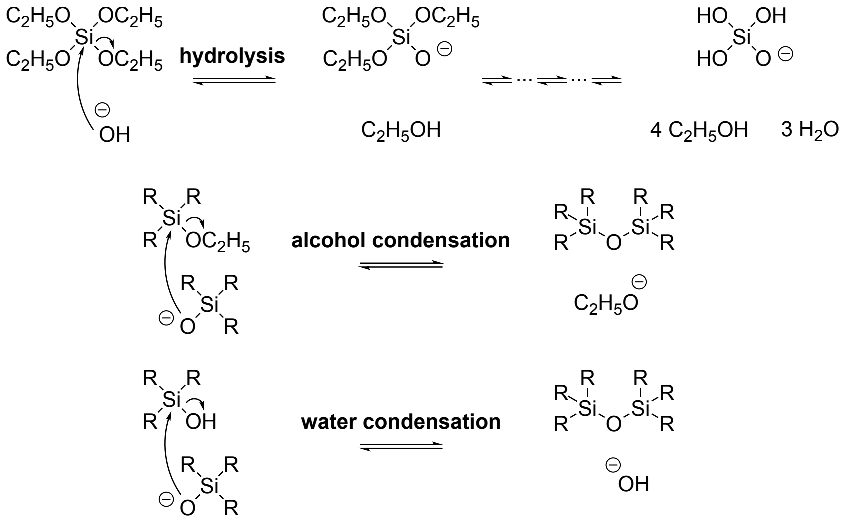

Figure 2.3: Hydrolysis and condensation mechanisms of TEOS in aqueous media under basic conditions.[52]

In the first step, under basic conditions, it is likely that water dissociates to produce hydroxyl anions. Then, TEOS is hydrolyzed by hydroxide anions *via* a nucleophilic substitution mechanism with a pentavalent transition complex as proposed by Iler.[53] For the condensation, the silanol anion attacks the silicon center of another molecule *via* nucleophilic substitution (Si-$\mathrm{SN_2}$) also generating intermediately a pentavalent complex, and finally forming a Si-O-Si bond, that results in the silica network.[52]

We first depict the hydrolysis and the influence of some reaction conditions on its rate since, it is usually admitted that the growth rate of silica is similar to the hydrolysis rate.[54, 55] OH^- is produced by reaction of NH_3 and H_2O. Therefore, an increase in the concentration of NH_3 or H_2O will increase the reaction rate, by increasing the concentration of OH^-. The reaction is first order in NH_3, *i.e.*, the rate increases linearly with the concentration of NH_3.[56] Identically, the hydrolysis was found to be first order in TEOS.[55, 56] The influence of the concentration of H_2O on the hydrolysis rate is even more important according to Harris *et al.* with a ratio of $[NH_3]:[H_2O]^{1.5}$. That way, increasing the concentrations of H_2O and NH_3 results in a faster reaction and thus in bigger silica particles. However, particle size decreases after a maximum radius is observed when increasing both the concentration of H_2O and NH_3, even if the reaction times continue to decrease. Generally, larger particles can be obtained by increasing the concentration of TEOS, even if this effect is quite moderate and sometimes, the opposite phenomenon was observed.[51]

The nature of the substituents on the silicon atom permits to explain the reactivity of organoalkoxysilanes using the base-catalyzed mechanism. Two contributions can be observed: steric hindrance to nucleophilic attack and the ability to withdraw electrons, since the Si-O bond is more polarized for low alkoxides, increasing the electrophilicity of the Si atom. The lower alcohol derivatives are therefore more reactive and faster to hydrolyze than higher or branched alkoxides. Additionally, large alkoxy substituents are also more bulky, which also contributes to a diminution of the Si center reactivity. In consequence, the rate of hydrolysis increases for every loss of an alkoxy group. This consideration permits also to explain their ability to polymerize since silicon is more electron-withdrawing than hydrogen.[51]

Additionally, other thermodynamic as well as kinetic parameters such as the temperature, the nature of the solvent or the addition rate of the reagents, affect particle size and distribution. For instance, increasing the length of the alcohol used as solvent leads to an augmentation of the size. The diminution of the temperature provokes always an increase of the particle size. Bogush *et al.* established that in general lowering the temperature by about 30 °C doubles the particles size. It was also observed that monodispersity was not systematically obtained at low temperature (9 °C). Whereas, at higher temperatures, narrow size distributions were maintained.[57]
The last parameter is usually neglected in most of the articles about the Stöber process, although Nozawa *et al.* showed that the addition rate plays an important role. Indeed particles with 1800, 1300 and 600 *nm* were synthesized simply by changing the addition rate of TEOS, respectively from 0.005 *via* 0.05 to 0.5 $mL{\cdot}min^{-1}$.[58]

In this chapter, only the base-catalyzed systems will be discussed, since they provide dense, highly cross-linked spherical particles, whereas acid-catalyzed systems provoke chain-like open branched polymers with a low crosslinking density, which cannot be used to build opals of silica particles.[52, 53, 59]

Even if the Stöber procedure has attracted much interest, the reason why these particles are so well defined with a narrow monodistribution is still disputed.[51] Two main models are proposed. Initially, LaMer's model[60] on nucleation and growth was used to explain the shape and the distribution of Stöber particles. After an initial burst of nucleation, the growth of the nuclei continues on their surface through condensation of hydrolyzed monomers. In contrast, the second model suggests that nucleation takes place continually along the reaction, but that the nuclei aggregate later on to form larger particles with a narrow size distribution.[57]

2.3.1 LaMer Model

Harris and coworkers assumed that the Stöber process obeyed LaMer's homogeneous nucleation and growth model.[56, 61] This model was initially established in 1950 by LaMer and Dinegar to describe the formation of monodisperse sulfur particles.[60] According to LaMer's model (Figure 2.4), TEOS is slowly hydrolyzed until the so-formed silicic acid reaches the critical concentration (C_N) to form nuclei. After a short period, the silicic acid concentration decreases below the point C_0, where further nucleation becomes unlikely. After nucleation, the number of nuclei stays constant along the reaction. Particles growth continues until the concentration is reduced to the equilibrium solubility (C_S). The key of this mechanism resides in the nucleation phase, which should be short enough, so that both the diffusion and the growth are controlled.[62] Additionally, Harris and coworkers emphasized that when the concentration of silicic acid exceeds a critical value, the particles obtained were polydisperse.

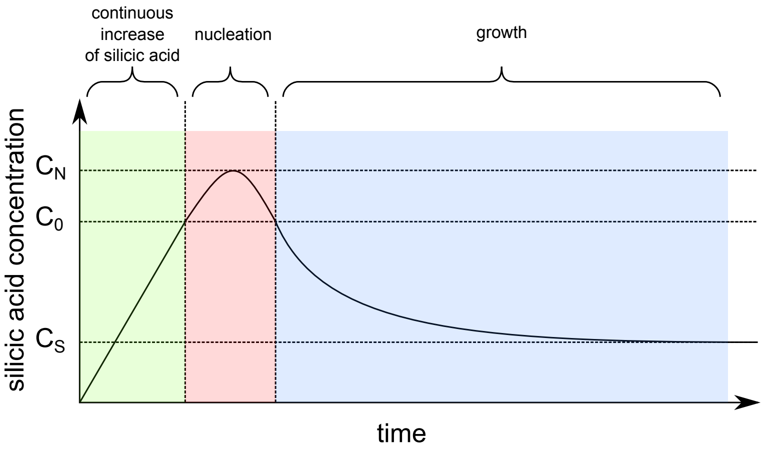

Figure 2.4: LaMer diagram of dissolved silicic acid concentration before and after nucleation, with C_N the concentration of silicic acid where the nucleation start, C_0 the concentration of silicic acid where the nucleation stop and C_S the equilibrium of solubility of silicic acid.[60]

2.3.2 Coagulative Mechanism

Bogush *et al.*[57, 63, 64] elaborated an alternative model based on observations by electron microscopy, conductivity, and change of reaction volume. They observed that almost all the TEOS is consumed within a few minutes, and also that silica particles were formed through a coagulative mechanism. According to Bogush and coworkers, nucleation continues along the entire process. At the first stage, small unstable particles aggregate until a critical size is reached, at which the probability of two particles of the same size sticking together becomes negligible. Once the aggregates are stable enough, their total number stays constant until the end of the reaction even if the homogenous nucleation continues, as the freshly formed small particles aggregate with the stable ones. Similarly to a model used to explain the emulsion of styrene polymerization,[65] Bogush *et al.* proposed a size-dependent nucleation-aggregation mechanism.

2.4 Stability of the Particles

The term "*stability*" in colloid science is used not only considering the absolute minimum of energy but comprises also metastable situations with relative minimums of energy. In general, sols are considered stable when the colloids do not settle or aggregate with a significant rate. An aggregate is a structure composed of colloid particles held together by cohesion. In this way, it is possible to differentiate between the type of cohesion, such as gelation, coagulation, flocculation or coacervation.[48]

- Gelling: particles are linked together in branched chains forming a network that retains water by capillarity.
- Coagulation: particles assemble into a more packed cluster structure in which the local concentration of silica increases compared to the original *sol*. It is common for this aggregate to precipitate.
- Flocculation: particles are linked by flocculation agent bridges. This can also provoke precipitation.
- Coacervation: particles are surrounded by an adsorbed hydrophobic layer, but do not form bridges between them. The aggregates form then an immiscible phase with water.

The stabilization of colloids is described by the DLVO theory (1940s), named after its authors: Derjaguin, Landau, Verwey and Overbeek. The total force of the particles in suspension is assumed to combine the attractive long-range van der Waals forces, present regardless of the chemical nature, and the repulsive double-layer electrostatic forces due to the surface charge groups or eventually by specific ion adsorption.[1] [52] Therefore, silica particles are rather stable in water or polar solvents such as ethanol, due to their negatively charged surface from the deprotonated silanol groups. Stöber particles do not aggregate as long as the charges are not screened by a salt, or dissociation is not subdued by a non-polar solvent. Nevertheless, silica particles do not completely conform to the DLVO theory because the particles seem to be stabilized by a layer of adsorbed water on their surface. Figure 2.5 illustrates the two cases of electrostatical (black curve) and sterical (purple curve) stabilization. In general, electrostatically stabilized systems present two minima of energy separated by an energetic barrier. The height of this barrier determines the particles fate: if the barrier is low, the particles will aggregate and end in the primary minimum. However, if the barrier is big enough, the thermal energy, approximatively around some kT (where k is the Boltzmann's constant), does not overcome the barrier, and the particles will repel and remain dispersed in a metastable state.

Additionally, sterically stabilized systems dispose of a protective adsorbed layer, which prevents aggregation and increases the distance between the particles. The stability depends of the thickness of the layer, which is made of water in the case of silica particles.[67, 68] This steric stabilization of silica can even persist at the isoelectric point, and so the only way to destabilize the particles, is to perform ion exchange, which reduces the amount of adsorbed water layer.[69–73].

---

[1] with V_A the attractive van der Waals potential and V_R the repulsive electrostatic potential, defined for two spheres by $V_A \propto -\frac{1}{d_s}$ and $V_R \propto e^{-\kappa d_s}$, with d_s as the distance between the surfaces.[66]

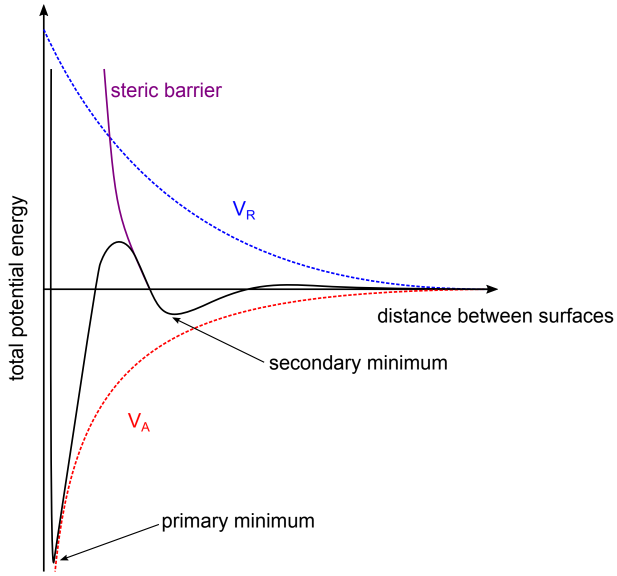

Figure 2.5: Schematic representation of total potential energy *vs.* distance between surfaces in the case of electrostatic (——) and steric (——) stabilization, with V_A attractive van der Waals potential (——) and V_R the repulsive electrostatic potential (——).

2.5 Dynamic Light Scattering

Dynamic light scattering (DLS) is a common technique to determine the size and the distribution of dispersed particles. Generally, this technique can characterize particles from a very small scale, a 1 nm to almost 1 μm. These two parameters must be controlled to build a photonic crystal of good quality. As already mentioned, non-uniform particle sizes disturb the crystal structure, so that the reflected light intensity reduces dramatically. Moreover, even if the size distribution is sufficiently narrow, the absolute size of the particles plays an important role, because this determines the wavelength of the reflected light. Only a properly adapted size will allow to reflect visible light.

DLS will be only briefly discussed in this section, for more detailed information, see references on light scattering in colloid science.[67, 74, 75]

The phenomenon of light scattering appears, when an incident light beam interacts with the electronic cloud of a material, which re-emits the light, called scattered light. Moreover, the scattering centers (here: silica particles) are undergoing Brownian motion (random motion). In this way, the dynamic variation of the particle positions makes fluctuate the scattered light intensity at a given scattering angle, as result of constructive or destructive interferences.[76]

That way, particles sizes, or more correctly, hydrodynamic radii can be determined *via* their *Brownian fluctuation.* The fluctuation is analyzed using an autocorrelation function, to provide the particles' diffusion coefficient. In other words, DLS measures Brownian motion of particles in solution. This motion becomes faster, when the size of particles decreases. The hydrodynamic radius (R_h) can be obtained *via* the Stokes-Einstein relation, which describes the diffusion coefficient of a spherical particle in a fluid as a ratio between the thermal energy and the friction coefficient.[67]

$$R_h = \frac{kT}{6\pi\eta D} \tag{2.1}$$

With T as the absolute temperature, k as the Boltzmann's constant, η as the solvent viscosity and D as the diffusion coefficient.

Note that for colloids such as silica particles, the measured hydrodynamic radius is usually slightly larger than the true particle radius. This difference is usually attributed to an adsorbed layer of solvent, ions or even surfactants on the particle surfaces. Concerning silica colloids, a layer of water is often bound on the particle surface. Therefore, the values obtained by DLS tend to overestimate the true particle size, which should be slightly smaller than the measured size.

In practice, a DLS experiment leads to the intensity-correlation function $G(q;\tau)$, which is independent of t. This function is obtained by averaging the intensity of the scattered light (I) at t and $t+\tau$, with τ as the time difference.

$$G(q;\tau) = < I(t) \cdot I(t+\tau) > \tag{2.2}$$

At a large delay time, $I(t)$ and $I(t+\tau)$ are not related, while for a small delay (in the order of microseconds) they can be correlated. This correlation measures the probability of the particle motion over a time difference, τ. For monodisperse particles, this correlation can be written as a decreasing exponential function:

$$G(q;\tau) = A\left[1 + Be^{-2Dq^2\tau}\right] \tag{2.3}$$

With A as the baseline of the correlation function and B as the intercept of the correlation function, D as the diffusion coefficient and q the wave scattering vector described as follows:

$$q = \frac{4\pi n}{\lambda \sin\left(\frac{\theta}{2}\right)} \tag{2.4}$$

Where λ is the incident wavelength, n the refractive index and θ the angle of the scattered light.

One of the downsides of DLS is that for more complex systems, the refractive index and the viscosity need to be determined. Still, for standard systems such as Stöber particles in water, these parameters are often known and implemented in the measuring software.

2.6 Conversion

Once particle synthesis was conducted, it was necessary to quantify the efficiency of the procedure by measuring the conversion of the TEOS, in addition to measuring the size and the dispersity.

Here, the conversion of TEOS was approximated by the yield of silica, which was determined conveniently by gravimetery, since all the other components can be easily evaporated. Normally, conversion has to be quantified by more intricate methods such as NMR or gas chromatography. Since the silica particles are the only solid of the reaction, the measurement of the solid content leads directly to the conversion of the reaction. Still, gravimetry does not inform about the purity.

Since impurities can affect the formation of colloidal crystals, the particles were subjected to a purification protocol. First, the solution was concentrated *in vacuo*, then the particles were separated by ultra-centrifugation from the supernatant liquid, and then redispersed in pure ethanol.

The conversion was defined as the ratio of the silica mass measured (m_{SiO_2}), divided by the mass of silica in the case of full conversion (theoretical or maximum mass of silica: $m_{SiO_2}^{theo}$).

$$\text{Conversion} = \frac{m_{SiO_2}}{m_{SiO_2}^{theo}} \tag{2.5}$$

2.7 Synthesis of Stöber Particles

Monodisperse silica particles, namely Stöber particles, can be synthesized with a size range from 50 *nm* to 2 *µm*. [77] This process introduced by Stöber *et al.*[47] and fundamentally explained in the Section 2.3, is a classical method for monodisperse colloid synthesis. This straightforward one-pot reaction leads to tunable and reproducible monodisperse silica particles, as long as the parameters are kept strictly constant.

Here, the particle sizes were designed to produce a visible color once assembled as colloid crystal, but also to provide large spherical templates. This should lead to hydrogel materials with large pores that are highly permeable even to big molecules. Accordingly to the approximate rules: $\lambda \approx 2d$, with λ the Bragg peak position of the silica opal at normal incidence, and d the diameter of the particles (see Chapter 3). Silica particles with a diameter of 400 *nm* were targeted since once assembled, they should diffract light around 800 *nm* which is around the upper border of the visible light of the electromagnetic spectrum.

The principle of the reaction consists in the addition of two reagent mixtures, one containing silicate precursor (TEOS) in ethanol, and the second consisting of an ammonia solution. The reaction instantly starts, when the TOES/ethanol mix is added to the ammonia solution. The particle size is modulated by the concentrations of the reagents, the temperature, the velocity of the stirring and the velocity of the mixing. After at least 12 *h* reaction times, the particles were submitted to a purification procedure. This method first consists in evaporation of the solvent, but without drying the silica particles that might become permanently agglomerated if the liquid phase is completely removed. The concentrated dispersion was then diluted in pure ethanol, in ten times its volume, centrifuged/redispersed 6 times by replacing the supernatant by pure ethanol. Later, the dispersions were characterized by DLS and the conversion was determined as explained in Section 2.5.

Since the process is driven by kinetics, a small change of a seemingly marginal parameters may change the particle sizes and the size distribution. Yet, important informations, such as the size or the form of the stirrer, or even the velocity of the mixing are often not specified, and differences in these key parameters may explain the scatter of the results reported in the literature.

The Table 2.1 depicts the modulation of synthesis parameters, which leads to particles close to 400 *nm* in diameter in most case. The parameters were adapted from the work described by Santamaría Razo *et al.*[78] Since the first attempts led to much smaller particles than expected, the other parameters were adjusted in order to correct this deviation. The encountered problem could be due to starting materials from different providers, or missing experimental informations (stirring, velocity of mixing,...). In order to increase the size of the particles to 400 *nm*, several combined parameters were adjusted. Still, the goal of this study was to obtain silica particles with a size of 400 *nm via* a satisfactorily reproducible process, not to establish a systematical method for obtaining different particle sizes. Within this context, the different batches listed in Table 2.1 were synthesized. Subsequently, the recipe providing the most satisfying batch, *i.e.* **SiO_2-3** (see below) was repeated 3 times in order to estimate its reproducibility. For more details about the experimental procedure see Chapter 8.

Table 2.1: Explored Stöber process parameter.

	TEOS[a] $[mol{\cdot}L^{-1}]$	NH_3[b] $[mol{\cdot}L^{-1}]$	ultra-pure water[c] $[mol{\cdot}L^{-1}]$	ethanol[c] $[mol{\cdot}L^{-1}]$	T [°C]	addition velocity $[mL{\cdot}min^{-1}]$
SiO_2-1	0.12	2.33	13.80	10.75	30	125
SiO_2-2	0.12	2.33	13.80	10.75	30	250
SiO_2-3	0.12	4.33	13.80	10.75	30	250
SiO_2-4	0.18	4.33	13.80	10.75	30	250
SiO_2-5	0.06	4.33	13.80	10.75	30	250
SiO_2-6	0.12	4.33	13.80	10.75	40	250
SiO_2-7	0.12	4.33	13.80	10.75	50	250

[a] TEOS purified *via* distillation,

[b] From commercial grade: 28 *wt.*-%,

[c] High purity grade: ultra-pure water and anhydrous ethanol.

The influence of the parameters discussed in Section 2.3 (TEOS and ammonia concentrations, temperature), were confirmed by the size profiles of the particles obtained (see Figure 2.6). Only the influence relative to the increase of the velocity was observed to be in contradiction with the discussion in Section 2.3.

It was observed that the increase of the velocity of mixing from both **SiO_2-1** to **SiO_2-2** produces an increase of the particle size from 236 *nm* to 336 *nm*, when all the other parameters were kept constant. This differs from the opposite tendency highlighted by Nozawa *et al.*,[58] whose study shows a decrease of the particle size upon higher velocity of mixing. This may be due to a major difference of the parameters' magnitude, such as the concentrations, but also of the velocity, which is in our case more than 1000 times higher. The increase of the concentration of ammonia (**SiO_2-3**) was noticed to increase the particle size, resulting in particles with a diameter close to 400 *nm* (406 *nm*).

Later, in order to investigate the other parameters, the concentration of TEOS, which affects less the final size of the particles, was varied. It was observed that upon a diminution by a factor of two of the TEOS concentration, the particle sizes decrease by 104 *nm* (**SiO_2-5**). By contrast, when the TEOS concentration doubles, the particle sizes increase by 62 *nm* (**SiO_2-4**). Finally, an increase of the temperature was noted to decrease strongly the particle size. When the reaction is conducted at 40 °C (**SiO_2-6**) instead of 30 °C (**SiO_2-2**), the particle sizes decrease by 10 *nm*, whereas at 50 °C (**SiO_2-7**) the particle size decrease by 137 *nm*.

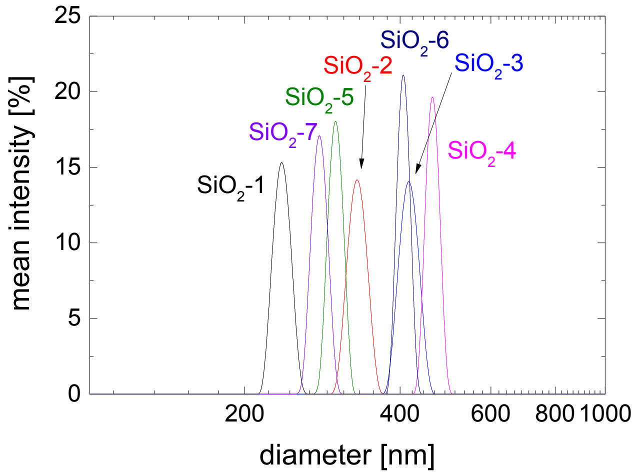

Figure 2.6: Size distribution of the Stöber particles; **SiO_2-1** (——), **SiO_2-2** (——), **SiO_2-3** (——), **SiO_2-4** (——), **SiO_2-5** (——), **SiO_2-6** (——) and **SiO_2-7** (——) (see Table 2.1).

The batch **SiO_2-3** exhibits satisfying particle sizes. Therefore, the reaction was repeated 3 times (Figure 2.7), in order to estimate the "*batch-to-batch*" variability, which occurred even when the reaction was reproduced with the same parameters and conditions. The particles size were noticed to slightly fluctuate around 415 ± 5 *nm* with a relative standard deviation (SD_{rel}) of 4 ± 1%, which was considered to be acceptable for the planned of studies. Therefore it can be approximated that these particle sizes are kept constant at 415 *nm*. Additionally during the next step, which consists in the assembly of the silica particles into a regular colloidal crystal, these small variations did not influence the position of the photonic band notably, in contrast to the assembly parameters (concentration, solvent, temperature . . .), see Chapter 3.

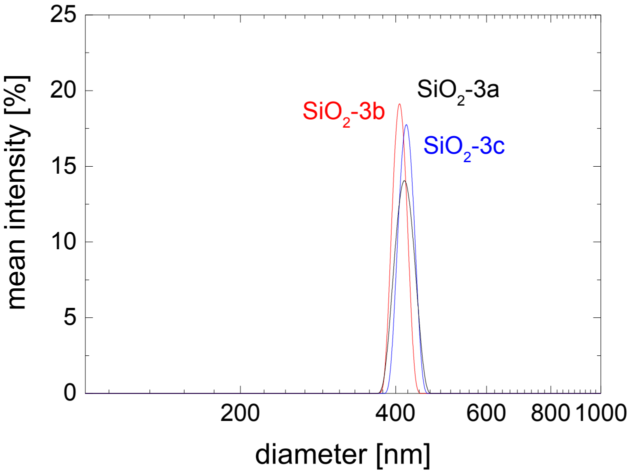

Figure 2.7: Size distribution of the Stöber particles; **SiO_2-3a** (——), **SiO_2-3b** (——) and **SiO_2-3c** (——) (see Table 2.1).

Table 2.2 summarizes the DLS data of the silica particles: the diameter, the absolute and relative standard deviation (SD_{abs} and SD_{rel}) and the full width at half maximum (*FWHM*). Another important parameter apart from the particle sizes, is the dispersity of the distribution, although this parameter was considered secondary in this study, due to the always low polydispersity. No obvious reaction conditions were observed to affect the SD_{rel} of the particles size, which stays always around 3-4% (Table 2.2). This is actually a primordial condition for the following step, since it determines the regularity of the silica crystals. The limit for SD_{rel} generally admitted for obtaining a sufficiently ordered silica opal crystal is 5%.[15]

The Stöber particles **SiO_2-3** respect the narrow distribution criterion and are suitable for the next step: the silica particle assembly into a homogenous colloidal crystal. The particles **SiO_2-3** were chosen due to their size of 415 *nm*. Because the final nanostructured hydrogel is targeted to be used in biomedical application with interaction of large molecules, the pores and also the silica particles must be as large as possible. However, too large particles may have problems to homogeneously assemble due to a higher sedimentation rate.[79, 80] Even if crystals with large particles (> 600 *nm*) are technically possible and might be suitable for sensing of macromolecules, their diffractions will reflect wavelengths in the infra-red range. Since sensors exhibiting a visible light are targeted, the particle sizes were deliberately limited to a size of 400 *nm*.

Table 2.2: DLS data of SiO_2 particles.

	d^a [nm]	${SD_{abs}}^b$ [nm]	${SD_{rel}}^c$ [%]	$FWHM^d$ [nm]
SiO_2-1	236.2	9.2	3.9	21.7
SiO_2-2	330.7	14.0	4.2	32.9
SiO_2-3a	416.7	17.8	4.3	41.9
SiO_2-3b	407.4	12.6	3.1	29.7
SiO_2-3c	419.8	14.0	3.3	33.1
SiO_2-4	462.7	13.9	3.0	32.7
SiO_2-5	300.2	9.9	2.1	23.2
SiO_2-6	406.3	11.3	2.8	26.6
SiO_2-7	279.3	9.8	3.5	23.0

[a] Mean diameter,
[b] Absolut standard deviation,
[c] Relative standard deviation,
[d] Full width at half maximum defined for normal distribution by $FWHM = 2\sqrt{2ln(2)} \cdot SD_{abs}$.

In the next chapter, it will be explained how the synthesized monodisperse silica particles (**SiO_2-3**) can be used as starting material for the assembly of silica opals, which manifest optical properties. Additionally other characterization techniques (electron microscopy: 397 *nm* ± 2% and atomic force microscopy: 387 *nm* ± 1%) were used to confirm the particle size determined by DLS: 415 *nm* ± 4%.

3 Silica Opals

This chapter describes the construction of the sacrificial opals, which were used as template for IOH synthesis. These materials, also named colloidal crystals (CCs), are a particular type of photonic crystals made of self-assembled spherical nanoparticles. These CCs are often synonymously called opals, although they may be built of other materials than SiO_2, such as TiO_2 or polystyrene (PS).[16–18] Their particular 3D ordered structure that consists in periodic domains with distinct dielectric constants confers them rather unique optical properties, which prevent the propagation of specific wavelengths. The particular optical properties depend highly on the homogeneity of the lattices of the CC and on their diffraction plane parameters. Therefore, various techniques have been developed to self-assemble colloidal particles in regular structures.[15, 22, 79, 81]

In order to obtain a regular structure, it is necessary to control several parameters such as:

- the dispersion of the nanoparticles,
- the speed of the assembly,
- the regularity of the lattice.

The first criterion was discussed in the previous chapter (Chapter 2). Silica particles with a narrow dispersity were obtained *via* the Stöber process. Thus, the next sections will cope with the two other criteria, related to particle self-assembly.

3.1 Assembly

In general, particle assembly is driven by a combination of the *attractive long-range van der Waals forces* and the *repulsive double-layer electrostatic forces.* For a more detailed discussion see Section 2.4. Silica dispersions are usually stable, as repulsive interactions between the particles are prevailing, and can be stored for months under standard conditions (room temperature, sealed flask ...). An additional driving force must be applied to assemble the particles into a crystal lattice, as needed to exhibit iridescence. For instance, sedimentation of particles is led by the gravitational force. However, this assembly process is rather slow to obtain a regular lattice. Therefore, other assembly methods are generally preferred such as centrifugation[82] or spin coating,[83, 84] using this time centrifugal forces, or even filtration.[85, 86] Techniques using electrophoresis were developed to overcome the inhomogeneous sedimentation of particles (smaller particles sediment slower than bigger particles).[87–89]

The most used 3D assembly technique was introduced by Colvin's group, known as vertical deposition.[15] This method was essentially inspired by the work of Nagayama *et al.* for 2D monolayer films,[90, 91] and leads to a relative low number of defaults. In the vertical deposition method (Figure 3.1), a substrate is placed vertically (occasionally tilted with a defined angle) in a container filled with a dispersion of nanoparticles. The CC germinates in the meniscus region, formed by the wetting of the substrate by the solution with a constant solution influx due to the constant evaporation of the solvent.[92, 93] The self-assembly of the particles at the interface is driven by the inter-capillary forces. This leads to close-packed opals with good quality. The so obtained CC is defined in the three space dimensions: its width is equivalent to the width of the substrate, its length is proportional to quantity of evaporated solvent on the substrate surface, and the thickness is relative to the concentration of the colloids dispersion (Figure 3.1). Although vertical deposition leads to homogenous 3D CCs, it might take some days to obtain a crystal length of 2-4 *cm*, depending on the solvent, the particle concentration, and the temperature.
In this regard, techniques similar to the Langmuir-Blodgett method were developed by Gu and coworkers as "*lifting substrate*" method.[22, 81] The principle is the same as for the vertical deposition, but the substrate is slowly moved out of the dispersion, instead of allowing the solvent to evaporate. In this way, the concentration of the dispersion remains constant along the process. Nevertheless, vertical deposition was preferred in this work since it requires only rather simple equipment, such as an oven.

In summary, vertical deposition is an easy and fast process, which leads to good opal quality in a reasonable time in a laboratory scale (growth: 1-2 *cm* length per day). Nevertheless, industry would prefer other techniques such as spin coating [83] or "*lifting substrate*" techniques,[81, 94] which are easier to monitor and to automatize on a bigger scale.

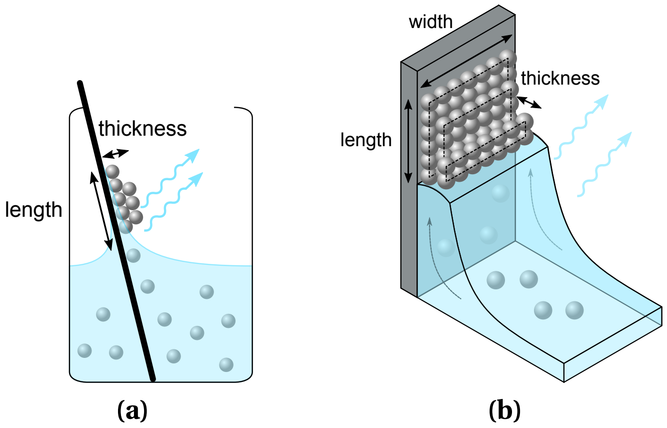

(a) (b)

Figure 3.1: Schematic representation of vertical deposition: a substrate is placed into a dispersion of colloidal particles.

In this work, the assembly method used was the vertical deposition due to its rather large adaptability and tunability of the assembly conditions. The thickness, and thus the number of layers, depends of the evaporation rate of the solvent and the concentration of the colloidal dispersion. Unfortunately, the quality of the opals, *i.e.* the number of defects, depends also on the evaporation rate and the particle concentration. They increase when the concentration is too high, or the solvent evaporates too fast. Therefore it is necessary to find a good balance between sufficiently well-structured and thick films. Since the intensity of the reflected light depends on both, the section Section 3.4 will address the parameters chosen to maximize the reflected light intensity.
Additional parameters, such as the inclination of substrate, the viscosity of the solution, and the size of the particles can influence the deposition. Nevertheless, this work focuses on two main parameters: the temperature and the concentration, while the other, presumably secondary parameters will only be briefly commented.

In films produced by vertical deposition using spherical particles such as silica, PS or PMMA, the particles are usually close-packed and mainly form a face cubic centered (fcc) lattice (Figure 3.2a).[15, 17, 19, 95] It has also been shown that non-spherical particles can also be assembled,[96] although it is difficult to assemble them in single regular lattices, mainly because of their non-uniform shape. Vertical deposition is possible on a large variety of substrates. In the specific case, the substrate will be used later on as a part of a sealed mold for infiltration and photo-polymerization of reactive premixes to yield nanoporous inverse opal hydrogels. Thus, the substrate requires to transmit UV-light, which in this work is UV A. This condition is fulfilled by ordinary glass, which is inexpensive and already well used in the literature.[15, 17–19, 81, 83, 91–94, 96] Additionally, glass substrates are easy to handle, to clean and to hydrophilize using mixtures of acid and oxidizing agents.

Vertical deposition processes for opal films are limited by the speed of solvent evaporation (growth: 1-2 *cm* length per day). The evaporation should not be too fast, as otherwise the particles cannot reach their favorite lattice sites, leading to defects and the loss of structural color. Defects are also due to the dispersity of the particles. Non-uniform size of particles leads to discordances in the lattice. This is illustrated in Figure 3.2b, where an increase of the size distribution provokes the loss of the regular close-packed arrangement.[15, 97] However, if deposition is too slow, the particles risk to sediment. Then, the local concentration in the neighborhood of the meniscus will decrease, changing the regularity and the thickness of the film. This will result in a lower film quality. Despite these downsides of the vertical deposition, it was possible to produce homogeneous opal films with sufficient quality to be used as a template to build nanoporous inverse opal hydrogels.

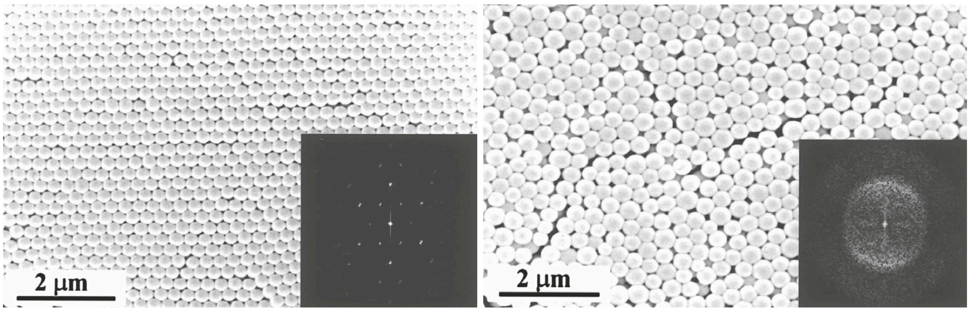

(a) **(b)**

Figure 3.2: Electron micrographs of two samples with different particles standard deviation (SD_{rel}). The insets show a Fourier transform of $40 \times 40\ \mu m^2$ regions, (a) high regularity, $SD_{rel} = 3.8\%$, (b) low regularity, $SD_{rel} = 14.2\%$. Reproduced from ref. [15].

3.2 Structural Color

In this section opals, in particular assembled silica particles, will be discussed regarding their crystalline structure, but also their optical properties. First, the classical silica opal structure will be presented. Then, the fundamental theory about opal diffraction will be depicted. Finally, characterization methods of such materials will be described.

3.2.1 Structure

In most cases, vertical deposition assembles particles in the energetically most favored lattice, which is a regular closed-packed arrangement as face cubic centered (fcc). Figure 3.3 illustrates the three lattice planes that describe all arrangements of silica particles in the fcc lattice: (111), (220) and (200). The planes are described as usual in crystallography by the Miller-indexes (hkl), which denote a plane that intercepts the three points of the coordinate frame: $\vec{\boldsymbol{a_1}}/h$, $\vec{\boldsymbol{a_2}}/k$ and $\vec{\boldsymbol{a_3}}/l$; an index zero means that the plane does not intercept this axis. For a cubic lattice $\vec{\boldsymbol{a_1}}$, $\vec{\boldsymbol{a_2}}$ and $\vec{\boldsymbol{a_3}}$ simply denote Cartesian coordinates $\vec{\boldsymbol{u_x}}$, $\vec{\boldsymbol{u_y}}$ and $\vec{\boldsymbol{u_z}}$.

The packing condition for a fcc lattice is defined as the relation between the particles' diameter (d) and the length of the edge of the cubic crystal(a_0). This means that the limiting condition is situated on the diagonals of the cube sides:

$$d = a_0 \frac{\sqrt{2}}{2} \tag{3.1}$$

An elemental cell in fcc lattices contains $8 \cdot \frac{1}{8} + 6 \cdot \frac{1}{2} = 4$ spheres, placed in the 8 corners and in the middle of each of the 6 faces of the cube. Thus the atomic packing factor (APF) can be defined as the ratio between the volume occupied by the particles and the volume of the primitive cell.

$$\text{APF} = 4\,\frac{V_{\text{sphere}}}{V_{\text{cell}}} = \frac{4^2\,\pi\left(\frac{d}{2}\right)^2}{3a_0{}^3} = \frac{\pi}{3\sqrt{2}} = 74\% \tag{3.2}$$

The APF is maximum (74%) for close-packed lattice such as fcc or hexagonal close-packed (hcp), whereas APF is smaller for other packings: body-centered cubic (bcc), 68%; simple cubic, 52%; diamond cubic, 34%.[98]

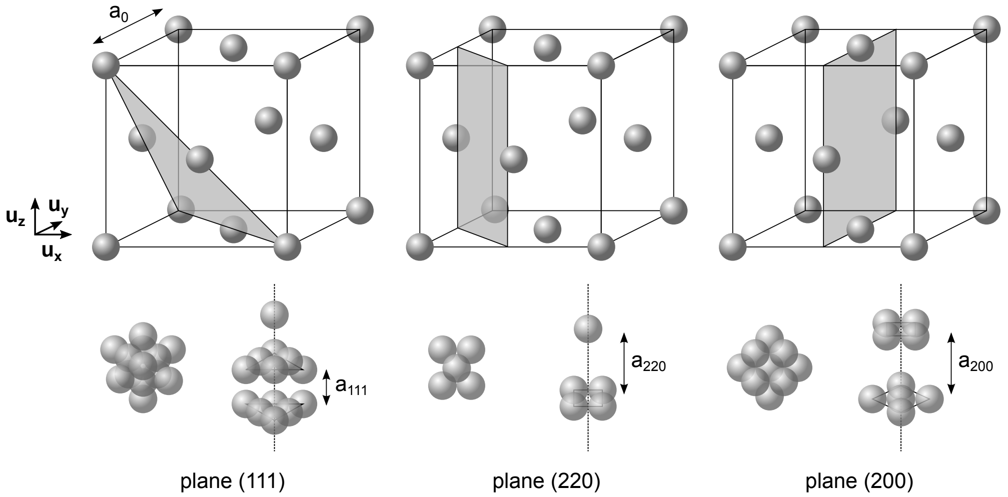

plane (111) plane (220) plane (200)

Figure 3.3: Structure of silica opals with fcc lattice, with the planes (111), (220) and (200) marked in grey, and their top-view.

In the top-view of the fcc plane (111), the spheres form closely-packed hexagons (Figure 3.3) that are separated by a distance d, which is the diameter of the particles. In this way, the lattice constant a_{111} can be obtained from the particle diameter d.

More generally for the plane (hkl) in a cubic lattice, the interplanar distance (a_{hkl}) can be defined as a function of h, k and l as follows:

$$a_{hkl} = d\sqrt{\frac{2}{h^2+k^2+l^2}} \tag{3.3}$$

Moreover, the relative angle between two planes (dihedral angle) can be defined as:

$$\vec{\boldsymbol{n_1}} \cdot \vec{\boldsymbol{n_2}} = \| \vec{\boldsymbol{n_1}} \| \cdot \| \vec{\boldsymbol{n_2}} \| \cdot \cos(\phi_{1-2}) \tag{3.4}$$

with $\vec{\boldsymbol{n_1}}$, $\| \vec{\boldsymbol{n_1}} \|$ and $\vec{\boldsymbol{n_2}}$, $\| \vec{\boldsymbol{n_2}} \|$, respectively, are two normal vectors of two planes with their norms. ϕ_{1-2} is the angle between these two vectors,

and with ϕ_{1-2} as the angle between the plane (hkl) and the plane (111).

$$\cos(\phi_{hkl}) = \frac{h+k+l}{\sqrt{3\,(h^2+k^2+l^2)}} \tag{3.5}$$

Table 3.1: Characteristic distances and angles of the planes in the fcc lattice.

plane	(111)	(220)	(200)
ϕ_{hkl}	0°	35.3°	54.7°
a_{hkl}	$d\sqrt{\frac{2}{3}}$	$\frac{d}{2}$	$d\sqrt{\frac{1}{2}}$
	$a_0\sqrt{\frac{1}{3}}$	$a_0\sqrt{\frac{1}{8}}$	$\frac{a_0}{2}$

3.2.2 Scattering and Diffraction

Photonic crystals were introduced by Yablonovitch and John.[99, 100] These materials, such as silica opals, exhibit a photonic bandgap that inhibits the propagation of light due to their particular periodical array of high and low dielectric constants. While atomic crystals diffract X-rays, the periodic feature depending on the exact size of the silica particles engenders the diffraction around the visible range of the electromagnetic spectrum.[7]

When an electromagnetic wave hits matter, it is subjected to scattering and lead to the emission of a scattered wave. When particles have a geometric organization (which is the case for a crystal), the scattered waves of each scattering center (atoms or silica particles) will interfere and produce constructive waves in some directions (the waves are summing up), and destructive waves in other directions (the waves are cancelled). This phenomenon is called diffraction. As in X-ray crystallography, for PhCs each plane of the crystal diffracts light according to the lattice spacing (a_{hkl}). The mechanism of the interferences is schematically described by Figure 3.4. In practice, coherent interference is not the only requirement for diffracting light. Additionally, the difference of refractive index, between the particles and the medium, needs to be big enough to obtain a decent intensity.

To explain the reflected color, Figure 3.4 illustrates a silica opal illuminated with monochromatic light: the plane (111) is hit by an incident beam (λ_0) under an angle θ_0^i. This incident beam is first transmitted (λ_1) according to the Snell-Descartes law. Due to the change of the refractive index, here $n_{air} = 1.00$ and n_{avg}, the light beam is deviated. The average refractive index (n_{avg}) is defined as the volume average of the refractive index that constitutes the crystal, n_{air} and n_{SiO_2}. Therefore n_{avg} can be calculated as follows: $n_{avg} = \varphi_{SiO_2} \cdot n_{SiO_2} + (1 - \varphi_{SiO_2}) \cdot n_{air}$. Since the particles are close-packed (fcc), the volume fraction of silica (APF or φ_{SiO_2}) is 74%. The resulting beam hits the refraction plane under an angle θ_1^i, where it is reflected with the same angle θ_1^r, to finally be transmitted from silica to air, leading to the outgoing beam of the reflected light (λ_0, θ_0^r).

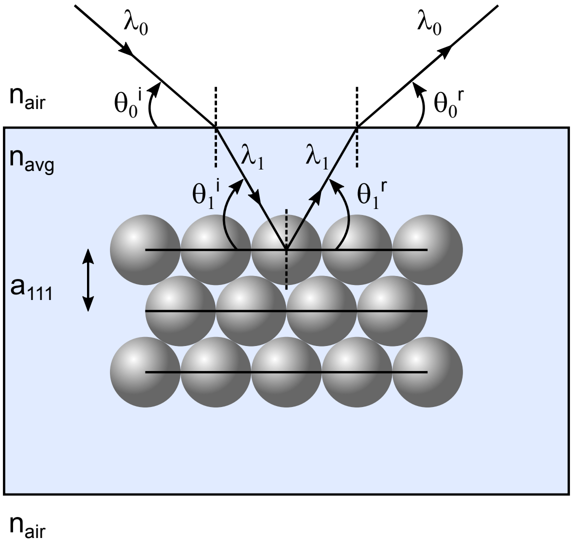

Figure 3.4: Diffraction of periodical fcc silica opal at the lattice plane (111).

Note: in our case the Snell-Descartes law is defined with the angle between the light beam and the diffraction plan, whereas the angle between the light beam and the normal of the crystal surface is normally used. It is also possible to define the angle between the light beam and the sample, which is the same as for the plane (111), while it is different, for the planes (200) and (220) (Table 3.1).

Snell Descartes law:
$$n_{air} \cdot \cos(\theta_0) = n_{avg} \cdot \cos(\theta_1) \tag{3.6}$$

and
$$n_{air}\,\lambda_0 = n_{avg}\,\lambda_1 \tag{3.7}$$

Bragg law :
$$2a_{hkl} \cdot \sin(\theta_1) = m_{\mathbb{N}}\,\lambda_1 \tag{3.8}$$

or
$$\sin^2(x) + \cos^2(x) = 1 \tag{3.9}$$

so
$$2a_{hkl}\sqrt{1-\cos^2(\theta_1)} = \frac{m_{\mathbb{N}}\,\lambda_0}{n_{avg}} \tag{3.10}$$

$$\Rightarrow \quad 2a_{hkl}\sqrt{1-\frac{\cos^2(\theta_0)}{n_{avg}^2}} = \frac{m_{\mathbb{N}}\,\lambda_0}{n_{avg}} \tag{3.11}$$

$$\Rightarrow \quad 2a_{hkl}\sqrt{n_{avg}^2-\cos^2(\theta_0)} = m_{\mathbb{N}}\,\lambda_0 \tag{3.12}$$

finally for the plane (111) and $m_{\mathbb{N}}$ an integer called the order of diffraction, we obtain:

$$2d\sqrt{\frac{2}{3}\left(n_{avg}^{2}-\cos^{2}(\theta_{0})\right)} = m_{\mathbb{N}}\,\lambda_{0} \tag{3.13}$$

Although atomic scale fcc crystals can diffract electromagnetic waves with different crystal planes, the color produced by silica fcc opals is mainly due to the reflection by the plane (111). Still, reflections from other planes such as (200) and (220) are possible. If the (111) reflection is close enough to the infra-red, it is sometimes possible to observe a less intense peak from the plane (220), which may affect the color properties.[7, 101] However, the reflection at plane (200) is usually not strong enough to be distinguished from the main reflection coming from the plane (111), particularly if the incident light is perpendicular to the sample. Since color of the crystals is angular dependent, this parameter affects the Bragg peak position as well as the Bragg peak intensity. The plane (111) is most intense for an incident angle θ_0^i of 90 °, due to its alignment with the surface of the sample ($\phi_{111} = 0$). In order to build a structural color template, this study will be focused on the plane (111).

3.3 UV-vis Spectroscopy

Opals or inverse opals were characterized in the transmission mode using a spectrometer. The equipment measures the intensity of the transmitted light (I), and quantifies it following the two variables, transmittance (*Trans*) and absorbance (*Abs*), with I_0, being the intensity of the incident light (Figure 3.5).

$$Trans = \frac{I}{I_0} \tag{3.14}$$

and

$$Abs = \log\left(\frac{I_0}{I}\right) \tag{3.15}$$

Normally, opals are characterized by UV-vis reflection spectroscopy (Figure 3.5, green beam). However, this work used transmission spectroscopy (Figure 3.5, red beam) since inverse opal hydrogels are transparent and allow to let the light pass through. The two methods are rather equivalent, when measuring the Bragg reflection *via* UV-vis transmission spectroscopy, the detector indicates the non-transmitted light which is assimilated to the reflected light. Therefore, this technique is commonly used to describe opals and inverse opal hydrogels. In practice, the sample is illuminated with a light source which hits the sample under an angle θ_0. The wavelengths corresponding to the Bragg reflection do not pass through the sample, whereas the residual, also called (complementary) transmitted wavelengths pass and are collected by the detector (Figure 3.5).

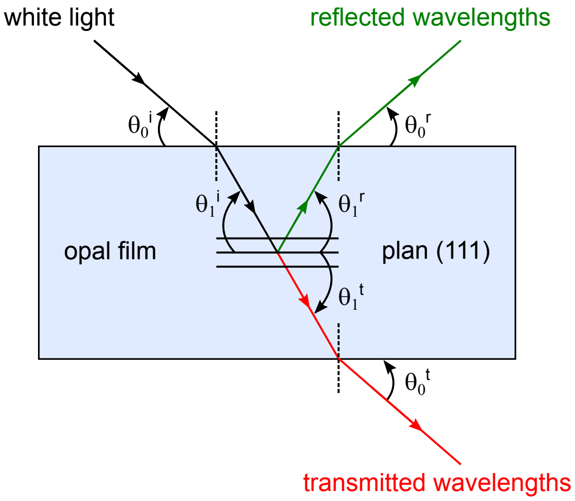

Figure 3.5: UV-vis reflection (——) and transmission (——) of the plane (111) of a silica opal film.

3.4 Vertical Deposition Assembly

In Section 3.1, the vertical deposition was presented as the method chosen to build easily and rapidly homogenous opals from silica particles with a size of 415 *nm*. First, the glass substrate was cleaned in order to remove impurities, but also to hydrophilize the surface with an oxidizing/acidic mix such as piranha solution. This classical cleaning solution is composed of a 1:1 v/v mixture of hydrogen peroxide (H_2O_2) and sulfuric acid (H_2SO_4). Once the impurities are removed, it plays a second role as cleaving Si-O-Si bonds, thus creating Si-OH and Si-O^- groups on the surface which increase the overall hydrophilicity. The negative charges increase the spreading of the silica solution (based on water/ethanol) due to a diminution of the contact angle and an increase of the capillary driving forces which govern the vertical deposition assembly (Figure 3.6), leading to a more homogenous and structured opal film.

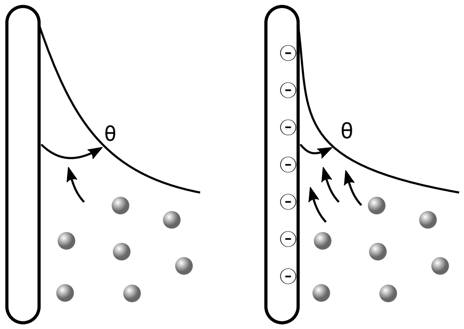

Figure 3.6: Illustration of (a) a non-hydrophilized, (b) an hydrophilized glass surface and its influence on the meniscus of the silica solution.

Therefore, cleaned and hydrophilized glass microscope plates are placed in a beaker that was before washed with HF solution in order to remove eventual glass or silica impurities that could disturb the deposition. The beaker was filled with the colloidal solution, placed in a thermally controlled atmosphere, *e.g.* in a drying oven. The oven was kept without ventilation, and opened as less as possible in order to maintain the atmosphere concentrated of solvent vapor. Additionally, the oven was placed in a stable place in order to absorb as much as possible the vibration, which were observed to disturbed solvent front and so the crystal array.

The different parameters were investigated in the same chronology than the order presented in the Table 3.2. First a mixture of water and ethanol was used as the evaporating mixture (**OP-1** and **OP-2**).

The use of water reduces the sedimentation of silica particles, and also the evaporating rate. Therefore, the deposition takes longer compared to solutions only made from ethanol. It was observed that this slow deposition (< 1 *cm* per day) creates irregularities of the surface of the film. The reason behind is that after long deposition time, the silica particles sediment in water/ethanol mixture. Thick films devoid of regular optical properties were so obtained. Consequently, the concentration of water was reduced, which increases the evaporation rate. This provokes a diminution of the observed thickness of the silica film. Besides, the increase of the evaporation rate, and the shortening of the deposition time, lead to an increase of the iridescences (**OP-3**). Since the sedimentation rate of silica in pure ethanol is relatively constant, the deposition time was shortened *via* an increase of the temperature. In this way, the apparitions of irregularities after 2-3 days are avoided.

It has been found that the increase of the temperature improves the iridescence until an upper limit. If the temperature of the deposition takes place above 40 °C, irides-

cence fades away. This can be illustrated by the diminution of the thickness of the film when the temperature increases (**OP-3** - **OP-6**).
The concentration of the silica is another parameter to control the deposition rate. The less the concentration of silica, the less the silica gradient (upon sedimentation) is pronounced. Therefore, the concentration of the silica was decreased (**OP-4**, **OP-7** - **OP-9**). It was noticed that the thickness of the film is not affected by a change of concentration of silica from 1.5 to 0.5 *wt.*-%. The strongest iridescence was obtained for 0.75 *wt.*-% (**OP-8**), although a decrease of the concentration of silica has been noted to improve first the iridescence intensity, while below 0.5 *wt.*-%, the iridescence disappeared and led to pearly white film (**OP-9**).

In order to confirm these primary observations, in Section 3.7 the iridescences of the opals **OP-4** - **OP-9** will be quantified *via* spectroscopy.

Table 3.2: Vertical deposition of silica particles varying **SiO_2-3** concentration and temperature.

	SiO_2 [*wt.*-%]	ultra-pure water [*wt.*-%]	ethanol [*wt.*-%]	*T* [°C]	thickness [μm]	appearance[a]
OP-1	1.5	20	80	30	25	opaque
OP-2	1.5	10	90	30	15	opaque
OP-3	1.5	0	100	30	10	iridescent − −
OP-4	1.5	0	100	35	10	iridescent +
OP-5	1.5	0	100	40	7.5	iridescent −
OP-6	1.5	0	100	45	5	iridescent − −
OP-7	1.0	0	100	35	10	iridescent + +
OP-8	0.75	0	100	35	10	iridescent + + +
OP-9	0.5	0	100	35	10	iridescent − −

[a] (− −) only faintly colored, (−) slightly colored, (+) colored upon strong illumination, (+ +) colored with irregularities , (+ + +) intensely colored.

The pictures in Figure 3.7 show a typical opal illuminated with a flash light from the bottom-left corner. The first picture (Figure 3.7a) shows an intense cyan color with an incident angle of approximatively 30 °. By contrast, the second picture (Figure 3.7b) displays an orange color when illuminated with an incident angle of 80 °. The intense iridescent color indicates the qualitatively good assembly of the silica particle upon **OP-8** conditions.

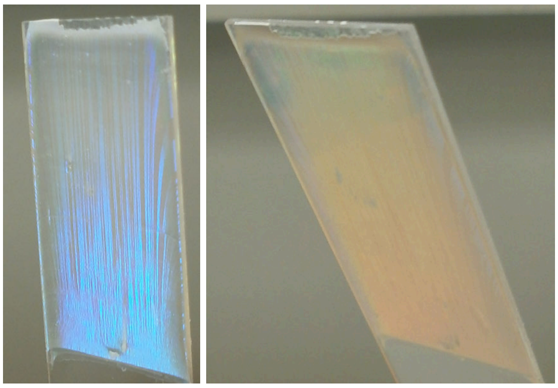
(a) (b)

Figure 3.7: Photographs of the silica colloid deposition **OP-8** at 30° and 80°.

As explained in Section 3.2, the observed colors are due to the reflection of certain wavelengths, which form a photonic band also called Bragg peak. Such changes of colors occur, although the structure of the opal is unchanged (Figure 3.7). Here, the Bragg peak is modulated by varying the incident angle. In Section 3.7, this color shift will be used to confirm the structure of the opal. But first, microscopy was used to verify the arrangement of the particles, as well as to estimate the thickness of the crystal that was until now measured with a micrometer.

3.5 Electron Microscopy

Electron microscopy is a powerful technique to elucidate microstructure, particularly for silica opals. The sample was prepared similarly to the method **OP-8** from silica particles with a size of 415 *nm*, according to DLS measurement. Only the support, which consists originally of a microscope plate made of glass, was replaced by a silicon wafer. This permits to obtain a better contrast between the support and the opal.

In Figure 3.8, silica crystal electron micrographs of **OP-8** are presented under two viewing angles, one from the top, and the other as a perpendicular cut through the plane of the crystal film (plane (111)). The micrographs (Figures 3.8a to 3.8c) show the top view with different magnifications. They highlight well arranged hexagonal lattices separated by important cracks. Nevertheless, Figure 3.8c and the hexagonal green marks show a qualitatively good regularity with the face cubic center (fcc) arrangement. In these micrographs the particles show a size around $397 \pm 2\ \mu m$.

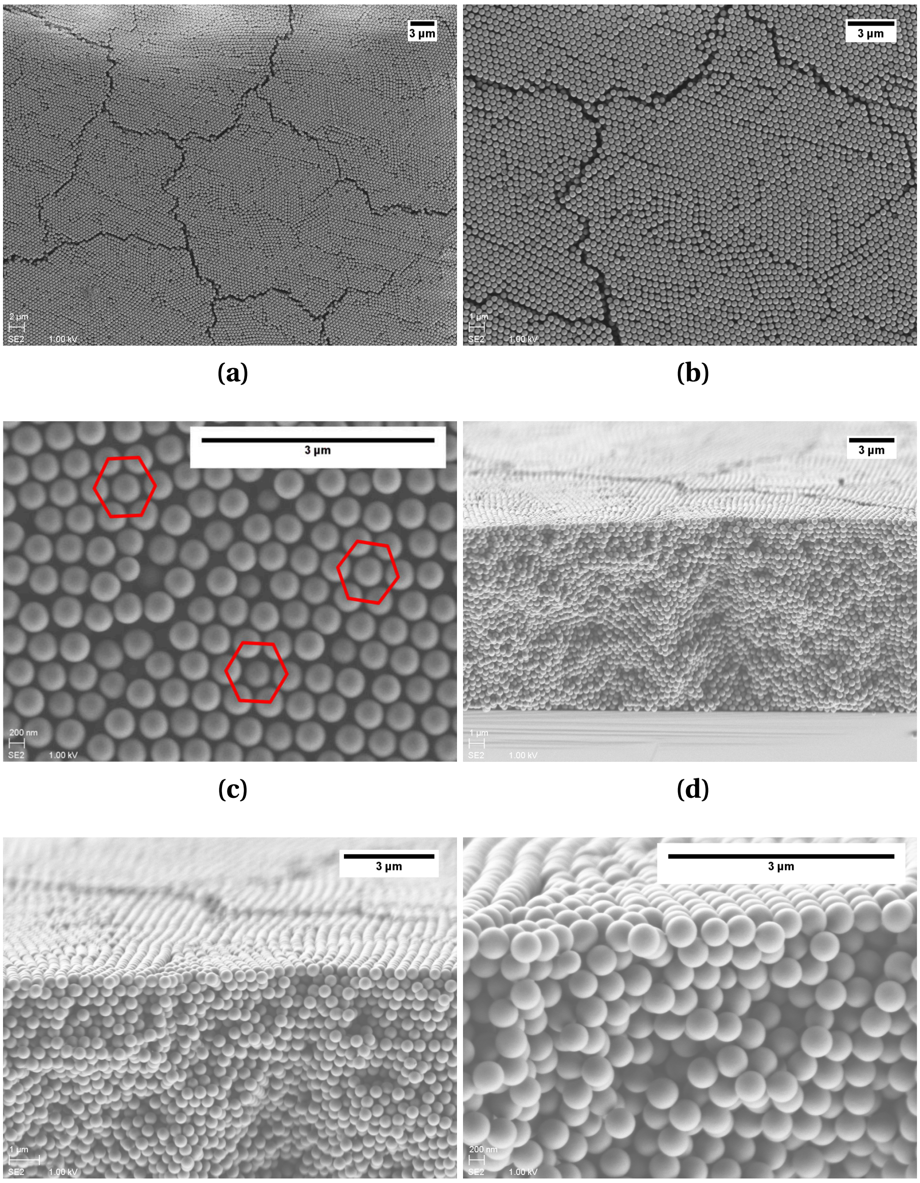

(a) **(b)**

(c) **(d)**

(e) **(f)**

Figure 3.8: Electron micrograph of silica opal sample **OP-8**, with size particles of 397 ± 2 *nm*, (a-b-c) front view, (d-e-f) face view.

Additionally, the cut views (Figures 3.8d to 3.8f) show a rather thick colloidal crystal (10 μm) made of 42 layers. Even at the end of the growing, the crystal does not show defaults that would reduce the regularity. On the contrary, the last layer (on top) still exhibits an impressive flat and regular hexagonal structure. Even if the close packed arrangement is quite obvious, it could not be determined from the micrographs if the arrangement is hexagonal close-packed (hcp) or face cubic center (fcc). The formation of a fcc array was assumed, since the fcc arrangement is described more often in the literature with vertical deposition, due to its more stable character.[18]

3.6 Atomic Force Microscopy

The regular topography of the silica opal crystal was also characterized *via* atomic force microscopy (AFM). This technique was used in addition to electron microscopy to confirm the arrangement of the silica particles on the surface. Although AFM can be used to elucidate the topography of the sample, it cannot be used to define the thickness of the opal. The last layer of silica particles which compose the surface of the sample should inform about the inner regularity of the sample. Since the sample is composed of 42 superposed layers, it is necessary for obtaining a regular last layer that the inner layers are regular. In other words, if the inner layers are not hexagonally packed, or present too many defects, the last layer cannot be regularly hexagonally assembled. Figure 3.9 shows atomic force micrographs of **OP-8**. The first micrograph (Figure 3.9a) exhibits highly regular hexagonal (red mark) structure over a surface with a size of 10×10 μm. Similarly to the electron micrographs, some defects, mainly cracks, reduce the hexagonal regularity. They are attributed to particle heterogeneities and/or problems during the assembly process (Section 3.4). The second micrograph (Figure 3.9b) highlights the composition of the opal surface of 3×10 μm formed by highly monodisperse silica particles (387 ± 1 *nm*). Moreover, the last micrograph (Figure 3.9c) represents the 3D surface of the sample **OP-8**, which exhibits a remarkably homogenously flat surface in addition to its hexagonal structure. This is explained as above due to the regular hexagonal structure present all long the 42 layers of the opal.

Similarly to DLS distributions or SEM micrographs, AFM micrographs show that **OP-8** is made of spherical particles which are highly monodisperse; DLS: 415 ± 15 *nm*, SEM: 397 ± 2 *nm*, AFM: 387 ± 1 *nm*.
Comparing the various results, the particle sizes obtained by SEM and AFM are slightly smaller than for DLS. This might be explained by the presence of a bound water layer adsorbed on the surface of the particles when particles are in solution as with DLS, which is generally estimated to be about 5% of the particle sizes. On a dry crystal state, such a water layer is missing, and so the measured size should be reduced by 20 *nm*, in agreement with particle size obtained by SEM and AFM. Additionally, the SD_{abs} of

the silica particles decreases also by comparison to SD_{abs} from DLS. This is attributed to the assembly, which is driven by capillary forces that are stronger when the particle sizes are similar. The vertical deposition induces a preselection of the particles, since the process is slow enough to be thermodynamically driven.

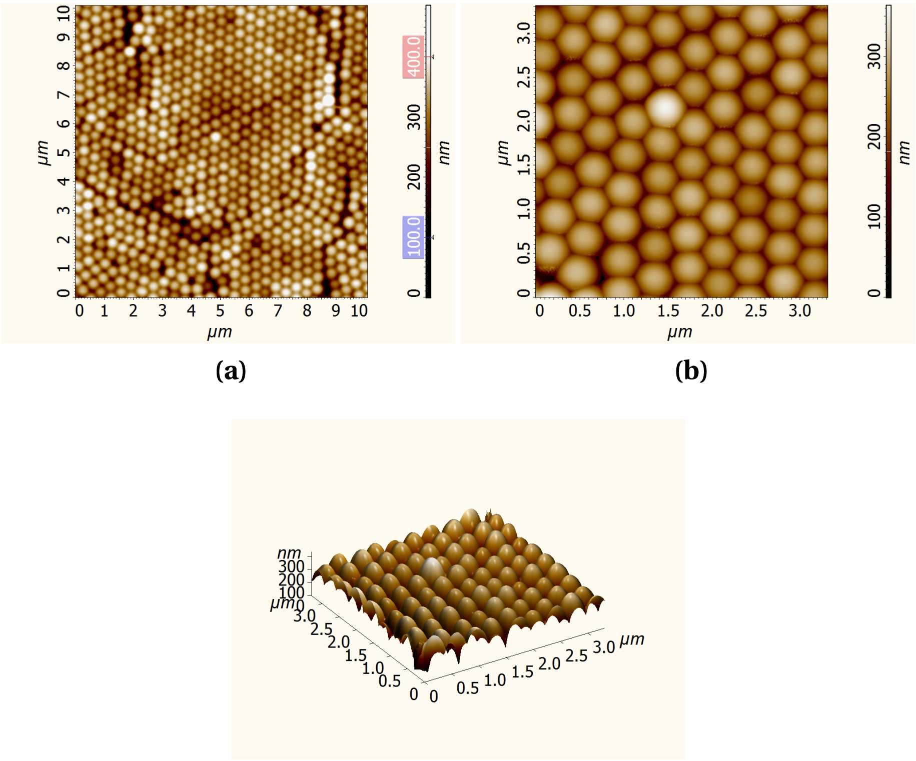

(a)

(b)

(c)

Figure 3.9: Atomic force micrograph of silica opal sample **OP-8**, with size particles of 387 ± 1 *nm*; (a) topography 10 × 10 *μm*, (b) topography 3 × 3 *μm*, (c) 3D representation 3 × 3 *μm*.

In spite of some defaults, high hexagonal regularity is revealed at the surface and also into the crystal. Although more elaborate assembly procedures may lead to "*quasi*" crack-free opals or inverse opals,[17, 102, 103] the crystals obtained were judged sufficient to exhibit intense light reflection *via* UV-vis spectrometry (see section Section 3.7).

In summary, colored silica opals were fabricated that can be used as template for inverse opal hydrogels. These opal templates are built by *ca.* 42 layers of hexagonally assembled monodisperse particles (SEM 397 ± 2 *nm*, AFM: 387 ± 1 *nm*), which gives a thin film of about 10 *μm* thickness.

3.7 Light Interference

The hexagonal structure of silica opals composed was clearly demonstrated *via* microscopy: SEM and AFM. In the following section, their aptitude to reflect certain wavelength will be investigated *via* UV-vis spectrometry. As explained in the Section 3.2, photonic crystals and other systems based on structural color present a strong dependence between the incident angles of the light beam and the reflected wavelengths, as predicted by the Bragg law.

These studies will focus on the reflection from the plane (111), which is the main contribution at normal incidence ($\theta_0 = 90^\circ$). We saw in the previous sections that the synthesized opals made of silica particles (*ca.* 400 *nm*) pack according to a fcc array. Therefore, at normal incidence, a Bragg peak between 600 *nm* and 800 *nm* is expected. At normal incidence, the Bragg law for the plane (111) can be in this way simplified as follows:

$$m_{\mathbb{N}}\,\lambda_0 = 2d\sqrt{\frac{2}{3}\left(n_{avg}^2 - \cos^2(\theta_0)\right)} \tag{3.13}$$

or

$$n_{avg} = 0.74 \cdot n_{SiO_2} + 0.26 \cdot n_{air} \tag{3.16}$$

with

$$n_{SiO_2} = 1.45 \quad \text{and} \quad n_{air} = 1.0$$

at $\theta_0 = 90^\circ$ and for $m_{\mathbb{N}} = 1$

$$\lambda_0 = 2d\sqrt{\frac{2}{3}}n_{avg} \Rightarrow \lambda_0 = 2d\sqrt{\frac{2}{3}} \cdot 1.33d \tag{3.17}$$

$$\Rightarrow \lambda_0 = 2.2d \tag{3.18}$$

In order to quantify the quality of the opal, the Bragg peaks of **OP-4** - **OP-9** were measured at normal incidence (Figure 3.10). Clearly, the majority of the samples exhibits a maximum of absorbance (Bragg peak) in the range of 600 *nm* to 1000 *nm*. These Bragg peaks are approximately positioned at *ca.* 800 *nm*. This is in agreement with the particle sizes of about 400 *nm* ($\lambda_0 = 2.2 \cdot 400 = 880$ *nm*). Still, it is noticed that the intensities of the Bragg peaks differ notably. For instance, **OP-6** and **OP-9** showed no absorption peak but only a weak shoulder at 785 *nm*. Their lack of internal structure already indicated visually (see Table 3.2) is thus confirmed by spectroscopy. In contrast, **OP-4**, **OP-5**, **OP-7** and **OP-8** exhibit intense Bragg peaks at 808 *nm*, 834 *nm*, 849 *nm* and 815 *nm*, respectively. The maximum intensity is obtained for **OP-8**, with an absorbance of *ca.* 1.06. The Bragg peaks' height of the various opals correlates

with the order of the crystal, or the "*quality*" of the assembly. [15, 101]
The comparison of the samples **OP-4 - OP-6** in Figure 3.10 clearly shows the decrease of the opals' quality upon increasing temperature. The increasing disorder of these samples is manifested by a broadening of their Bragg peak, which moreover, reduce its maximum of height, 0.44, 0.28 and 0 in absorbance, respectively. Additionally, the position of the peaks is shifted to longer wavelengths. This is due to a marked change of the interplanar parameter (a_{hkl}), which depends of the structure of the opal. As discussed before, a_{111} is a function of the silica particle diameter (d) according to $a_{111} = d\sqrt{\frac{2}{3}}$. Obviously, as the conditions of assembly change, the interplanar distance changes, too.

For the second group of samples **OP-4**, **OP-7 - OP-9**, the temperature was kept low, but the concentration of the silica was reduced. The Figure 3.10 illustrates not only the effect of the nanoparticles concentration on the opal quality, but also on the position of the Bragg peak. When the concentration of silica is decreased, the Bragg peak intensity passes through a maximum from 0.44 *via* 0.60 to 1.06 in absorbance, before further dilution results in a nearly complete loss of the Bragg peak.
Although the quality of the opal evolves continuous when changing the assembly parameters (temperature, concentration of silica), no obvious relation was noted for the Bragg peak position. Therefore, it is necessary to control, if the Bragg peak position of the selected opal (**OP-8**) matches with the highly regular fcc lattice observed *via* microscopy. Such information can be deduced from the linearization of the Bragg law, by following the Bragg peak position as function of the angle of the incident light.

Figure 3.10 highlights also the importance of hydrophilizing the glass substrate prior to particle deposition (see Section 3.4): when the glass substrate was only washed, but not hydrophilized by treatment with piranha solution, the silica film **OP-8 no** $\mathbf{H_2O_2/H_2SO_4}$ does not show a Bragg peak. In contrast, **OP-8** that was deposited under identical conditions but after appropriate hydrophilization of the glass substrate, exhibits an intense Bragg peak.

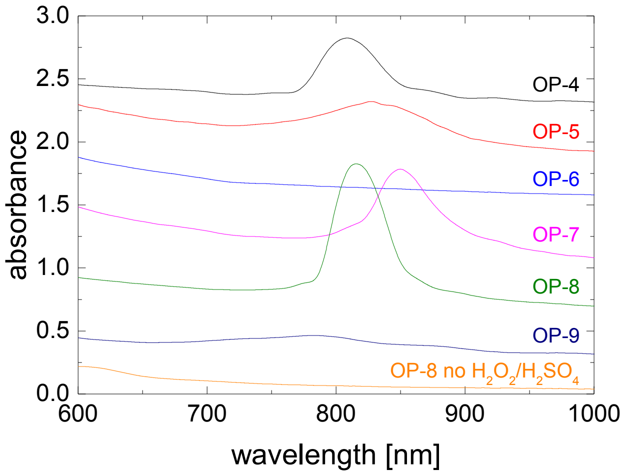

Figure 3.10: Absorbance of colloidal crystals deposited under different conditions on glass plates. (Table 3.2)

Opal build up by vertical depositions is reproducible, when all the parameters are strictly kept constant. The method limits' may reside in the maximum thickness of the opal layers. It was not possible to build iridescent film thicker than 10 μm. Nevertheless, under optimized conditions, **OP-8** exhibits a Bragg peak height of 1.06 in absorbance, which corresponds to 91% of non-transmitted incident light. These optical properties were judged sufficient to use the colloidal crystals as template for inverse opals.

It should be noted that in the experiments described above, the other deposition parameters discussed in Section 3.1 were kept constant, namely particle size, angle of the glass substrate,[104] or the geometry of the oven. The latter parameter must be respected, since it determines the concentration of the solvent in the atmosphere, which affects the evaporation rate, and so the assembly of particles.

More generally, if vertical deposition can produce colloidal crystals (**OP-8**) with similar Bragg peak positions, they are all slightly different. Nevertheless, for the purpose envisaged, the crystals obtained were checked *via* UV-vis spectrometer; their Bragg peak positions were always found to be closely within the same range of 800 ± 20 nm.

Futhermore, **OP-8** was characterized under different incident angles. Thus, its structural color was confirmed and correlated with the Bragg law. As illustrated by Figure 3.11, a linear correlation between λ_0^2 and $\cos^2(\theta_0)$ was revealed (Equation (3.20)).

The linearization allow to calculate the average refractive index (n_{avg}) and also the particle sizes (d) as follows:

$$2d\sqrt{\frac{2}{3}\left(n_{avg}^{2}-\cos^{2}(\theta_0)\right)} \;=\; m_{\mathbb{N}}\,\lambda_0 \qquad (3.13)$$

$$\Rightarrow \quad \left(2d\sqrt{\frac{2}{3}}\right)^{2}\left(n_{avg}^{2}-\cos^{2}(\theta_0)\right) \;=\; m_{\mathbb{N}}^{2}\,\lambda_0^{2} \qquad (3.19)$$

$$\Rightarrow \quad \left(2d\sqrt{\frac{2}{3}}\,n_{avg}\right)^{2} - \left(2d\sqrt{\frac{2}{3}}\right)^{2}\cos^{2}(\theta_0) \;=\; m_{\mathbb{N}}^{2}\,\lambda_0^{2} \qquad (3.20)$$

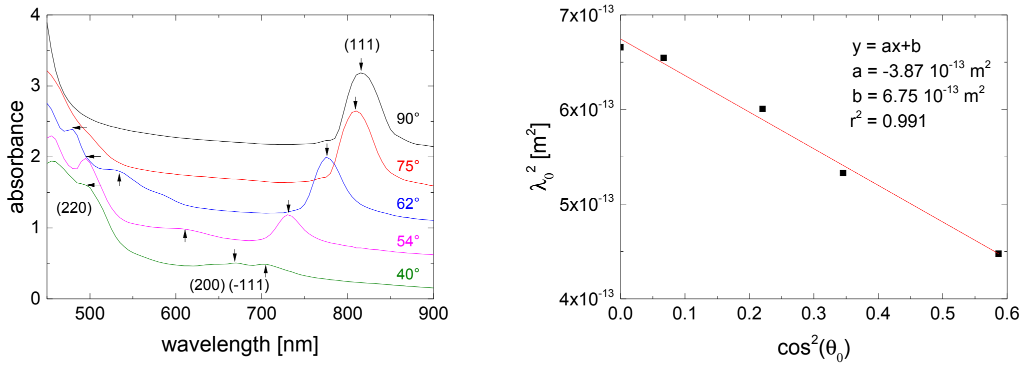

(a) (b)

Figure 3.11: UV-vis analysis of **OP-8** at different incident angles; (a) plots of the absorbance *vs.* wavelength, the diffraction peaks indicated by ↓, ↑ and ← are due to the plane (111), (200)/(-111) and (220), respectively; (b) linearized plot of the Bragg peak position (λ_0^2) of the plane (111) as function of incident angle ($\cos^2(\theta_0)$), with the order of diffraction, $m_{\mathbb{N}} = 1$

Figure 3.11a shows the diffraction peaks of **OP-8** at different angles. Three types of peaks are seen in the figure. The main peak (indicated by ↓) at around 800 *nm* is due to the plane (111), since the angle of the incident light is close to 90°. Other planes, such as (200), (-111) (indicated by ↑) and (220) (indicated by ←) might be observed in different wavelength ranges. Clearly, the position and the relative intensity of these peaks change as function of the incident angle. It should be noted that the planes (200), (-111) and (220) weakly reflect light compared to plane (111), especially, when the sample is illuminated by light under an angle close to normal incidence. The Bragg peak (111) intensity decreases when the incident angle decreases. Additionally, its position shifts to shorter wavelengths. By contrast, the intensity of the light reflected by the other planes ((200), (-111) and (220)) slightly increases when the angle of incident increases. Note also that their positions move to higher wavelengths. Figure 3.11a illustrates that the strongest intensity of the Bragg peaks is due to the plane (111) at normal incidence. Therefore, the optical properties of the opals and inverse opals will be described in the following *via* their reflection from the plane (111) at normal incidence.

Additionally, Figure 3.11b visualizes the correlation between the Bragg peak position and the incident angle ($r^2 = 0.991$), with $m_{\mathbb{N}} = 1$. The refractive index (n_{avg}) and the diameter of the silica particle (d) can be deduced from the slope and the intercept respectively, as $n_{avg} = 1.32$, and $d = 381\ nm$.
The particle size and the refractive index calculated in this way are in the range of the fcc expected values, $n_{avg} = 1.33$, and $d_{AFM} = 387\ nm$. The differences can be explained by defects in the crystal, which distort the structure of the fcc array. Due to this correlation, the color of IOHs will be strictly discussed according to their Bragg peak position at constant angle, namely at normal incidence, in Chapter 5.

This chapter presented silica particles with a size of 415 *nm* assembled in a hexagonal crystal structure, which exhibits intense iridescence. Notably, upon normal incident light, a main Bragg peak at *ca.* 800 *nm* was observed. Although these materials exhibit intense color, they are not flexible enough to be used as a practical sensor. Therefore in the next chapter, thermoresponsive polymers and hydrogels will be developed and studied, in which subsequently an opal structure will be implemented, in order to induce structural color.

4 Linear Polymers and Hydrogels

4.1 Thermoresponsive Polymers

A number of water soluble polymers change drastically their macroscopic physical properties upon marginal changes of their environment (also called "*stimuli*").[105] This is not a new phenomenon for biologists, as in most living systems, macromolecules, proteins, and polypeptides can modulate their conformation depending on the environment.[26, 44] Synthetic polymers present the same ability to adapt or to change their conformation and hence their properties such as their interactions with a solvent under certain conditions or stimuli.[25, 106–108] Various stimuli have been reported to trigger the properties of responsive polymers, such as

- temperature,[25, 109–111]
- pH,[25, 109, 112]
- ionic strength,[25, 113]
- light,[107, 109, 114, 115]
- electrical field,[25, 107, 116]
- magnetic field,[25, 117]
- presence of chemical species.[25, 106, 109, 118, 119]

Moreover, the induced macroscopic changes such as dissolution/precipitation, swelling/collapsing or micellization/demicellization, ... *etc.* can be reversed once the trigger is removed.[120] In other terms, when an inverse stimulus is applied, the polymer chains return to their original state. Because of the polymer's ability to respond and interact with the surroundings, such responsive polymers are also called "*stimuli-sensitive*", "*environmentally-sensitive*", "*intelligent*" or "*smart*" polymers.[121] Vice versa, the observation of the macroscopic property changes of such polymers inform about the presence of the respective trigger, which is thereby detected. Therefore, smart polymers are excellent candidates for sensor devices.

4.2 Energetic Considerations

The solvent affinity of every polymer (natural or synthetic) depends on the temperature, which normally results in a variation of the solvated coil size.[105] If we consider a dissolved polymer in a suitable solvent, the polymer may become insoluble and precipitate upon decreasing or increasing the temperature.[122] Therefore, the system polymer/solvent may phase separate (*via* a first order transition[1]) upon changing the temperature. In other words, the temperature induces a transition from a one-phasic towards a bi-phasic system. We can distinguish two possible scenarios: the first one occurs by the apparition of an upper critical solution temperature (UCST) upon decreasing the temperature (Figure 4.1a), while alternatively a lower critical solution temperature (LCST) may be found, if the phase separation results from an elevation of the temperature (Figure 4.1b).

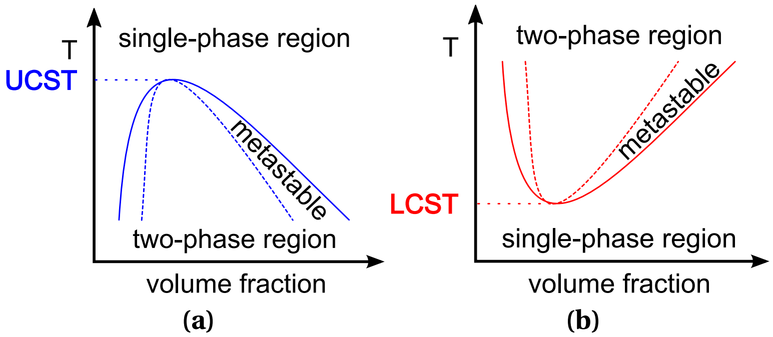

Figure 4.1: Schematic phase diagram (polymer volume fraction *vs.* temperature): binodal (plain line) and spinodal (dashed line) curves of a polymer solution, exhibiting (a) an upper critical solution temperature (UCST) and (b) a lower critical solution temperature (LCST) .

The following diagrams are usually characterized by their LCST or UCST, which are, respectively, the minimum and the maximum of the binodal (coexistence) curve. Binodal and spinodal curves are defined, respectively, as the borders between the single-phase – metastable regions, and the metastable – two-phase regions. These values are deduced from the free enthalpy of mixing $G_{mix}(T,P,\phi)$, with T as temperature, P as pressure, ϕ as volume fraction of polymer in solution.

---

[1] The first derivatives of the free enthalpy of mixing ($G_{mix}(T,P)$) are not continuous.[123]: $\left(\frac{\partial G_{mix}}{\partial T}\right)_P = -S$ and $\left(\frac{\partial G_{mix}}{\partial T}\right)_T = V$

The phase diagram depends not only on the precise chemical nature of the solvent and the polymer, but also on its molar mass. LCST-type transitions are usually assimilated to the temperature where the solutions become turbid, due to the formation of polymer-rich and solvent-rich domains, which reach a size that is big enough to scatter light. This experimental temperature is named cloud point and often measured with a simple spectrometer. In this work, cloud points were used to evaluate the relative hydrophilicity of the polymers (see Section 4.4).

The transition behavior of thermoresponsive polymers can be explained considering the second law of thermodynamics (Equation (4.1)). Accordingly, the miscibility of a polymer in a solvent requires a negative free enthalpy of mixing ($\Delta G_{mix} < 0$). In contrast, phase separation occurs when the free enthalpy of mixing becomes energetically unfavorable ($\Delta G_{mix} > 0$).

$$\Delta G_{mix} = \Delta H_{mix} - T\Delta S_{mix} \tag{4.1}$$

In a first approximation, ΔH_{mix} and ΔS_{mix} are assumed independent of the temperature. For LCST and UCST phenomena, the energetic consideration shows that in the first case, phase separation is driven by entropy, while in the second case by enthalpy. In the simplest case of an ideal solution where the enthalpy of mixing is zero ($\Delta H_{mix} = 0$), only the entropic term that is given by statistical thermodynamics governs the free enthalpy of mixing:

$$\Delta G_{mix} = -T\Delta S_{mix} \tag{4.2}$$

Although the ideal solution may be used to describe gases, it is incomplete to describe the interaction between the polymer and the solvent. Therefore, the case of regular solutions needs to be considered at least, and so the enthalpic term expresses the energy change of the non-covalent interactions, from solvent-solvent and polymer-polymer to polymer-solvent. Mostly, the interactions between two similar repeat units of a polymer and to solvent molecules are stronger than the interaction between the repeat unit and the solvent.[124, 125] Thus, the enthalpic term of mixing is positive ($\Delta H_{mix} > 0$). Also, the entropic term is positive ($\Delta S_{mix} > 0$) due to the increase of the disorder by the solubilization.

$$\Delta G_{mix} = \underbrace{\Delta H_{mix}}_{>0} - T\underbrace{\Delta S_{mix}}_{>0} \tag{4.3}$$

In this way, the free enthalpy is positive until that by heating, the entropic term overcompensates the enthalpic contribution ($T\Delta S_{mix} > \Delta H_{mix}$). This scenario is typical for the UCST behavior, for which the solubility increases by heating.

On the other hand, LCST-type polymers are a priori soluble in water due to the presence of hydrophilic groups, which can interact attractively with water molecules, often due to complementary hydrogen bonds. That way, the overall enthalpic term becomes negative ($\Delta H_{mix} < 0$). This leads to an ordering of the water molecules due to the attraction between the water molecules and the hydrophilic moieties, the water does not let the non-polar chains penetrate between them, because the attraction from hydrogen bonding is much stronger than van der Waals force. [68, 105]

These two effects leads to the formation of ordered hydration layers, which reduce the degree of freedom of the water molecules. In this case, the "*structured*" water conformation is entropically unfavorable ($\Delta S_{mix} < 0$).

$$\Delta G_{mix} = \underbrace{\Delta H_{mix}}_{<0} - T\underbrace{\Delta S_{mix}}_{<0} \tag{4.4}$$

At low temperature, the enthalpic contribution is bigger than the entropic one ($T\Delta S_{mix} < \Delta H_{mix}$), this leads to a negative free enthalpy; and so to a solubilization of the polymers chains. By increasing the temperature, the entropic term will surpass the enthalpic stabilization ($T\Delta S_{mix} > \Delta H_{mix}$) eventually inverting the sign of the free enthalpy of mixing, and hence, the solution demixes (Figure 4.2).

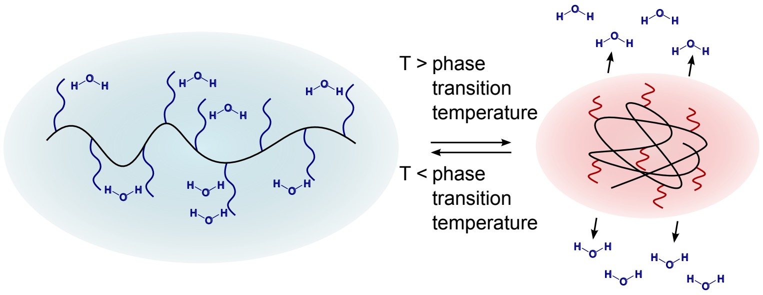
T > phase transition temperature
T < phase transition temperature
H O H

Figure 4.2: Schematic representation of OEG-bearing thermoresponsive chain below and over LCST-type phase transition temperature.

It is necessary to ponder this explanation, because in this simplified discussion, both the entropy and enthalpy of mixing were taken independent of the temperature. Another plausible explanation of LCST phase transitions would be to consider an enthalpy-driven process.[126] Indeed, at lower temperatures the polymer chains with hydrophilic groups are solubilized due to the favorable hydrogen bonds with water ($\Delta H_{mix}(T) < 0$). And for the same reasoning than before, the amphiphilic character of the polymer keeps the water in a certain ordered conformation which leads to an unfavored entropic contribution ($T\Delta S_{mix}(T) < 0$). By heating, the mobility of the water molecules increases ($\frac{dS_{mix}(T)}{dT} > 0$), reducing this way the hydrogen bonding with the polymer ($\frac{dH_{mix}(T)}{dT} > 0$). This results in a diminution of the polymer-water interactions to the profit of polymer-polymer interactions. Hence the polymer collapses, the water is expelled and the solution phase separates.

More specifically for many LCST-type polymers, the superposition of the hydrophilicity of the pendant moieties and the hydrophobicity of the polymer backbone modulates the LCST and more generally the phase transition curves. By analogy to surfactants, this ambivalence is often characterized by the hydrophilic/lipophilic balance (HLB). In this manner, the following figure (Figure 4.3) exemplifies, how the cloud point is affected by the length of hydrophilic polyethylene glycol pendent groups. When increasing the monomer's HLB, or in other words, increasing its hydrophilicity, this will favor the enthalpic term, thus requiring a higher temperature to be overcompensated by the unfavorable entropic term. In this way, the phase separation will take place at a higher temperature (CP increases). For most applications, it is not sufficient for a polymer to contain both hydrophilic and hydrophobic moieties. The composition needs to be finely balanced to lead to a phase transition which is observable between 0 and 100 °C.

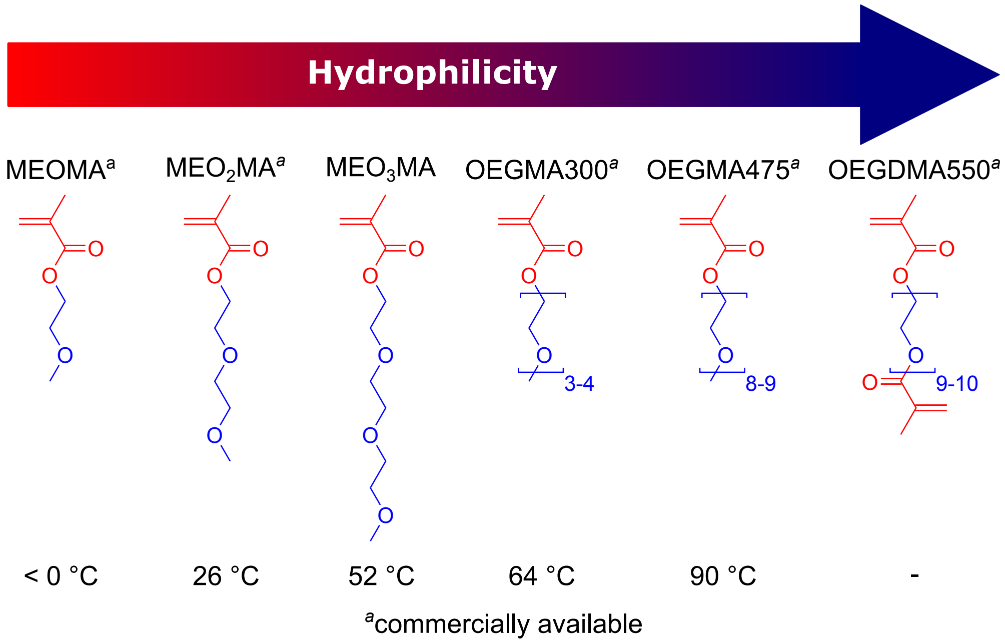
Hydrophilicity
MEOMA^a
MEO$_2$MA^a
MEO$_3$MA
OEGMA300^a
OEGMA475^a
OEGDMA550^a
3-4
8-9
9-10
< 0 °C
26 °C
52 °C
64 °C
90 °C
-
^{a}commercially available

Figure 4.3: Molecular structures of various oligo(ethylene glycol) methacrylates (OEGMAs) with the CPs of their homopolymers. Hydrophobic and hydrophilic parts are represented in red and blue, respectively.[127]

4.3 Classical Thermoresponsive LCST-type Polymers

The repeat units of thermoresponsive LCST-type polymers present commonly an amphiphilic nature. Classical LCST-type polymers other than P-OEGMAs are illustrated in Figure 4.4.

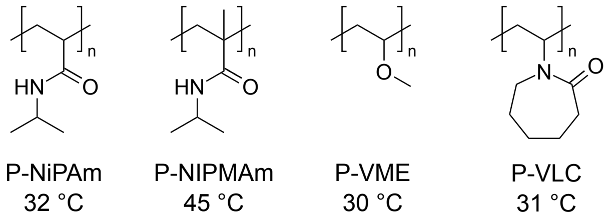
P-NiPAm
32 °C
P-NIPMAm
45 °C
P-VME
30 °C
P-VLC
31 °C

Figure 4.4: Classical thermoresponsive LCST-type polymers with their CPs. From left to right: poly(N-isopropylacrylamide) (P-NiPAm), poly(N-isopropylmethacrylamide) (P-NiPMAm), poly(vinylmethylether) (P-VME), poly(N-vinyl-ε-caprolactam) (P-VCL).

As mentioned before, LCST-polymers have been studied for more than 10 years. They all present not only different cloud points, but also different shapes of their phase diagram. The most frequent LCST-polymers in water currently present in the literature is poly(N-isopropylacrylamide) (P-NiPAm), first characterized in 1968 by a CP around 32

°C.[128] As P-NiPAm is a polyacrylamide, it has been often copolymerized with other acrylamide or methacrylamide monomers. P-NiPAm presents a typical sharp phase transition with a characteristic hysteresis shape between the heating and cooling cycle. This property was also shown to be modulated by the number of repeat units and also by the nature of the end groups. Although the hysteresis can play an interesting role for monitoring the system, for a sensor system, a well-defined transition is preferable.

In the 2000s, a new family of thermoresponsive polymer was popularized, by the work of Han, Ali and Kitano.[129–131] These polymers based on oligoethylene glycol macromonomers did not present hysteresis between the heating and the cooling cycle, in contrary to P-NiPAm.[132] As for P-NiPAm,[25] the copolymerization of other more hydrophilic or more hydrophobic comonomers - such as, acrylamide or methylacrylamide - allows to tune the CP. Concerning oligo(ethylene glycol) methylether methacrylate (OEGMA), the HLB can be precisely tuned by copolymerizing (hydrophilic) OEGMA with long OEG chains and (hydrophobic) OEGMA with short OEG chains. This convenient method extensively developed by Lutz and coworkers, and inspired on copolymers of NiPAm,[25] has allowed to adjust the CP in a range from 0 to 100 °C (Figure 4.5). For instance, around the body temperature (37 °C) the copolymer will require a composition of 8 *mol.*-% of oligo(ethylene glycol) methylether methacrylate $M_n = 475\ g \cdot mol^{-1}$ (OEGMA475) and 92 *mol.*-% of di(ethylene glycol) methylether methacrylate (MEO$_2$MA).[127, 132, 133]

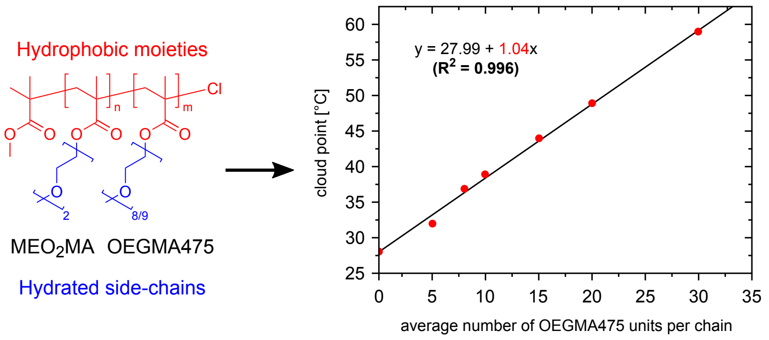

Figure 4.5: Plots of the measured CPs as a function of the theoretical average number of OEGMA475 units per chain for a series of P-MEO$_2$MA-co-OEGMA475 copolymers of various compositions. Hydrophobic and hydrophilic molecular regions in the copolymer are indicated in red and blue, respectively. Reproduced from [127].

Lutz *et al.* reported that such PEG analogues combine a rather unique set of advantages such as, thermoresponsivity, biocompatibility since they are mainly composed of OEG segments (up to 85 *wt.*-%), and also a straightforward and versatile synthesis from commercially available monomers.[127] The OEG side chain length only moderately affects the reactivity of the different monomers. Therefore, the various OEGMA derivatives can be copolymerized according to a nearly ideal azeotropic copolymerization.[127, 133, 134]

The Figure 4.3 depicts the "*classical*" OEGMA monomer derivatives. It presents their relative HLB and their CPs as homopolymers. If we look closer at the difference of OEG pendant groups, we might conclude that adding one OEG to the side chain length will increase the CP by *ca.* 25 °C. Nevertheless, this is not true anymore for OEGMA300 and OEGMA475. A possible reason could be that OEGMA300 and OEGMA475 are mixtures of several oligomers and so, cannot be precisely defined as MEOMA, MEO_2MA and MEO_3MA are. This might cause a diminution of the CP compared to polymers with one unique length of OEG side chains.

As mentioned before, this set of commercially available monomers offers a wide range of transition temperatures by combination. For this thesis, it was decided to base the thermoresponsive polymer on combinations of MEO_2MA, OEGMA475, and when a crosslinked hydrogel is desired, OEGDMA550, not only by virtue of the straightforward synthesis, but also for their presumably good biocompatibilities.[127]

4.4 LCST Determination

The most popular LCST determination methods for polymer solutions are based on scattering of light, such as turbidimetry or dynamic light scattering (DLS). These two indirect methods, turbidimetry [135] and DLS [136] are easily carried out and perfectly adapted for solutions. Phase separation of LCST-type polymers do actually not produce the apparition of two distinct superposed clear phases (*e.g.* oil/water), with one containing water and the second containing polymer. Still, the phase separation creates small domains rich in polymer (often named globule) surrounded by water molecules. Therefore, the term coil-to-globule transition will be used to designate the phase separation. Coil-to-globule transitions are observed *via* a change of the hydrodynamic radius, which is directly measured by DLS, (Section 2.5) whereas, turbidimetry illustrates the apparition of globules provoking Mie scattering that clouds the solution. By contrast, direct methods to characterize thermoresponsive polymers measure directly the enthalpy of the transition. This is, *e.g.*, the case for differential scanning calorimetry (DSC). [137–139] The heat flux determined is usually weak, as found for P-OEGMA.[42, 140, 141] Concerning insoluble polymers, such as a crosslinked hydrogels, it is necessary to use the notion of shrunk-to-swollen transition, instead of coil-to-globule transition.

4.4.1 Turbidity Measurement

Cloud points of polymer solutions can be measured with a simple spectrometer. The polymer solution is thermostated, *e.g.* by using a Peltier element. A light source irradiates the sample and a detector measures the quantity of light passing through the polymer solution at a given temperature. Below the phase transition, the solution is transparent because the polymer chains (coils) are too small to scatter the light notably (normalized transmission / 100%) (Figure 4.6a). However, above the phase transition, the polymer chains form aggregates such as globules, which are big enough to scatter the light effectively. Thus, the solution becomes turbid as the light cannot be transmitted through the solution (normalized transmission / 0%) (Figure 4.6b). The cloud point (CP) is usually defined by the temperature, where the solution becomes turbid according to naked eyes. This can in principle be attributed to the onset of the transition curves. Nevertheless, in a number of cases in the literature, the temperature at half transmittance ($T_{1/2}$) is taken as a characteristic value of the thermal transition. The comparison of these two values can be used to estimate the shape of the transition, which is, however, a priori kinetically controlled (Figure 4.6c). Throughout this work, the observed transition was always sharp, so both ways to define the transition temperature provided rather similar values.

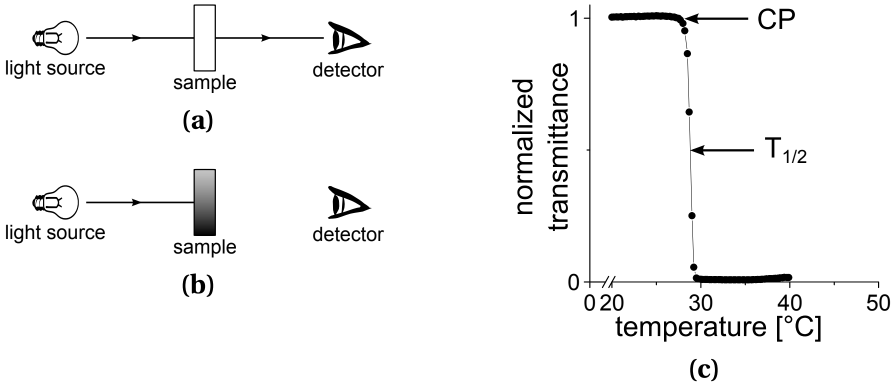

Figure 4.6: Schematic presentation of a turbidimetric measurement, (a) situation below and (b) above the phase transition. (c) transmission *vs.* temperature plot of a polymer showing a LCST-type phase transition.

4.4.2 Swelling Ratio

Many crosslinked thermoresponsive hydrogels do not become turbid by heating, unlike collapsed polymers in solution, due to highly homogenous structure, which does not scatter the light. Nevertheless, when heating hydrogels, the same thermodynamic mechanism as for soluble polymers takes place: the attractive polymer-water interactions are reduced to the profit of polymer-polymer interactions. If in polymer solutions a coil-to-globule transition is observed, for hydrogels the transition is manifested by a change from swollen to shrunk, with an expulsion of the excess water. Thus, a classical method to estimate the affinity of a hydrogel for water over the temperature is gravimetry. In practice the hydrogel is immersed and equilibrated in water at the desired temperature, taken out of the solution and weighed without residual water using a balance. That way, the swelling ratio (SR) is defined as the ratio of the weight of the hydrogel at a temperature (T) $(m(T))$, divided per the dry weight of crosslinked polymer forming the hydrogel (m_{dry}).

$$\mathrm{SR} = \frac{m(T)}{m_{dry}} \tag{4.5}$$

SR indicates the quantity of water included in the hydrogel over the temperature. The first extreme case is SR = 1, which signifies the absence of water. SR = 2 means that the same amount of water and polymer are contained in the gel. Finally, SR → ∞, describes a hydrogel swollen to infinity.

Note: other definitions of the swelling ratio exist such as

$$\mathrm{SR} = \frac{m(T) - m_{dry}}{m_{dry}} \tag{4.6}$$

$$\mathrm{SR} = \frac{V(T)}{V_{dry}} \tag{4.7}$$

$$\mathrm{SR} = \frac{V(T) - V_{dry}}{V_{dry}} \tag{4.8}$$

For the swelling ratio by volume, the dimension of the gel is measured to determine the volume (V). Nevertheless, the swelling ratio by weight is more often reported in literature as it is easier to determined.

4.5 Thermoresponsive Polymers as Analyte Sensor

For polymers or gels that are thermosensitive, the affinity of the polymer to the solvent is modulated over the temperature. In order to detect analytes by such systems, it is necessary to transduce the basic thermoresponsive to analyte-sensitive behavior. In the approach chosen in this work, analytes are detected *via* distinct affinities polymer/solvent, in dependence whether the polymer bind the analyte or not. As described below (Figure 4.7a), consider a polymer containing specific recognition sites in solution with a defined phase diagram that is characterized by LCST_1. Once analytes (here: hydrophilic) bind to the polymer, it will modify (here: increase) the HLB of the polymer, which presents now a different phase diagram with a new LCST_2 (here: $\mathrm{LCST}_1 < \mathrm{LCST}_2$). Therefore, the change from one- to two-phase systems, or vice versa, at a temperature in between LCST_1 and LCST_2 will inform about the presence of analytes (here: one-phase $\Rightarrow$ presence of analytes, two-phase $\Rightarrow$ no presence of analytes). As explained before, CPs or SRs are directly correlated to the polymer/solvent affinity. That way, their isothermal change can indicate the presence or absence of a given analyte within the appropriate temperature window (Figures 4.7b and 4.7c).

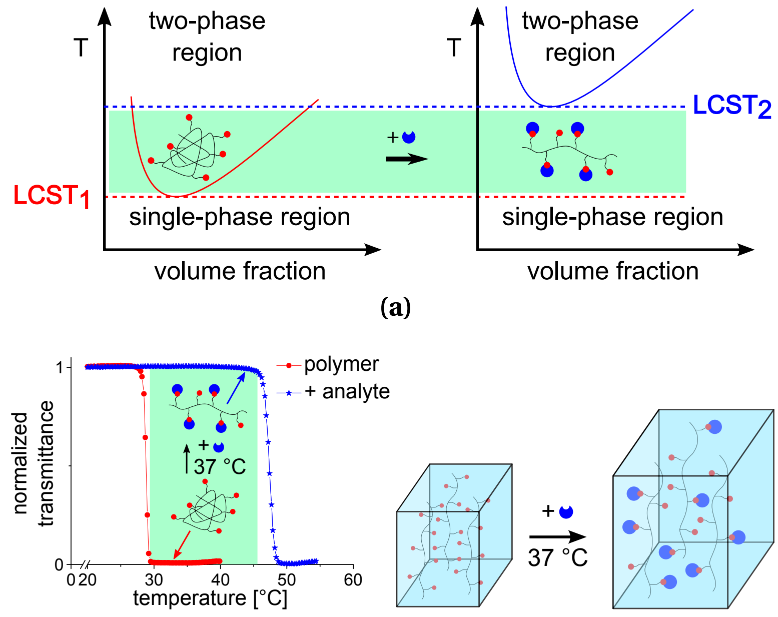
T
two-phase
region
LCST$_1$
single-phase region
volume fraction
+
T
two-phase
region
LCST$_2$
single-phase region
volume fraction
normalized
transmittance
1
0
0 20
30
40
50
60
temperature [°C]
polymer
+ analyte
+
37 °C
+
37 °C

(a)

(b)

(c)

Figure 4.7: Sensor principle explored in this thesis, based on smart hydrogels functionalized with selective recognition units (red dots): (a) schematic phase diagram in absence (left) and in presence (right) of the analyte, (b) turbidity profile and (c) swelling property change induced by the presence of the corresponding analyte (blue symbol). The green zones in (a) and (b) indicate the temperature range suitable for analyte detection.

It will be explained in detail in Chapter 5, how the change of SR can be used to induce a color shift in the case of hydrogels implemented as inverse opals, and how smart hydrogels can thus serve as autonomous sensor device. In a preliminary experiment, it is interesting to evaluate the analyte induced CP shifts of polymers in solution, as described by Buller *et al.* in the case of a thermoresponsive polymer functionalized with biotin as a recognition unit in presence of its specific binding analyte: avidin.[142] Here, the turbidimetry should inform not only about the occurrence of a binding event, but also about its strength. The next section will discuss different model systems and the effects observed.

In the following section, linear polymers and hydrogels composed of poly(oligoethylene glycol) methacrylate derivatives are synthesized *via* free-radical polymerization. These polymers may also contain crosslinkers in order to create mechanically stable covalent hydrogels: additionally, they contain selective recognition groups, in order to exhibit different solubilities in presence or in absence of the corresponding analyte. The phase transitions of linear polymers are evaluated by the analysis of their CPs, whereas hydrogels are studied by analysis of their SRs. In the next section, the synthesis of the recognition group containing monomers and the linear polymers are presented. Their solubility properties will be discussed.

4.6 Functional Recognition Unit Monomers

Specific sensor device requires two opposed characteristics: they should have specific interaction that results in the adsorption of the target analytes, while they simultaneously inhibit non-specific adsorption of other compounds. Therefore, oligoethylene glycol side chains with low-fouling properties were used as copolymer matrix: Additionally, recognition units, such as boroxol, biotin and mannose, were incorporated *via* functional monomers (Figures 4.8d, 4.9c and 4.10c). Their roles were to exhibit specific interaction with target analytes, namely 1,2-*cis*-diols, avidin and concanavalin A respectively. With these prerogatives, the smart hydrogels should adsorb analytes only if the corresponding recognition unit is present. The three pairs of recognition unit/analyte will be introduced and their syntheses described in the following.

4.6.1 Benzoboroxole – 1,2-Diols

The use of phenylboronic acid derivatives exhibits several advantages for saccharide recognition. They are known to form reversible covalent boronic esters with 1,2- and 1,3-*cis*-diol molecules, as typically found in carbohydrates or glycopolymers. Therefore, phenylboronic acids are occasionally called "*boronolectins*" due to being a remarkably stable alternative to lectins, which are proteins that can specifically bind carbohydrates (see Section 4.7.1).[143] The cyclic boronic esters are favored under basic conditions, because of the coordination of a hydroxyl anion that annihilate the electron deficiency of the boron atom. Moreover, the hydroxyl group added provokes a change of configuration from sp^2 to sp^3, which is more favorable to build esters. Benzoboroxoles (1-hydroxymethyl-phenylboronic acids) introduced by Hall and coworkers [144, 145] were described to be better binding agents for saccharide recognition than established Wulff-type boronic acids [146] (ortho-dialkylaminomethyl arylboronic acids). Therefore Schumacher *et al.* developed saccharide sensing systems that work even at physiological pH (see Figure 4.8e).[147, 148] Additionally benzoboroxoles are implemented as binding agents for glycopolymer detection as TF-antigen or gb120 of IH virus.[149, 150]

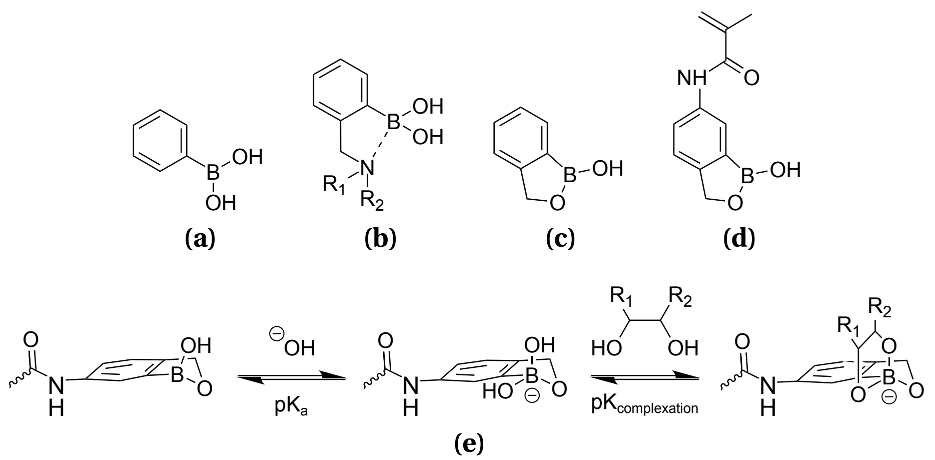

Figure 4.8: Phenyl boronic acid derivatives and benzoboroxoles, from left to right: (a) phenylboronic acid; (b) Wulff-type boronic acids: ortho-dialkylaminomethyl arylboronic acids; (c) 1-hydroxymethyl-phenylboronic acid; (d) benzoboroxole methacrylamide (**boroxol-MAm**); (e) Reaction of a benzoboroxole with 1,2-diol.[145]

In this thesis, benzoboroxole recognition units are introduced into smart hydrogels for *cis*-diol moiety sensing. First, small molecules as monosaccharides or catechols are targeted, in analogy to the work by Asher, [151, 152] Braun [34] or Kataoka,[153, 154] who used hydrogels with phenylboronic acid as recognition units. In a second step, the recognition of bigger molecules such as glycopolymers and polysaccharides is also tested in functional smart hydrogels, in order to investigate the size effect that might be a limit, particularly in the case of crosslinked hydrogels. The benzoboroxole group presents the advantage to verify if the sensors are sensitive enough to detect small molecules, but also to screen different analyte sizes, and to bind natural as well as synthetic analytes.

4.6.2 Biotin – Avidin

Molecular recognition or biorecognition between a protein and a small receptor molecule is exemplified by the ultrahigh non-covalent affinity of the well-established pair biotin – avidin.[155, 156] Avidin is a glycoprotein of 67 $kg{\cdot}mol^{-1}$ presented in egg white and composed of four subunits depicted in Figure 4.10d in magenta, blue, cyan and red. Each subunit, composed of 128 amino acids, can interact with one biotin. Biotin or vitamin H (Figure 4.9a) is a small molecule (244.31 $g{\cdot}mol^{-1}$) which exhibits a strong affinity to avidin and streptavidin. This is the strongest natural non-covalent interaction known, with a characteristic affinity (dissociation) constant of 10^{-15} $L{\cdot}mol^{-1}$. The strong interaction leads to irreversible binding, since once the complexes is formed, it remains stable, even toward changes in pH, temperature, washing or the presence of chaotropes. In order to have smart polymers that interact with avidin, biotinylated polymers were prepared. Though several synthetic methods may be suited such as polymer post functionalization,[157–159] the synthesis of an already biotinylated methacrylate monomer was opted for (Figure 4.9c), in order to have a better control of the biotin content in the functional linear polymers as well as in the crosslinked hydrogels.

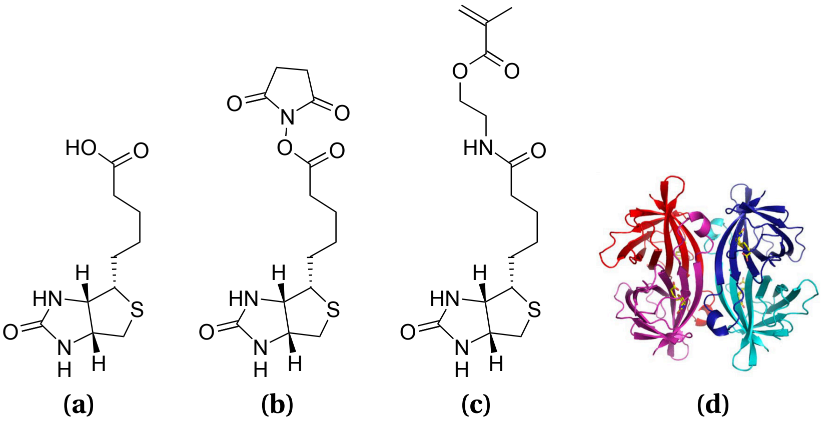

Figure 4.9: Chemical structure of; (a) biotin as anti-avidin; (b) chemically activated biotin; (c) biotin methacrylate (**biotin-MA**) as avidin receptor monomer; (d) Crystal structure of the avidin tetramer showing the subunits in magenta, blue, cyan and red where the four biotin molecules are shown in yellow.[156]

Biotin-MA was synthesized by a modified two steps procedure inspired by Liu *et al.*,[160] *via* peptide coupling between the previously prepared activated ester of biotin (Figure 4.9b) and the commercially available aminoethylmethacrylate hydrochloride at room temperature. The biotinylated methacrylate (Figure 4.9c) was then copolymerized into linear polymers and hydrogels, in order to enable selective responses to the presence of specific analytes: avidin, as highlighted by Buller and coworkers.[142, 161]

4.6.3 D-Mannose – Concanavalin A

Concanavalin A (ConA) is one of the most abundant lectins present in leguminous, notably in jack beans (*Canaoalia ensijormis*). Lectins are sugar binding proteins that reversibly and non-covalently interact with carbohydrates. They play an important role in biological events such as cell adhesion, cell agglutination or cell recognition. ConA can non-covalently interact with a wide range of saccharides, in specific cases with strong binding constants, as *e.g.* with mannose or glucose, exhibiting a affinity constant (dissociation) of 10^{-4} $L\cdot mol^{-1}$. At neutral pH, the protein is a tetramer of 102 $kg\cdot mol^{-1}$ that consists of four subunits in a tetrahedral orientation, where each subunit contains typically a Ca^{2+} ion, a transition metal ion usually (Mn^{2+}) and a saccharide binding site.[162–164] Pagé *et al.*[165] developed divalent mannosides that present stronger affinity with lectins than the monovalent mannosides, such as allyl-α-D-mannopyranose.[166] The biorecognition of D-mannose and ConA seems to be dictated by hydroxyl groups present at 3-, 4- and 6-carbon.[167, 168] Similarly to the case of **biotin-MA**, the synthesis of mannose monomers was opted, since ConA shows a similar affinity with mannose containing a 1,2,3-triazole group directly attached to the anomeric sugar center.[169] Mannose monomers having acrylate groups (**mannose-A**, Figure 4.10c) attached by click chemistry were obtained from acetylated azidomannose (Figure 4.10b) (kindly provided by A. Enzenberg and R. Bernin – University Potsdam and obtained according to the procedure described by [170]), and propargyl acrylate (see Chapter 8).

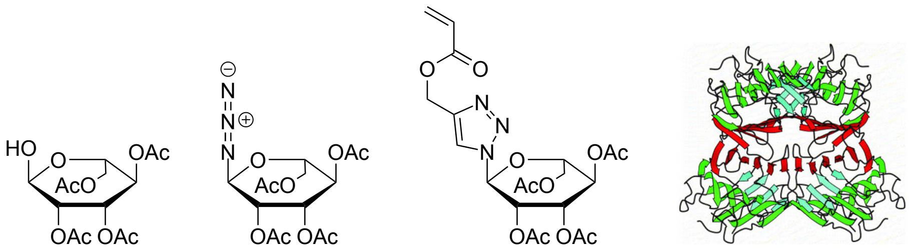

(a) **(b)** **(c)** **(d)**

Figure 4.10: Chemical formula of; (a) acetylated mannose; (b) acetylated azidomannose; (c) acetylated mannose acrylate (**mannose-A**) as concanavalin A recognition monomer. (d) Tetrameric structure of concanavalin A with subunits in red, cyan and green.[171]

Once **mannose-A** was copolymerized with OEG methacrylate derivatives to give linear copolymers or alternatively, crosslinked hydrogels, the sugar groups were deprotected with K_2CO_3 in solution, and used to build sensor devices which change their solubilities in the presence of ConA, as highlighted by Hetzer *et al.*[172–174]

4.7 Linear Copolymers

The responsive behavior was first studied for the soluble copolymers. All linear polymers shown in this work were synthesized *via* free-radical copolymerization. The copolymers always contained MEO_2MA and OEGMA475 in a ratio close to 90/10 *mol.*-%, which permits them to exhibit coil-to-globule phase transitions of the LCST-type. The recognition unit bearing monomers were incorporated to the recipe with a fraction close to 10 *mol.*-% in the feed. The reactions were conducted under standard conditions at 60 °C, over 24 *h*: azobisisobutyronitrile (AIBN) 1 *mol.*-% was used to initiate the polymerization, the solvents were ethanol, 1,4-dioxane or dimethylformamide (DMF), respectively, for **P-0** and **P-mannose**, **P-boroxol**, **P-biotin**, with a monomer concentration of 20 *wt.*-% (Figure 4.11).

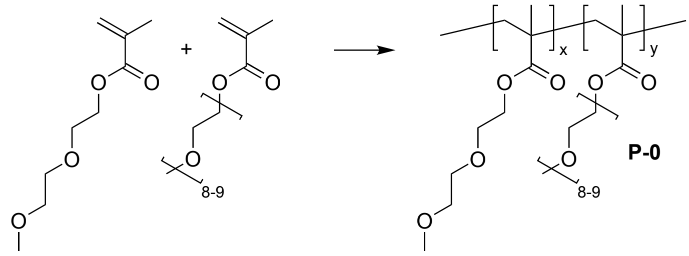

Figure 4.11: Scheme of the radical copolymerization of the binary copolymer **P-0**.

The four polymers (see Figure 4.12) were obtained after purification by dialysis and isolation using freeze drying, their chain lengths were characterized by gel permeation chromatography (Chapter 8). Table 4.1 summarizes the compositions of the four functional copolymers. The molar fractions of each monomers incorporated in the polymers were determined *via* NMR. The compositions of the methacrylic monomers in the polymers are similar to the compositions in the feeds. This is not true for acrylate contents, such as **mannose-A** that is reduced to 2 *mol.*-%. This is in agreement with the relative reactivities of the two monomer types used, acrylic and methacrylic ones. Methacrylate radicals are more stabilized than acrylate radicals due to the methyl group in the α-position of the carbonyl group. Therefore methacrylates are incorporated preferentially in the polymer.[175]

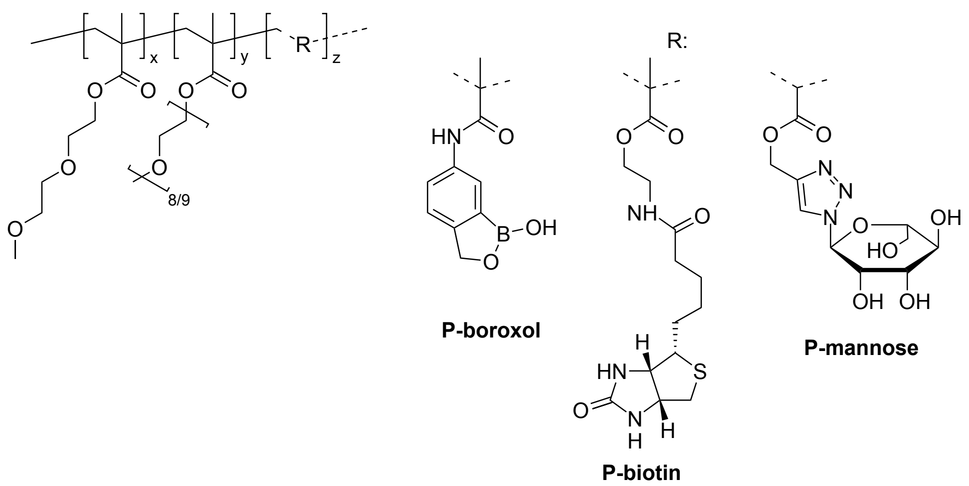

Figure 4.12: Scheme of the ternary functional copolymers: **P-boroxol**, **P-biotin** and **P-mannose**.

Table 4.1: Composition of synthesized linear copolymers **P-**.

	$MEO_2MA^{a,b}$ [*mol.*-%]	$OEGMA475^{a,b}$ [*mol.*-%]	functional monomer^{a,b} [*mol.*-%]	CP^c [°C]
P-0	92^a/ 90^b	8^a/ 10^b	-	31.0
P-boroxol	76^a/ 75^b	12^a/ 11^b	$13^{a,d}$/ $14^{b,d}$	28.0
P-biotin	78^a/ 80^b	12^a/ 10^b	$10^{a,e}$/ $10^{b,e}$	35.5
P-mannose	78^a/ 83^b	12^a/ 15^b	$10^{a,f}$/ $2^{b,f}$	39.0^g/ 43.5^h

[a] Molar fraction in the feed,

[b] Molar fraction determined *via* NMR,

[c] Cloud point determined *via* turbidimetry,

[d] **boroxol-MAm** as functional monomer,

[e] **biotin-MA** as functional monomer,

[f] **mannose-A** as functional monomer,

[g] Before deprotection,

[h] After deprotection.

These functional thermoresponsive polymers exhibit coil-globule transition around *ca.* 30 °C *via* turbidimetry (Figure 4.13). All the polymers show a sharp transition, the normalized transmittance goes from 100 to 0%, within less than 3 °C. The cloud points lead to a estimation of the relative hydrophilicity of the polymers. These differences are explained notably by the hydrophilicity of the functional monomers, which differs between the polymers. This effect is highlighted by the **P-mannose**, which is getting more hydrophilic when the acetyl groups of the incorporated **mannose-A** are cleaved by a solution of K_2CO_3. **biotin-MA** is known to be highly hydrophobic which slightly reduces the CP of the copolymers compare to a pure P-MEO$_2$MA-co-OEGMA475 with similar MEO$_2$MA/OEGMA475 ratio.[141, 142]. When the copolymers incorporate **boroxol-MAm** their hydrophilicity decrease, even if their MEO$_2$MA/OEGMA475 ratio decrease too. Indeed, at pH = 7.4 the boronic acid moieties are still partially uncharged, which confers to them a strong hydrophobicity. Additionally, it has been noted that **P-boroxol** was about to gel and to become insoluble in water if the concentration of the **boroxol-MAm** were increased (> 20 *mol.*-%). This property was instantly vanished under more basic conditions (pH = 9). Moreover, the copolymers exhibit a small hysteresis of about 2 °C. Actually oligoethylene glycol analogue polymers are known not to present a hysteresis by contrast to P-NiPAm.[132, 133]

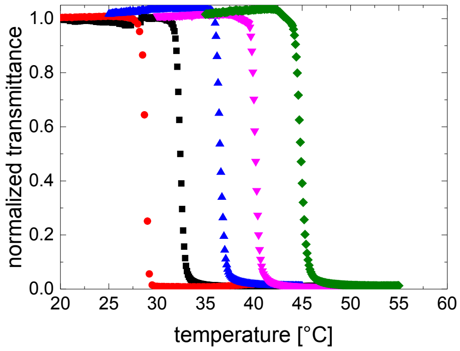

Figure 4.13: Plots of the normalized transmittance as a function of the temperature (700 *nm*, 1 $K \cdot min^{-1}$) for aqueous solutions (3 $g \cdot L^{-1}$ in PBS pH = 7.4) of **P-0** (■), **P-boroxol** (●), **P-biotin** (▲), **P-mannose-Ac** (▼) and **P-mannose** (◆).

These thermal phase transitions between linear polymers and crosslinked hydogels are not identical, especially due to the hydrophilic or hydrophobic contribution of the crosslinkers. A crosslinker such as OEGDMA550 posess its own hydrophilicity which is comparable to OEGMA475's contribution. Nevertheless, we will see that the turbidity measurements permit to control that the copolymers exhibit indeed a coil-to-globule transition (from 25 to 45 °C).

In a second step (Section 4.7.1), specific analytes will be used to induce a shift of the overall hydrophilicity upon binding. Under appropriate conditions, near the phase transition temperature, this shift will induce the phase transition.[142] The next section will discuss the effect of 1,2-*cis*-diols, avidin, and ConA on the phase transition of **P-boroxol**, **P-biotin** and **P-mannose**.

4.7.1 Analyte Tests

Benzoboroxole – 1,2-Diols

Boronic acids have a strong affinity for 1,2-diols, which might induce a change of hydrophilicity upon bonding. In order to screen the selectivity of polymers functionalized benzoboroxole, various analytes were tested. The potential analytes tested can be subsumed into four categories, namely aliphatic and cycloaliphatic 1,2-diols, monosaccharides and sugar alcohols, polysaccharides and glycopolymers, and catechols (see Table 4.2 and Figure 4.14). Additionally, control analytes devoid of vicinal-diol moieties were also investigated, as octane-1,8-diol, poly(vinyl alcohol) (PVA), and anthraquinone-4-sulfonic acid. The change of the overall hydrophilicity is studied *via* turbidimetry and correlated with the shift of the cloud points (ΔCP). The observed ΔCP is governed by the strength of the interaction of the benzoboroxole groups with the respective diol, *i.e.*, of its binding constant, as well as by the relative hydrophilicity of the analyte bound. Hydrophilic analytes increase CP, whereas hydrophobic analytes decrease CP. These shifts will be more intense for strongly bound analytes as well as for highly hydrophilic or hydrophobic analytes. Therefore, a direct comparison of the ΔCP values can be done only with analytes with similar hydrophilicities or with similar binding strengths.

Table 4.2: Shift of the cloud point (ΔCP) of a solution of **P-boroxol** (3 $g\cdot L^{-1}$) in PBS at pH = 7.4, induced by the addition of 1 equivalent (relative to the boroxole content) of a potential diol or polyol analyte.

diol	ΔCP [°C]	monosaccharide / sugar alcohol[a]	ΔCP [°C]	polysaccharide / glycopolymer	ΔCP [°C]	catechol	ΔCP [°C]
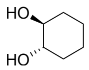 *trans*-cyclohexane-1,2-diol	3.2	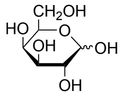 galactose	0.3	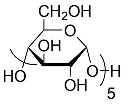 PMA	2.0	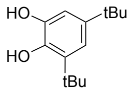 3,5-di-*tert*-butyl catechol	-28.0
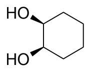 *cis*-cyclohexane-1,2-diol	4.5	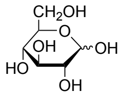 glucose	0.6	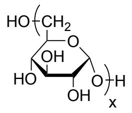 dextran	1.0	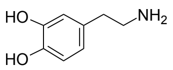 dopamine	6.7
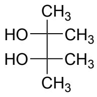 pinacol	4.0	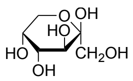 fructose	7.3	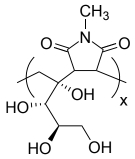 PXM-1	5.9	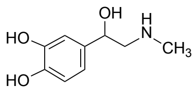 adrenaline	11.2
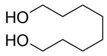 octane-1,8-diol	4.5	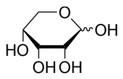 ribose	1.0	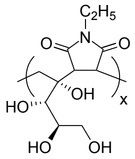 PXM-2	3.4	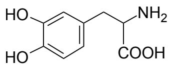 L-DOPA	18.1
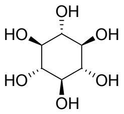 scyllo-inositol	4.0	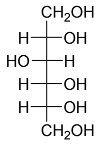 sorbitol	4.3	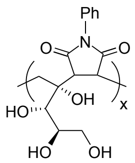 PXM-3	1.0	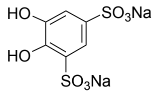 catechol-3,5-disulfonic acid	17.0
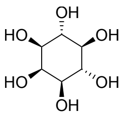 myo-inositol	3.5	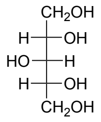 xylitol	5.4	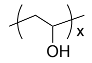 PVA	2.5	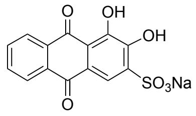 alizarin S	21.3

[a] all sugars shown in the pyranoside form that predominates in aqueous solution.

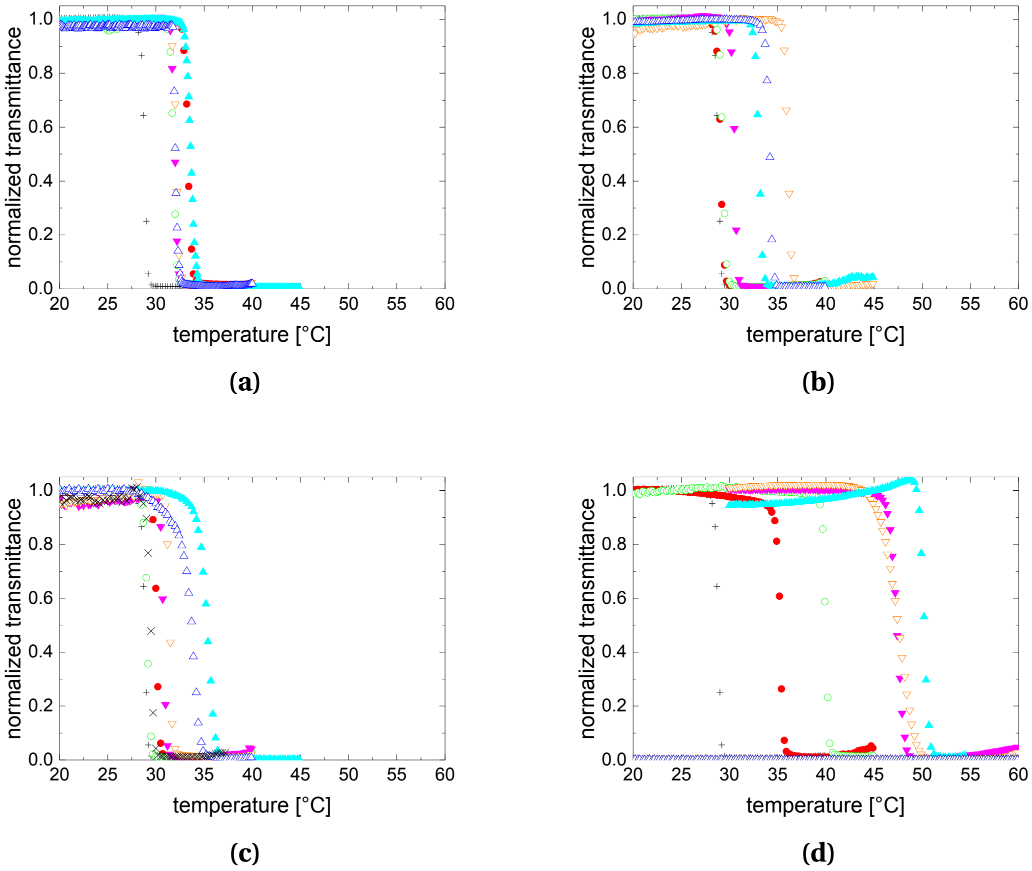

(a)

(b)

(c)

(d)

Figure 4.14: Thermoresponsive behavior of OEG-derived copolymers in aqueous solutions (3 $g{\cdot}L^{-1}$in PBS, pH = 7.4) followed by the temperature dependent normalized transmittance at 700 *nm*, and run with rates of 1 $K{\cdot}min^{-1}$; changes in the heating curves of functionalized **P-boroxol** induced by the addition of selected analytes (1 equivalent relative to the boroxole content, see Table 4.2): (a) no additive (+), *cis*-cyclohexane-1,2-diol (●), *trans*-cyclohexane-1,2-diol (○), scyllo-inositol (▼), myo-inositol (▽), octane-1,8-diol (▲) and pinacol (△); (b) no additive (+), galactose (●), glucose (○), ribose (▼), fructose (▽), sorbitol (▲) and xylitol (△); (c) no additive (+), anthraquinone-2-sulfonic acid (●), PMA (○), dextran (▼), PVA (▽), PXM-1 (▲), PXM-2 (▽) and PXM-3 (×); (d) no additive (+), dopamine (●), adrenaline (○), L-DOPA (▼), catechol-3,5-disulfonic acid (▽), Alizarin S (▲) and 3,5-di-*tert*-butyl catechol (△).

First of all, as demonstrated by the differing ΔCP values within the set of inositols, sugar alcohols and monosaccharides investigated, which all have similar hydrophilicities, their complexation by the boroxole-functionalized thermo-responsive polymer shows some specificity. Still, within the group of the aliphatic and cycloaliphatic diols, the differences between the ΔCP values are small. For instance, the difference between *cis*- and *trans*-cyclohexane-1,2-diol amounts hardly to more than 1 °C, while virtually no difference is seen for the two inositol isomers, of which only one contains a *cis*-1,2-diol motif. Also, the ΔCP values of *cis*-cyclohexane-1,2-diol and the aliphatic 1,2-diol pinacol as well as octane-1,8-diol differ only marginally. This implies that the selectivity of the boroxole groups in **P-boroxol** for complexing with *cis*-1,2-diols, compared to other diols, is a priori limited. Within the group of monosaccharides and sugar alcohols, complexation by **P-boroxol** shows higher specifity. While galactose, glucose and ribose induce only marginal changes of CP, fructose provides the highest ΔCP value of all low molar mass diols tested. The differences can be explained by the respective binding strengths with boronic acids, as sorbitol, xylitol and fructose exhibit considerably higher binding constants than galactose, glucose and ribose. [35, 145, 176, 177]

Also, glycopolymer PXM-1 derived from xylitol induces a marked increase of CP and thus interacts strongly with **P-boroxol**, while the ΔCP values induced by the other polymers poly(vinyl alcohol), a 1,3-diol analogue, dextran and PMA (both polymerized forms of glucose) are much smaller, despite their high hydrophilicities. The decreasing ΔCP values within this copolymer series as PXM-1 > PXM-2 > PXM-3 presumably reflect the decreasing overall hydrophilicity of these glycopolymers rather than decreasing affinities for the boroxole group, as all bear the identical polyol binding motif. The strongest effects on the cloud point were found when adding catechols (Table 4.2). The observed ΔCP values can be easily correlated with their relative hydrophilicities. While the interaction with the strongly hydrophobized 3,5-di-*tert*-butylcatechol basically reduces CP to 0 °C, *i.e.*, renders the polymer water-insoluble, the biogenic catechols studied, which lack the hydrophobic *tert*-butyl substituents, increase the CP of **P-boroxol** in the order of their relative hydrophilicity, *i.e.*, dopamine < adrenaline < L-DOPA. However, not only the hydrophilicity of the catechol, also the strength of the binding plays an important role for modulating CP, as the effect of Alizarin S exemplifies. While being less hydrophilic than catechol-3,5-disulfonic acid, Alizarin S is nevertheless more effective in increasing ΔCP (21 °C compared to 17 °C), whereas the addition of the analoguous anthroquinone-4-sulfonic acid, lacking the catechol binding motif, does virtually not affect CP of **P-boroxol** at all (ΔCP = 0.2 °C).

It was also verified whether the CP modulation by the various diol analytes is truly due to their interaction with the boroxole groups incorporated into the thermo-responsive polymer, and not due to unspecific interactions with the OEG-derived polymer matrix. Therefore, the reference copolymer **P-0**, which does not contain the benzoboroxole moiety, was exposed to low as well as high molar mass analytes that show strong interaction with the functionalized analogue **P-boroxol**, namely the catechol Alizarin S and glycopolymer PXM-1. As illustrated in Figure 4.15, the addition of these compounds to **P-0** induces only very small CP shifts in contrast to the situation encountered for **P-boroxol**, thus confirming that the boroxole group is responsible for its strong interaction with the diols.

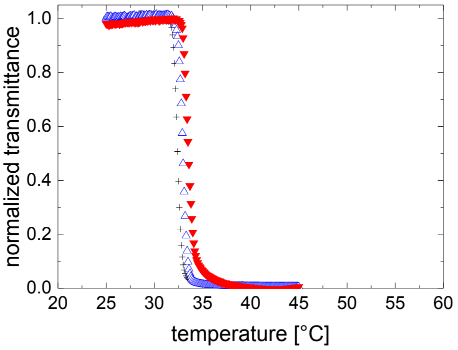

Figure 4.15: Thermoresponsive behavior of OEG-derived copolymers in aqueous solutions (3 $g \cdot L^{-1}$in PBS, pH = 7.4) followed by the temperature dependent normalized transmittance at 700 *nm*, and run with rates of 1 $K \cdot min^{-1}$; changes in the heating curves of functional **P-0** induced by the addition of selected analytes (1 equivalent relative to the boroxole content in the functionalized analogue **P-boroxol**): no additive (+), Alizarin S (△), PXM-1 (▼).

Biotin – Avidin

Buller and coworkers highlighted the ability of avidin to modulate the CP of thermoresponsive copolymers, which incorporates MEO_2MA, OEGMA475 and biotinyl-3-aminopropyl methacrylamide.[141, 142] Analogously, as an initial test, the binding assay was reproduced using **P-biotin** containing **biotin-MA**, since its synthesis was more straightforward. Moreover the use of a methacrylate instead of a methacrylamide derivative should help to obtain the same composition in feed than incorporated into the polymer.

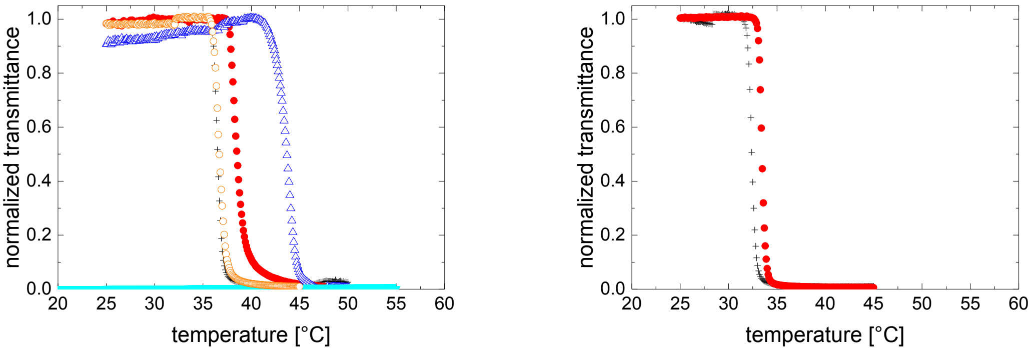

(a)

(b)

Figure 4.16: Thermoresponsive behavior of OEG-derived copolymers in aqueous solutions (3 $g\cdot L^{-1}$in PBS, pH = 7.4) followed by the temperature dependent normalized transmittance at 700 nm, and run with rates of 1 $K\cdot min^{-1}$; changes in the heating curves of (a) functionalized **P-biotin** and (b) non-functional **P-0** induced by avidin: (a) 0 $g\cdot L^{-1}$ (+), 0.5 $g\cdot L^{-1}$ (●), 5 $g\cdot L^{-1}$ (△), 10 $g\cdot L^{-1}$ (▼), BSA 50 $g\cdot L^{-1}$ (○); (b) 0 $g\cdot L^{-1}$ (+), 5 $g\cdot L^{-1}$ (●).

CP of the copolymer containing 10 *mol.*-% **biotin-MA** could be gradually shifted upon the addition of the specific analyte partner namely, avidin, with ΔCP = 2.0 °C and ΔCP = 5.7 °C, respectively for 0.5 $g\cdot L^{-1}$ and 5 $g\cdot L^{-1}$ (Figure 4.16a). Finally the polymer becomes insoluble when the concentration of avidin surpasses 10 $g\cdot L^{-1}$, presumably due to multiple binding of the avidin molecules (composed four anti-biotin binding sites) with the copolymer. Importantly, no effect is observed when adding bovine serum albumin (BSA), ΔCP < 0.1 °C (Figure 4.16a).

Additionally, the crutial role of **biotin-MA** was verified by exposing the reference polymer **P-0** devoid of **biotin-MA** to avidin. **P-0** in presence of avidin (Figure 4.16b) exhibits only a weak shift of CP of **P-0** (ΔCP = 1.0 °C). Thus, Figure 4.16 confirms that potential unspecific interactions between avidin and the OEG-derived polymer matrix do only marginally affect the CP, whereas the specific biotin – avidin interactions are responsible of the change of CP of **P-biotin**.

This model system takes advantages of the strong binding constant between biotin and avidin. Large biomolecule as avidin, which exhibit a size in the range of (5.6 × 5.0 × 4.0 nm^3) induces a strong ΔCP upon binding. The binding constant of biotin-avidin is exceptionally high, by contrast with classical biological affinities that are closer to 10^{-3}. Consequently, it was interesting to investigate also systems with similar protein size but with weaker binding constants.

D-Mannose – Concanavalin A

Most sensors devices based on copolymers containing mannose moieties take advantage of the strong affinity between mannose and the lectin, namely concanavalin A (ConA). The mannose-ConA non-covalent affinity is weaker that the one of the biotin-avidin system ($K_d = 10^{-4}$ for mannose-ConA *vs.* $K_d = 10^{-15}$ for biotin-avidin). **P-mannose-Ac** exhibits a CP around 39 °C, which is shifted to 43.5 °C when the mannose groups are deprotected (**P-mannose**). Similarly to biotin – avdin system, ConA disposes of four anti-mannose receptor sites. When ConA is added, first it increases the CP of **P-mannose** (shifting CP by 1.5 °C at 5 $g \cdot L^{-1}$), then it makes **P-mannose** insoluble when its concentration surpasses 10 $g \cdot L^{-1}$ (Figure 4.17a).

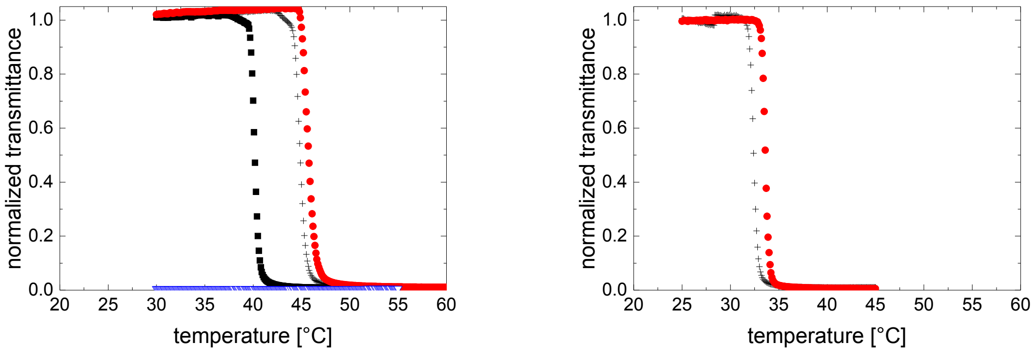

(a) (b)

Figure 4.17: Thermoresponsive behavior of OEG-derived copolymers in aqueous solutions (3 $g \cdot L^{-1}$in PBS, pH = 7.4) followed by the temperature dependent normalized transmittance at 700 *nm*, and run with rates of 1 $K \cdot min^{-1}$; changes in the heating curves of (a) functionalized **P-mannose-Ac** and **P-mannose** and (b) non-functionalized **P-0** induced by ConA: (a) **P-mannose-Ac** (■), **P-mannose** (+), in presence of 5 $g \cdot L^{-1}$ ConA (●), in presence of 10 $g \cdot L^{-1}$ ConA (▽); (b) **P-0** (+), in presence of 10 $g \cdot L^{-1}$ ConA (●).

The selectivity of functionalized copolymers were already verified for the other model systems *i.e.* boroxole and biotin moieties. Accordingly, oligoethylene glycol monomers and their low-fouling properties seem also to provide a sufficient inhibition of ConA molecules. Figure 4.17b highlights the small ΔCP provoked by ConA on **P-0** of 1.0 °C, whereas with similar a concentration, ConA makes **P-mannose** insoluble.

The three model systems – benzoboroxole, biotin, mannose – are a good selection for flexible and polyvalent sensor systems. They present strong ΔCP modulation in the presence compared to in the absence of their specific analyte partners – 1,2-diols, avidin, ConA – while OEG-derived matrix is basically inert to the analytes.

4.8 Hydrogels

4.8.1 Synthesis

Since the linear copolymers are composed of 90 *mol.*-% of oligoethylene glycol methacrylate derivatives to achieve biocompatibility and low-fouling, a bifunctional oligoethylene glycol derivative was used as crosslinker, which bears two polymerizable groups, here methacrylates.
A wide range of oligoethylene glycol dimethacrylates (OEGDMAs) is commercially available. OEGDMAs also possess an amphiphilic structure, often named bolaform due to their symmetry, which consists in a hydrophilic body and two hydrophobic ends. The incorporation of these comonomers may influence the overall hydrophilicity of the crosslinked hydrogels in function of their own HLB (see Figure 4.3). Nevertheless, thermoresponsive behavior should be preserved if the variations of the hydrophilicity stay moderate.

The crosslinker used was OEGDMA550 (M_n= 550 $g{\cdot}mol^{-1}$) composed of about 9-10 ethylene glycol groups. Using longer OEG side chains should, on the one hand, help for the swellability of the hydrogels. On the other hand, this would shift the temperature of the swollen-to-shrunk transition notably due to their highly hydrophilic chains (Section 4.3).

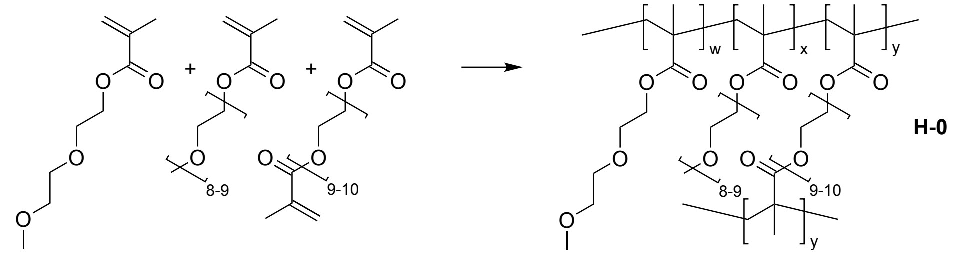

Figure 4.18: Scheme of the radical copolymerization to give the ternary copolymer hydrogel **H-0**.

The hydrogels were made in a mold of two microscope glass plates separated by a spacer made of paraffin film (also known as parafilm). This rather simple setup led to transparent hydrogels ($\approx 2\ cm \times 5\ cm \times 110\ \mu m$). The hydrogels were also polymerized *via* radical polymerization (Figure 4.18), but this time, the reactions were initiated by UV-light using the photoinitiator Irgacure 2010. This photoinitiator was chosen because the emitted UV-light is situated in the UV A range (315-400 *nm*), where glass is permeable. The glass plates were previously cleaned and hydrophilized following the same procedure as for silica crystallization (Chapter 3), using piranha solution: 1:1 v/v mixture of hydrogen peroxide (H_2O_2) and sulfuric acid (H_2SO_4). The polymarizable premix, which consists of MEO_2MA, OEGMA475, OEGDMA550, initiator and solvent was injected into the mold, and polymerized to give a thin hydrogel film of the desired dimensions (Figure 4.19). After demolding (see Chapter 8) the free standing hydrogels are released in the reaction solvent. In order to remove the non-reacted compounds, the hydrogels were washed with pure reaction solvent, and then several times with water.

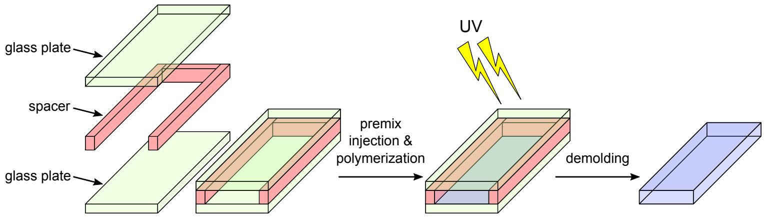

Figure 4.19: Scheme of the hydrogel molding process of monomer injection followed by polymerization under UV-light.

The concentration of the monomers used in the premix was chosen to correspond to the water content of the hydrogel in the final state (30 *wt.*-%). This avoids big volume changes of the hydrogels during the washing steps. This should help to preserve the initial structure of the IOHs implemented by the silica templates. A strong swelling or collapse of the IOHs upon solvent change to aqueous solution could dramatically distort the regular microstructure and so make the structural color vanish.
Therefore, the solvents selected to conduct the polymerizations swell the hydrogel with a similar magnitude than pure water, even if sometimes it was necessary to use a highly polar solvent such as DMF to dissolve the monomers.

First, a series of hydrogels with various crosslinker contents was synthesized (see Figure 4.18), in order to study the influence of the crosslinker content on the swelling of the hydrogels. Table 4.3 summarizes the composition of the synthesized hydrogels series (**H-0**).

For evaluating the results, additional parameters beyond the swellability had to be considered, such as the mechanical stability.
However, the stability increases with increasing crosslinker density, whereas the swellability decreases. Therefore, a good balance between swellability and stability had to be found. For these reasons, the optimal compositions of the hydrogels will be discussed in the next section, with regards to their swelling ratio and their stability (see Figure 4.20).

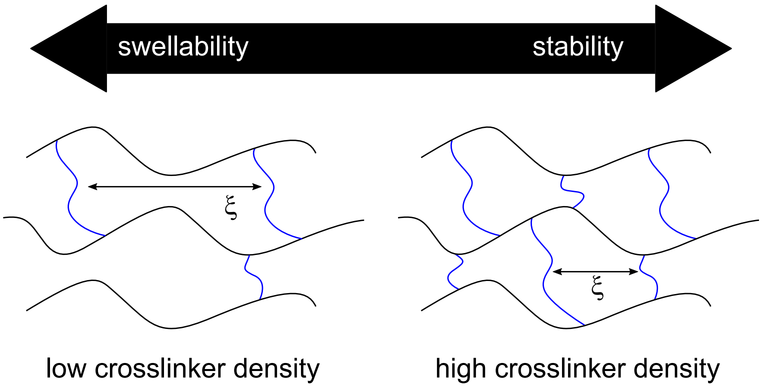

Figure 4.20: Schematic representation of hydrogels (——) with low and high amounts of crosslinker segments (——), ξ being the average mesh size.

4.8.2 Swellability and Mechanical Stability

Analytical methods such as NMR spectroscopy were not conclusive to characterize the hydrogels, since this technique requires good dilution of the polymer chains. This is prevented by the covalent crosslinks. Since in Section 4.5 the NMR analysis of the linear copolymers show almost no changes for compositional shifts, the compositions are assumed to be the same in the feed than in polymer.

Table 4.3 compiles the influence of the crosslinker density on the swelling ratio SR and mechanical stability of the hydrogels. Too low mechanical stability is found for hydrogels crosslinker densities below 15 *wt.*-%. (**H-0f- H-0i**).

For the hydrogels with sufficient stability, *i.e.* when containing 20 *mol.*-%of crosslinker and more, a general tendency is seen: the more hydrophilic OEGMA475 is incorporated, the more swellable are the hydrogels (**H-0a** - **H-0e**). The important quantities of crosslinker were presumably not fully effective as they may form loops, which do not contribute to the crosslinking.

Table 4.3: Composition of hydrogels (**H-0**).

	MEO_2MA^a [*mol.*-%]	$OEGMA475^a$ [*mol.*-%]	$OEGDMA550^a$ [*mol.*-%]	SR^b [%]	stability
H-0a	80	0	20	1.4	stable
H-0b	70	10	20	2.0	stable
H-0c	60	20	20	2.5	stable
H-0d	50	30	20	2.9	slightly stable
H-0e	40	40	20	3.3	slightly stable
H-0f	85.3	12.2	2.5	-	instable
H-0g	83.1	11.9	5	-	instable
H-0h	78.8	11.2	10	-	instable
H-0i	74.4	10.6	15	2.2	slightly stable
H-0j	65.6	9.4	25	1.6	stable

[a] Molar fraction in the feed,
[b] Swelling ratio at 25 °C.

Additionally, it is seen that at constant $MEO_2MA/OEGMA475$ ratio, the diminution of the crosslinker density increases the swellability of the hydrogels. For instance at 25 °C, the SR of **H-0j**, **H-0b** and **H-0i**, are 1.6, 2.0 and 2.2, respectively.

This behavior had been expected, as hydrogels containing a low crosslinker content exhibit larger meshes. These meshes, characterized by their average size (ξ) can be filled by more fluid, which lead to high SR.
By contrast, hydrogels with a higher crosslinker density are more rigid systems with smaller meshes. This reduces the amount of water that can be accommodated in the hydrogel, and thus their SRs (Figure 4.20).

Additionally to the general effects concerning swellability and stability, we note that hydrogels made of monomer bearing OEG side chains exhibit broad thermal swollen-to-shrunk transitions (Figure 4.21). This swelling behavior of P-OEGMA-hydrogels is opposed to the one of P-NiPAm-hydrogels, which show a sharp swollen-to-shrunk transition almost coinciding with the coil-to-globule transition of an equivalent linear

P-NiPAm.[178] This seems characteristic for P-OEGMA-hydrogels. The groups of Tang [42, 179, 180] and Hu [181] investigated the transition of microgels. Tang studied microgels made of P-NiPAm, whereas Hu focused on P-OEGMAs microgels. Both using OEGDMA as crosslinker, they observed that increased quantities of OEGs broaden the swollen-to-shrunk transition of the microgels.

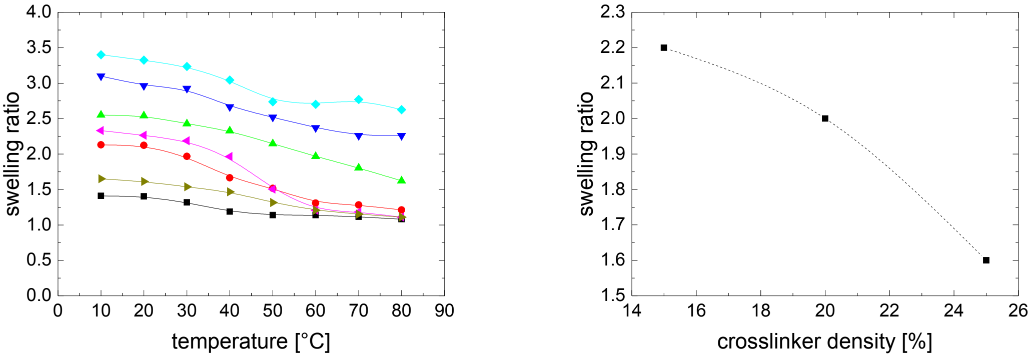

(a) **(b)**

Figure 4.21: Swelling behavior of the P-OEGMA-hydrogels series (**H-0**); (a) Plots of the normalized swelling ratio as function of the temperature in aqueous solutions (PBS pH = 7.4): **H-0a** (■), **H-0b** (●), **H-0c** (▲), **H-0d** (▼), **H-0e** (◆), **H-0i** (◀), **H-0j** (▶); (b) Plot of the swelling ratio at 25 °C as a function of the crosslinker density (**H-0i**, **H-0b** and **H-0j**).

Broad swelling transitions are not necessarily a disadvantage for sensor devices. If the aim is to design a binary system (yes-no), which indicates that pathogens are present above a certain threshold value or not, then thermosensitive systems with a sharp thermal swelling transition should be chosen. In contrast, if a sensing platform should also be able to quantify the pathogens, then hydrogels with a broad swelling transition should be preferred.

Figure 4.21b highlights for samples **H-0i**, **H-0b** and **H-0j** the swelling behavior of the P-OEGMA-hydrogels with different crosslinker density. At 25 °C, a diminished crosslinker density increases the swelling ratio of the hydrogels. Nevertheless, a minimum of 20 *mol.*-% of crosslinker was necessary to obtain a hydrogel film that was mechanically stable enough when swollen in water. The other hydrogels (**H-0f** - **H-0i**) could not be handled without ripping them up.
Sufficient mechanical stability is a crucial criterion, in particular considering that finally the inverse opal hydrogels will possess a porous structure. This should resist

various treatments, such as by HF, temperature, solvent or pH changes ..., *etc.*, let alone from the stress due to handling. Therefore, **H-0b** was chosen as the basis formulation to elaborate the functional hydrogels. It possesses the minimum crosslinker density to provide still sufficient stability.

4.8.3 Functionalized Hydrogels

Stable and flexible hydrogel formulations were established in the preceding sections. In order to obtain additionally functionalized hydrogels, some settings have to be adapted to the recognition units to be incorporated (see Figure 4.22). Even if the syntheses of the functional hydrogels follow in the main lines the procedure established in Section 4.8.1, the reaction solvent needed to be adapted. This is due to insolubility of recognition unit monomers in water, particularly with **biotin-MA**, which is only soluble in DMF.

Table 4.4 gives an overview of the synthesized hydrogels. It informs on their compositions in the feed, and in the polymer. As the functional monomers contain N or S, in contrast to the OEGMA derivatives, their contents were estimated *via* CHNS elemental analysis (EA).

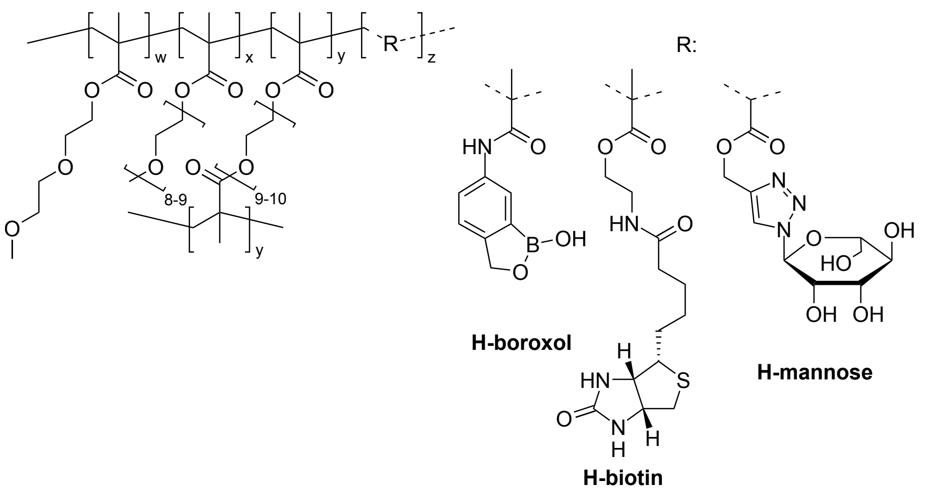

Figure 4.22: Scheme of the quaternary functional copolymer hydrogels: **H-boroxol**, **H-biotin** and **H-mannose**.

The incorporation of the functional monomers is similar for hydrogels and for linear polymers : **boroxol-MAm**, and **biotin-MA** are completely converted, whereas **mannose-A** is only incorporated in the polymer with 20 *mol.*-% (see Section 4.7).

Figure 4.23 shows the swelling ratio profiles of the functionalized hydrogels. They exhibit the same broad transitions than the hydrogels devoid of functional groups (**H-0**). Additionally, the relative hydrophilicities of the hydrogels due to different functional comonomers can also be observed, even if these differences are relatively low. At 25 °C, they were maximum for **boroxol-MAm** with SR reduced by 13 *wt.*-%.

Table 4.4: Composition of synthesized hydrogels **H-**.

	MEO_2MA^a [*mol.*-%]	$OEGMA475^a$ [*mol.*-%]	$OEGDMA550^a$ [*mol.*-%]	functional monomer^{a,b} [*mol.*-%]	SR^c
H-0	68^a	12^a	20^a	-	2.0
H-boroxol	62^a	11^a	20^a	$7^{a,d}$ / $7.4^{b,d}$	1.8
H-biotin	57^a	10^a	19^a	$14^{a,e}$ / $8.7^{b,e}$	1.9
H-mannose	57^a	10^a	19^a	$14^{a,f}$ / $3.5^{b,f}$	2.0^g / 2.1^h

[a] Molar fraction in the feed,
[b] Molar fraction determined *via* elemental analysis,
[c] Swelling ratio at 25 °C,
[d] **boroxol-MAm** as functional monomer,
[e] **biotin-MA** as functional monomer,
[f] **mannose-A** as functional monomer,
[g] Before deprotection,
[h] After deprotection.

All the hydrogels exhibit broad volume transitions from SR ≈ 2 to SR ≈ 1 (Figure 4.23). This almost corresponds to a deswelling of water content from ≈ 50 *wt.*-% to ≈ 0 *wt.*-%. A priori for analyte detection, a volume transition from a more swollen state is desirable, since the analytes will penetrate more easily in a highly swollen matrix. Nevertheless, "*rather hydrophobic*" formulations that do not swell excessively are needed to keep a sufficient refractive index contrast between the solvent and the matrix, (see Chapter 5). In the case of an inverse opal hydrogel, the wide amplitude of the volume transitions, 50% of weight expelled over 70 °C heating, should be strong enough to provoke a contraction of their crystal planes. Therefore, these formulations were also chosen for their changes of SR, which should directly determine their sensitivities.

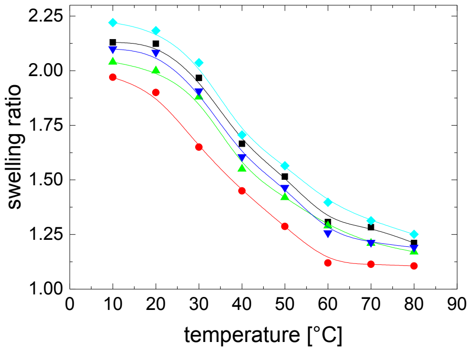

Figure 4.23: Plots of the normalized swelling ratio as a function of the temperature for aqueous solutions (PBS pH = 7.4) of **H-0** (■), **H-boroxol** (●), **H-biotin** (▲), **H-mannose-Ac** (▼), **H-mannose** (◆).

The relative hydrophilicities of the hydrogel are evident in Figure 4.23. The highest SRs are obtained with **H-mannose**, then almost superimposed are the SRs of **H-0** and **H-mannose-Ac**. This shift is due to the intrinsic hydrophilicity of mannose, which makes the hydrogel swell by 3 *wt.*-% at 25 °C, once deprotected. **H-biotin** and **H-boroxol** show lower SRs, which indicate that their functional groups shrink the hydrogel by 5 *wt.*-% and 13 *wt.*-% respectively, at 25 °C.

It is important to note that the gels should be stored in aqueous solution, otherwise they will dry out during a couple of hours due to their low thickness. Drying will provoke irreversible cracks and scars that could lead to the loss of color when the hydrogels are implemented in form of an inverse opal.

In conclusion, the synthesized functional hydrogels are transparent and exhibit a satisfactory mechanical stability for a crosslinker density of 20 *mol.*-%. This enables their manipulation and their extended storage in PBS solution (more than 2 years at least). Additionally, they possess high flexibility, which makes them good candidates for IOHs that show high sensitivities not only upon temperature changes, but also in the presence of analytes.

5 Inverse Opal Hydrogels

The previous chapters described, that thermosensitive hydrogels can be an interesting platform for analyte sensing, namely, that analytes can induce coil-to-globule transition for linear polymers which include specific recognitions moieties. In this chapter, I will discuss how it is possible to combine responsive hydrogels and 3D structure silica opals and their color to obtain inverse opal hydrogels (IOHs).

With the aim of tuning the swellability and also the color shift properties, the formulation of the polymer mixture was first studied by evaluating mechanical stability, thermal properties, and refractive index contrast. First, these parameters will be taken into consideration in the next section. Once thermosensitive IOHs were studied and characterized, other monomers were introduced in the IOHs recipes, in order to create specific recognition units. The second section of the chapter will then show IOHs with color changes induced upon analyte binding, with a view to develop sensor devices even for large biomolecules. Thus, in the hydrogel experiments, a range of IOHs with various recognition units as model systems were developed, including:

- Benzoboroxole – 1,2-diols
- Biotin – Avidin
- D-Mannose – Concanavalin A

The goal of this catalogue is to demonstrate the high potential of the use of IOH as a generally applicable, autonomous diagnostic sensor system.

5.1 Opal *vs.* Inverse Opal

To build photonic crystal (PhCs) with an opal form, two general strategies are possible: the use of opals or inverse opals. In the first case, opals made of PS or PMMA are usually made with a similar procedure than for the silica opals, by vertical deposition.

By contrast, inverse opals are the negative-replica of the opals that are used as a interim scaffold and finally removed.

Regarding "*traditional*" smart opal hydrogels, the synthesis usually proceeds by precipitation polymerization or emulsion polymerization of thermoresponsive polymers, such as P-NiPAm, before the particles are self-assembled (see Figure 1.6 - opal).[16, 30, 181–183]

In the case of IOHs, monodisperse particles of silica are first assembled toward an opal photonic crystal. A monomer mixture is subsequently infiltrated into the voids of the opal and polymerized. This produces a hybrid non-porous material made of particles embedded in a polymer matrix (see Figure 1.6 - hybrid material). Then, the sacrificial template is removed by dilute hydrofluoric acid in the case of silica particles, or by simple solvent dissolution in the case of non-crosslinked particles, or even by calcination if PS or PMMA particles are used (see Figure 1.6 - inverse opal).[27, 33, 34, 45, 184–186] When the template is removed, only the matrix remains and instead of the template voids appear, which are filled by air, solvent or water, in view to be compatible with biomolecules. Note that the template and the matrix should be chemically different, so that the template can be removed without affecting the matrix. Asher and coworkers showed that a hybrid hydrogel with embedded polystyrene colloids in a polymer matrix (Figure 1.6 - hybrid material) could also be used as sensor. Nevertheless, their non-porous structure does not allow the diffusion of large analytes.[31, 35, 37, 40, 151, 152, 187, 188]

The structures of opals and IOHs are rather similar, the main difference is the porosity. In the case of an fcc assembly, the atomic packing factor (APF) of the opal (hydrogels or templates) which is defined by the ratio of the volume occupied (here: particles' volume) against the lattice volume is equal to 74%. This supposes only 26% of opals is open space. For IOHs, the monomers building the hydrogels are infiltrated and polymerized in the 26% of void space. Thus, the removal of the opal template creates 74% of vacant space.

Although opal structures are more direct and simpler to elaborate, IOH structures were developed in order to enable a better diffusion of analytes. IOH pores tend to maximize the sensitivity of the gels, which is linked to the accessibility of the true specific surface. Indeed, large analytes cannot penetrate weakly porous gels, and accordingly interact only with the outside surface instead of the true specific surface. Their hollow structure with pores size in the range of several hundreds of nanometers should a priori allow diffusion of large molecules such as proteins or viruses into photonic crystals. Moreover, since the hydrophilic/hydrophobic change which induces the swelling/shrinking is a function of the number of bound analytes, the color shift should be bigger for materials with large accessible specific surface area such as, IOHs.

As already mentioned in the introduction, regarding physical properties, opals and inverse opals are both photonic crystals since they have a structure of distinct periodic domains with distinct dielectric constants. No matter if the PhC is an opal-type, which has spheres with a high refractive index (n_1) and voids with a low refractive index (n_2), or an inverse-opal-type, with a matrix with high refractive index (n_1) and pores with a low refractive index (n_2), as long as the difference between n_1 and n_2 is kept big enough, PhCs prevent the propagation of specific wavelengths. The influence of the refractive index contrast (Δn) and the light intensity will be discussed later. When the medium is water and the matrix is made of water swollen polymers, it might happen that the refractive index of the polymer chains and water get too close to diffract light effective.

5.2 Synthesis

Chapter 3 discussed the process to obtain self-assembled silica particles immobilized on a microscope glass plate. Accordingly, opal templates were embedded into the previously formulated polymer matrix presented in Chapter 4.

The molding process was elaborated using two microscope glass plates, one of them coated with a deposited silica opal. A spacer made of plastic paraffin film (also known as "*parafilm*") was used between the two plates to seal the mold, and so to avoid runoff of the reactive mixture. The reactive premix composed of monomers, crosslinker, UV-initiator and solvent was then infiltrated into the mold and polymerized under UV light (Figure 5.1).

It is noted that after synthesis, the color of the hybrid material appears less intense. Indeed, the refractive index contrast (Δn) is stronger for a silica opal ($n = 1.45$) surrounded by air ($n = 1.00$) than for the hybrid material where the air is replaced by the

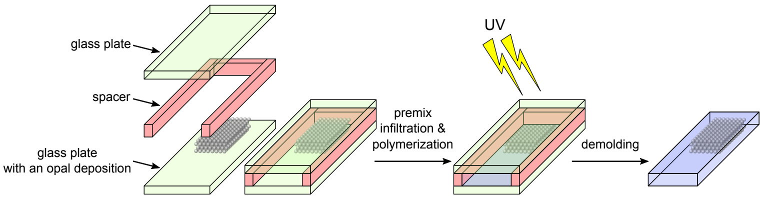
glass plate
spacer
glass plate with an opal deposition
premix infiltration & polymerization
UV
demolding

Figure 5.1: Scheme of the molding process, *via* monomer infiltration into an opal template followed by polymerization under UV-light.

polymer hydrogel.

To create the porosity, but also to establish the refractive index contrast, the silica template was dissolved by dilute aqueous hydrofluoric acid (HF)[1]. This step was carried out at least overnight, followed by several washing with ultra-pure water, in order to remove the residual traces of HF. After that, the IOHs could be stored in ultra-pure water at room temperature without showing any deterioration over two years.

The parafilm spacer ($\approx 100\ \mu m$) was also chosen to define the thickness of the whole hydrogel ($\approx 110\ \mu m$). Nevertheless, the hydrogels' thickness measured using a micrometer was quite bigger than the thickness of the spacer. This swelling is presumably caused by the pressure produced by the clamps used to maintain the mold sealed. Moreover, it is important to note that the IOHs are not fully, but only partially structured (≈ 10 *vol.*-%). The drawing below (Figure 5.2) represents a cut through the IOH, and underlines the complex structure of these materials. The first part on the left depicts the optically active part of the gel, which provides the color of the hydrogel when a sufficiently intense light source illuminates the sample. The second main part portrays the non-structured part of the hydrogel, which is required to give mechanical strength to the whole gel.

Once the silica templates were dissolved, the free-standing IOHs were immersed into water, which leads to an increase of the refractive index contrast between the polymer and the water. Consequently, the IOHs in water exhibit an intense structural color, as it was the case for the dry silica templates.

---

[1] **warning:** even dilute hydrofluoric acid (HF) has a number of physical, chemical, and toxicological properties that make it especially hazardous to handle. Strictly follow the precautions given by the material safety data sheet. Prevention of exposure or injury must be the primary goal when working with HF. However, any HF user must be intimately familiar with the appropriate first aid in case of an accidental exposure, and immediately seek medical advice.

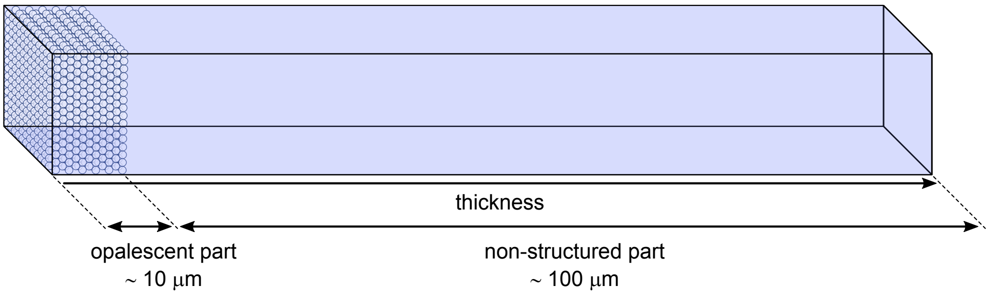

Figure 5.2: Schematic representation of the complex structure of IOH, which is composed of a structured opalescent part and a non-structured stabilizing part.

IOHs with multifunctionality were synthesized (Figure 4.22), using the optimized recipe, prior established for non-structure hydrogels, see Table 4.4.

First, as a proof the concept, soft inverse opals that exhibit a change of Bragg peaks upon a stimulus, such as temperature, solvent or pH change, will be investigate. Secondly, the model systems used in Section 4.7 will translated into IOHs. The change of IOHs' color, induced by molecular interactions will be discussed. Small molecules (1,2-diols) as well as large molecules, such as glycopolymers (PXM) and proteins (avidin and ConA), were tested.

5.3 Cryo-SEM Characterization

Since interference colors were observed, a regular structure must be present in the IOHs. Therefore, cryogenic electron microscopy (cryo-SEM) was used to analyze the integrity of the inverse structure, after dissolution of the silica opal template.
Note: SEM micrographs illustrate the geometry of the IOH at 25 °C, since the gel structure was elucidated *via* a freeze-fracturing procedure, which instantly freezes the gel with liquid nitrogen. The procedure is detailed in Chapter 8.

IOH dispose of inverse microstructure similar to the silica template (Figure 3.8), exemplarily shown in Figure 5.3 for a cut through an **IOH-boroxol** film. In the SEM micrographs, a highly porous zone of around 12 μm thickness appears on top of a non-porous support. The porous structure is formed by spherical holes, which are interconnected and arranged in about 40 layers. The size of the holes of around 500 nm is somewhat larger than the size of the silica particles (d = 415 nm) used as template, while the windows interconnecting the holes have diameters of around 250-

300 *nm*. Within the porous zone, the holes are distributed evenly and rather regularly. A closer look reveals that the zone displays an inverse microstructure similar to the one of the fcc silica opal template. Accordingly, not only the shape and size, but also the characteristic hexagonal structure of the silica particles in the colloidal crystal were basically conserved, as highlighted by the red marks in the micrographs (Figures 5.3c and 5.3d). Still, the IOH structure seen in the micrographs contains irregularities and defects, including, *e.g.*, a long fissure as shown in Figures 5.3b and 5.3d. In particular, large defects are visible at the border of the porous and the continuous zones, as illustrated at the bottom of Figures 5.3b and 5.3d. Possibly, the defects observed are damages suffered during sample preparation for taking the micrographs. Alternatively, the defects may be due to stress encountered in the course of the fabrication of the IOH, *e.g.*, during demolding, during etching of the template nanoparticles, due to contraction of the monomer mixture during the polymerization, or due to temporarily inhomogeneous swelling during, for instance, the various washing steps. In any case, even if we cannot decide whether the defects are inherent to the IOH fabrication, or are the result of secondary damaging, the internal structure of the IOH samples prepared is regular and good enough to display structural color and iridescence.

Moreover, these holes are connected to each other with windows of around 250-300 *nm*. Actually, these windows depict the effective limiting size for diffusion. Therefore, in order to enable a volume change, upon a stimulus (*e.g.* presence of an analyte), it is preferable to have stimuli that can homogenously penetrate the network and produce a volume effect instead of a superficial one. Consequently, too large molecules (> 300 *nm*) are not expected to induce a volume effect, and so a priori should not change the opal's color. In contrast, the smaller molecules (< 300 *nm*) that can diffuse into the gel, a volume effect may be expected if the resulting change of hydrophilicity is strong enough, and therefore may modulate the Bragg peak position.

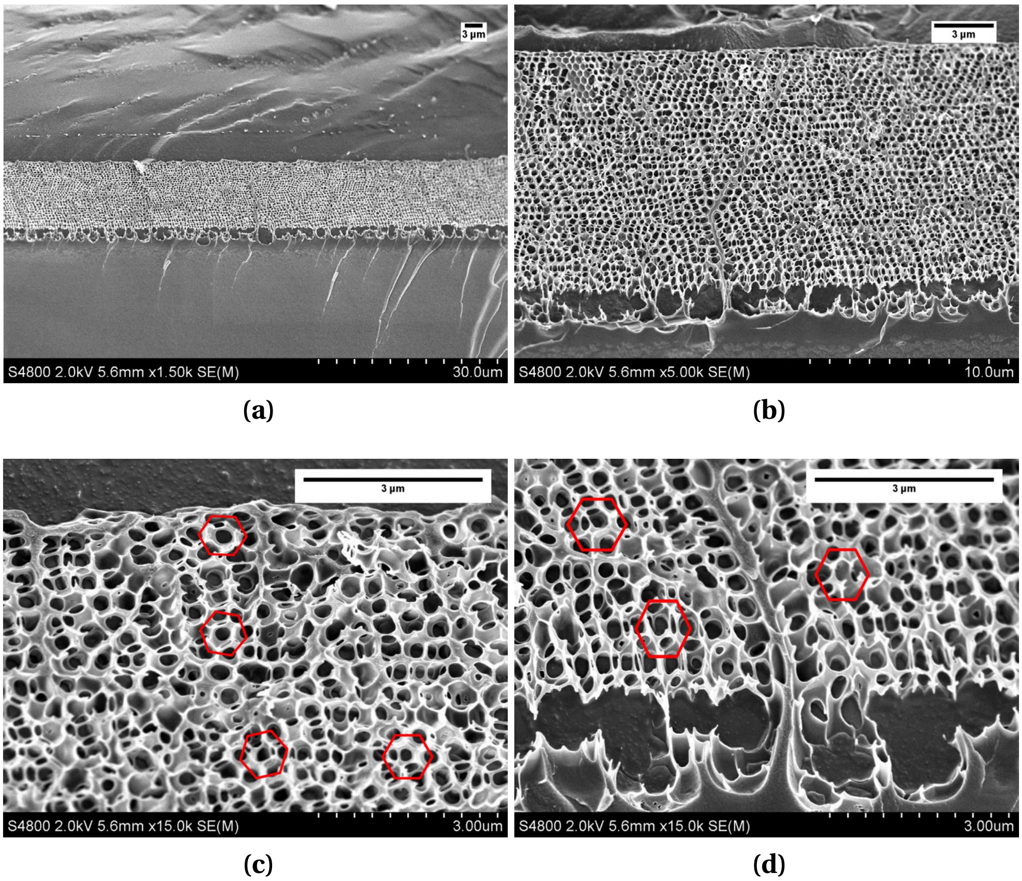
3 µm
S4800 2.0kV 5.6mm x1.50k SE(M)
30.0um
3 µm
S4800 2.0kV 5.6mm x5.00k SE(M)
10.0um
(a)
(b)
3 µm
S4800 2.0kV 5.6mm x15.0k SE(M)
3.00um
3 µm
S4800 2.0kV 5.6mm x15.0k SE(M)
3.00um
(c)
(d)

Figure 5.3: SEM micrographs of a cut through functionalized inverse opal hydrogel **IOH-boroxol**: (a) overview; (b) side view ; (c) detail of the IOH zone, the red hexagons highlighting the basic opal structure; (d) detail as for (c), highlighting the IOH zone near the interface to the bulk hydrogel.

5.4 UV-vis Spectroscopy Analysis

In order to evaluate the ability of the synthesized IOHs to reflect certain wavelengths, the PhCs were analyzed with a UV-vis transmission spectrometer, identically to the measurement presented in Chapter 3 for the characterization of silica opals. In contrary to the silica opal measurements, the IOHs need to stay immersed in water all time. The surrounded water guarantees the possible diffusion of analytes but also the equilibrium between a swollen and a shrunk gel, which is primordial for the recognition process. Therefore, IOH measurements were conducted using a specific demountable quartz cuvette with a light path of 0.5 μm, which kept the hydrogel film, which was fixed perpendicularly to the light beam, constantly immersed in solution.

This setup was primordial to investigate the swelling/shrinking behavior, following the Bragg diffraction peak with temperature, since the angle between the diffraction planes and the incident light also modulates the reflected light (see Chapter 3).

5.4.1 non-Functionalized IOH

Once the homogenous structure of the IOHs was elucidated, the question of the interference color and the IOHs' abilities to prevent the propagation of selective wavelengths still needed to be solved. Therefore, transmission spectra were analyzed in order to study the photonic band as done for the silica opals. Since the polymers used were thermosensitive, the photonic band (also called Bragg peak) could shift upon temperature change. Figure 5.4a illustrates this "*color shift*" for **IOH-0**. At 10 °C, the Bragg peak is in the near-IR region (859 *nm*), whereas at 80 °C, the local maximum of absorbance is shifted by about 200 *nm*, leading to a reddish appearance. The plot of the maximum *vs.* temperature (Figure 5.4b) illustrates the spectral window of the transition. Similar curve shapes were obtained with SRs of non-structured hydrogels (**H-0**). Indeed, OEG moieties provoke the enlargement of the volume transition (Chapter 4), which underlines the link between the volume and the color change. This evolution follows a polynomial function, which is characterized by an inflection point around 45 °C that may be assimilated to the transition temperature, since a notable volume change is actually taking place all long from 10 °C to 80 °C.

The color modulation upon temperature changes is due to the swelling/shrinking of the hydrogel. The color shift can be analyzed by the Bragg law, see Chapter 3. The schematic representation of hydrogels (Figure 5.4c) illustrates the swelling behavior when the temperature decreases, as well as the shrinking upon heating. The induced volume change modulates the interplanar distance (a_{hkl}), which modifies the reflected wavelengths when the other parameters (refractive index, n_{avg}, and the angle between the incident light and the diffraction plane, θ) are kept constant. When the IOH shrinks, d decreases ($a^1_{hkl} > a^2_{hkl}$), shifting the Bragg peak to the smaller wavelengths. Since this effect brings the reflected color closer to the blue color range (≈ 400 *nm*), this shift is often called "*blue-shift*". Analogously, the IOH swells when cooled, increasing the distance d and shifting the Bragg peak to higher wavelengths. In this "*red-shift*", the Bragg peak moves toward the red color range of the visible spectrum.

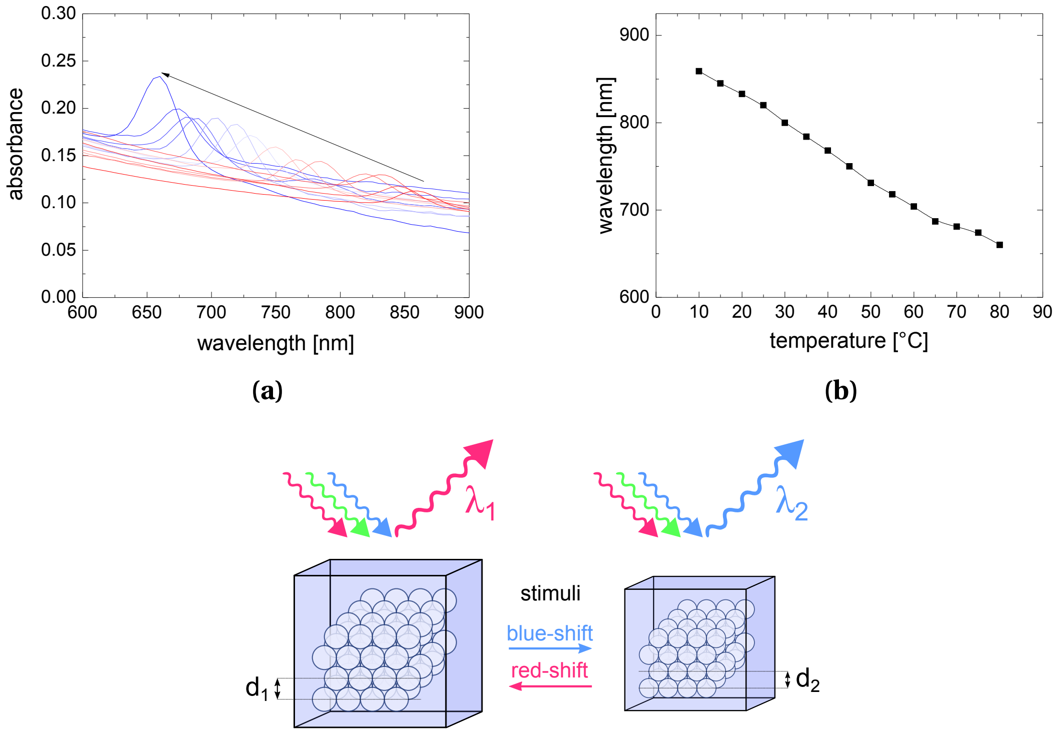

(a) **(b)**

(c)

Figure 5.4: Temperature dependent evolution of the structural color of the non-functionalized sample **IOH-0** (a) and (c)) from 10 to 80 °C in PBS (pH 7.4). Graph (a) shows the evolution of the absorbance spectra, graph (b) the derived Bragg peak's positions; (c) Schematic illustration of a responsive IOH, which exhibits a color change upon exposure to a stimulus.

Figure 5.5, illustrates this visual effect for a piece of an IOH (**IOH-boroxol**) at different temperatures. Figure 5.5a shows a reddish IOH at 40 °C, whereas upon an increase of 5-10 °C, the color of the IOH is shifted to yellow-orange (Figures 5.5b and 5.5c).

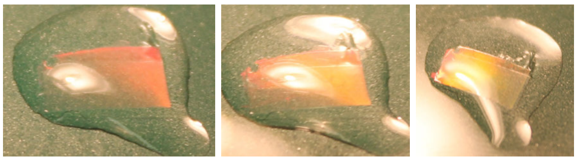

(a) **(b)** **(c)**

Figure 5.5: Photograph of a piece of **IOH-boroxol** swollen (size approx. 5 *mm* × 10 *mm*) immersed in water, illuminated by white light from the bottom-left side: (a) at 40 °C; (b) at 45 °C; (c) at 50 °C.

Simultaneously to the blue-shift, the absolute Bragg peak intensity was found to increase upon heating. This effect can be explained by the change of the hydrogel refractive index. At low temperature (20 °C) the IOH contains 53% of water, whereas at higher temperatures (80 °C) the water content decreases to 17%. Therefore the refractive index of the overall hydrogel is modulated between two limits: the refractive index of water ($n_{H_2O} = 1.33$) and the refractive index of the dry polymer (such as polymethacrylates $n_{\text{polymer}} \approx 1.49$), depending of content of water (φ_{H_2O}), as described below. Therefore the refractive index contrast, which determines the intensity of the Bragg peak, increases with the temperature, and the increasing dehydration of the gel.

$$\Delta n = \left| n_{\text{hydrogel}} - n_{H_2O} \right| \tag{5.1}$$

$$\Rightarrow \quad \Delta n = \left| n_{\text{polymer}} - n_{H_2O} \right| \cdot \left(1 - \varphi_{H_2O}\right) \tag{5.2}$$

$$= (1.49 - 1.33) \cdot \left(1 - \varphi_{H_2O}\right) = 0.16 \cdot \left(1 - \varphi_{H_2O}\right)$$

The evolution of the Bragg peak positions as a function of the temperature was also conducted in different organic solvents (Figure 5.6a), in order to verify the link between the swelling properties of the OEG-hydrogel, and the Bragg peak shifts.

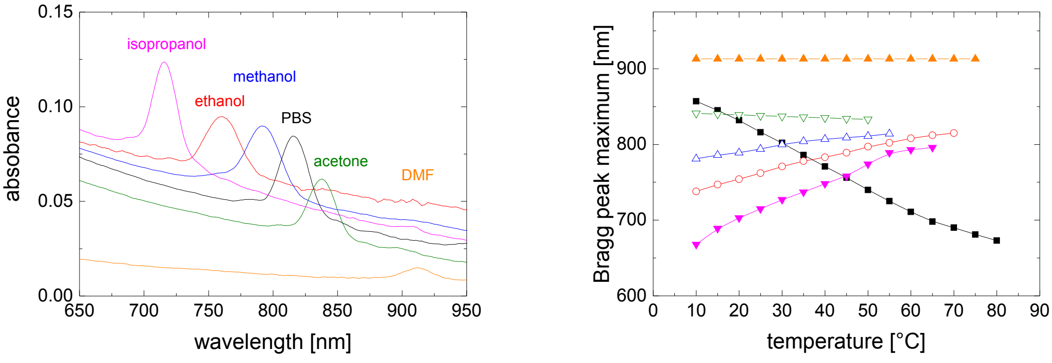

(a) **(b)**

Figure 5.6: Responsive behavior of inverse opal hydrogel **IOH-0** to selected organic solvents; (a) absorbance spectra of at 25 °C: isopropanol (——), ethanol (——), methanol (——), acetone (——), DMF (——) and PBS (pH = 7.4) as reference (——); (b) position of the Bragg peak maximum of in dependence on the temperature:isopropanol (▼), ethanol (○), methanol (△), acetone (▽), DMF (▲) and PBS (pH = 7.4) as reference (■).

Figure 5.6a illustrates that the IOH swells in different organic solvents at 25 °C, shifting its Bragg peak. The position of the Bragg peak seems to express the "*quality*" of the solvent. The solvents can be classified *via* their abilities to swell the IOH: isopropanol < ethanol < methanol < acetone < DMF.

Moreover, the various SRs as well as refractive indexes of the solvents were found to modulate the Bragg peak intensity (at 25 °C). The same trend is found as discussed above *i.e.*, the higher the refractive indexes contrast is, the higher is the Bragg peak intensity, see Table B.1. Indeed, the intensity in DMF is rather low (*Abs.* ≈ 0.006), the intensities in water and methanol are comparable (*Abs.* ≈ 0.04), as it is between ethanol and acetone (*Abs.* ≈ 0.03). Only the intensity in isopropanol is higher than expected (*Abs.* ≈ 0.05), presumably due to lower solvation of the polymer chains.

These measurements were repeated at different temperatures (Figure 5.6b). The evolution of the Bragg peak position as function of temperature in the organic solvents is opposed to the evolution in water. Upon heating a blue-shift is observed in water, whereas in organic solvents a red-shift is seen. The OEG chains encounter a decrease of the solubility when the temperature increases (LCST-type) whereas the solubility of the OEG chains in most of the organic solvents increases with increasing temperature (UCST-type). Exceptions are DMF, where the Bragg peak shift seems independent, and the acetone that shows a slight decrease of the Bragg peak position.

The "*quality*" of the organic solvent could also explain the evolution of the Bragg peak *vs.* temperature plots in organic solvents (Figure 5.6b). Nevertheless, no obvious correlations where found by comparing the Hansen solubility parameters of solvents and of molecules with similar structures as OEGMA-hydrogel (see Appendix B).

5.4.2 Functionalized IOH

Benzoboroxole – 1,2-Diols

Benzoboroxole moities incorporated in thermoresponsive polymers show a high affinitiy to 1,2-diols (Section 4.6.1), which can in some case induce a coil-to-globule transition (see Section 4.7.1). In this section, analyte binding with **IOH-boroxol** will be studied in regard to a shift of the Bragg peak position. Similar to the shift of CP in the case of linear copolymers, an increase of the overall hydrophilicity increases the

Bragg peak wavelength (red-shift), whereas a decrease of the hydrophilicity reduces the Bragg peak wavelength (blue-shift).

Initially, the shift of the Bragg peak position upon pH change was tested. As the pK_a value of the boronic acid controls the transformation between the hydrophobic sp^2 and hydrophilic sp^3 hybridized forms (see Figure 4.8e), **IOH-boroxol** should also be pH-responsive. Moreover, this pH-transition should take place at the pK_a of **boroxol-MAm**, which were designed to be close to physiological pH values.[143–146]

Bragg peak positions of the **IOH-boroxol** swollen in aqueous solution at different pH values were measured as done in the previous study in Section 5.4.1 at different temperatures (Figure 5.7). The IOH at pH = 7.4 shows a blue-shift of wavelength to 300 *nm* in the temperature window from 10 to 80 °C (Figure 5.7a). Additionally, the IOH exhibits also a Bragg peak shift *via* pH change, being inherently dual-responsive. Therefore, a red-shift is produced when the pH and so the amount of hydrophilic sp^3 benzoboroxole forms increase. The Bragg peak shift upon pH change is less pronounced than upon temperature change. Interestingly (at 25 °C), the strongest observed shift, about 40 *nm*, is between pH 6.8 to 7.4, where the pK_a of **boroxol-MAm** is expected.[147–149, 189–191]

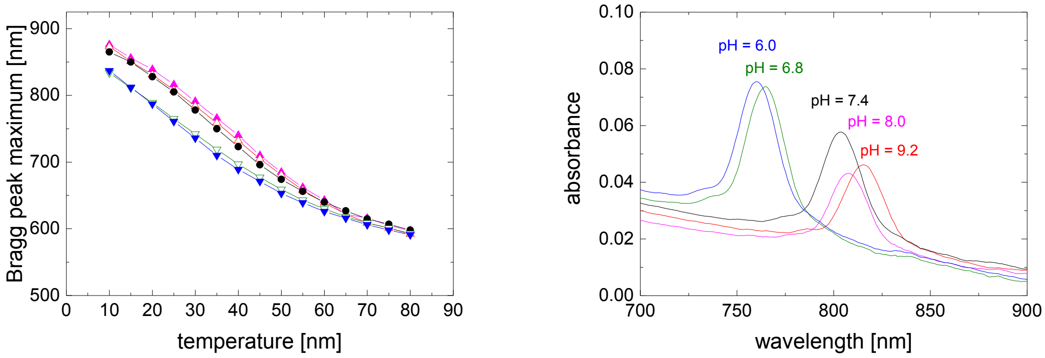

(a) (b)

Figure 5.7: Thermo-responsive and pH-responsive behavior of inverse opal hydrogel **IOH-boroxol** in water; (a) position of the Bragg peak maximum of in dependence on the temperature and pH: pH = 6.0 (▼), pH = 6.8 (▽), pH = 7.4 (●), pH = 8.0 (△), pH = 9.2 (▲); (b) absorbance spectra of at 25 °C modulated by the pH: pH = 6.0 (——), pH = 6.8 (——), pH = 7.4 (——), pH = 8.0 (——), pH = 9.2 (——).

Moreover, between 10 to 40 °C, the Bragg peaks are uniformly shifted to the lowest wavelengths by heating, but above 50 °C the profile approaches a plateau, identical for all pH values. This may be explained that at high temperatures, the hydrogel becomes too shrunk to display still a volume transition upon pH changes. Additionally, it is noted that the Bragg peak intensity decreases under basic conditions (Figure 5.7b). This observation can be explained as in Section 5.4.1: the increase of the charged groups increases the hydrophilicity of the hydrogel, which then absorbs more water. This reduces its refractive index contrast to the aqueous solution (Equation (5.2)).

Not only the binding of HO^- can change the IOH's hydrophilicity, thus shifting the Bragg peak position, a similar effect is observable also with bigger analytes, such as various 1,2-diols: catechols, catecholamines as dopamine, adrenaline, or L-DOPA, or even glycopolymers as PXMs.

The analyte-responsive behavior of the IOHs was investigated in PBS, fixing the pH of the system to the physiological value of 7.4. For screening and distinguishing the effects of the various diol analytes, a fixed analyte concentration of 50 $mmol \cdot L^{-1}$ was chosen (Figure 5.8). First, the effect of the addition of catechols on the swelling and structural color of **IOH-boroxol** was studied, as these diols showed the biggest effects on the cloud point of the soluble copolymer analogue **P-boroxol** (see Table 4.2). Figures 5.8a and 5.8b show clearly, that the various catechols bind to the IOH and induce strong shifts of the Bragg peak positions, thus effectively modulating the IOH's color. A closer comparison of the effects of the catechols reveals that the relative shifts observed can be roughly correlated with their relative hydrophilicities: whereas hydrophobic substituents result in a shrinking of **IOH-boroxol**, hydrophilic substituents on the catechol result in a swelling.

While the addition of the hydrophobic 3,5-di-*tert*-butyl catechol blue-shifts the Bragg peak maximum of **IOH-boroxol** by more than 100 *nm* (at 25 °C), the addition of the hydrophilic Alizarin S or catechol-3,5-disulfonic acid red-shifts the Bragg peak maximum by about 50 *nm* (at 25 °C). Also, the additions of the natural catechols adrenaline and dopamine induce notable red-shifts, in the order of 20 - 25 *nm* (at 25 °C), while L-DOPA provokes a red-shift of more than 80 *nm* (at 25 °C). Interestingly, the sequence of the induced color shifts of the IOH by the individual catechols matches closely the sequence observed for the cloud point shifts of the soluble analogue **P-boroxol** (see Table 4.2), but is not completely identical. This finding underlines

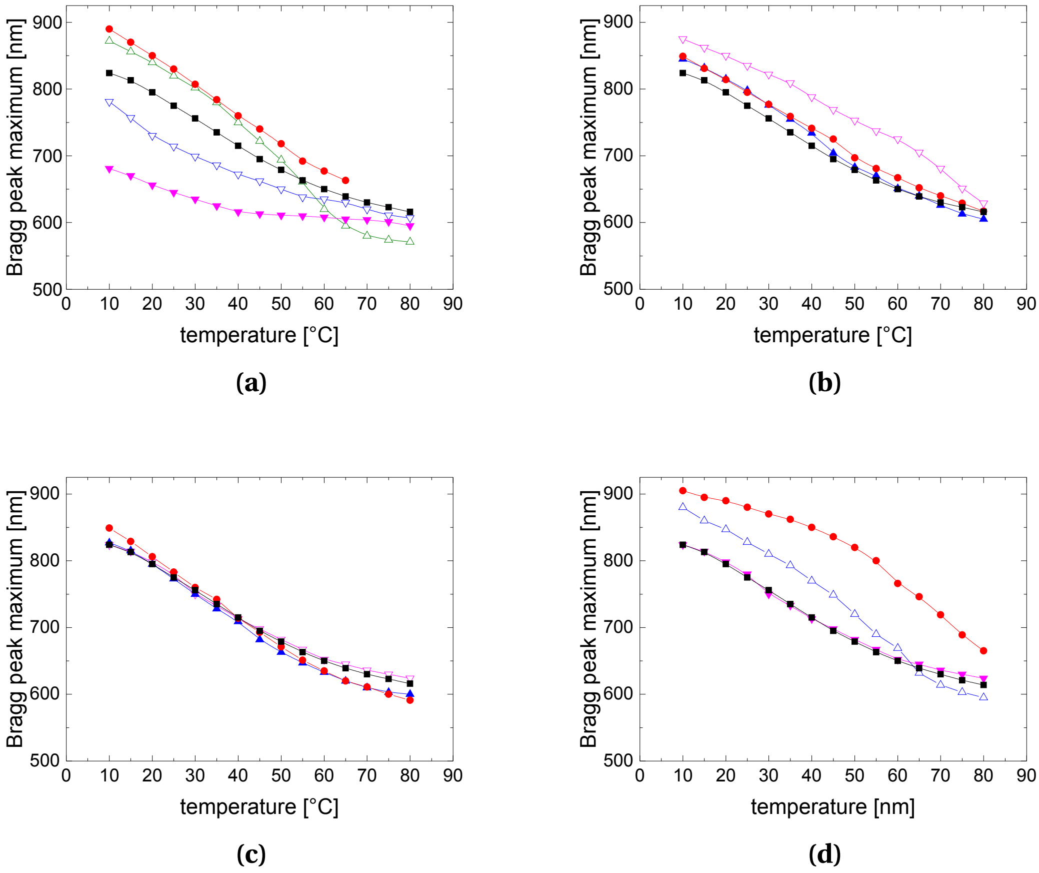

(a)

(b)

(c)

(d)

Figure 5.8: Evolution of the position of the Bragg peak maximum with temperature for the functionalized inverse opal hydrogel **IOH-boroxol** in PBS at pH = 7.4 in the absence (■) and in the presence (50 $mmol\cdot L^{-1}$) of diol analytes: (a) synthetic catechols: Alizatin S (●), catechol-3,5-disulfonic acid (△), pyrocatechol (▽), 3,5-di-*tert*-butyl-catechol (▼); (b) catecholamines: L-DOPA (▽), adrenaline (▲), dopamine (●); (c) saccharides and references: fructose (●), PMA (▲), PVA (▽); (d) glycopolymers: PXM-1 (●), PXM-2 (△), PXM-3 (▼).

the often neglected fact, that the evolution of the phase transition temperature of a polymer and of its absolute water content at a particular temperature above the phase transition, are – though being somehow related – two different phenomena, and therefore do not necessarily coincide. For instance, the rather small red-shifts induced by the binding of the protonated and thus cationic chatecols adrenaline and dopamine may originate in the ampholytic character of these adducts at pH 7.4, counteracting the swelling process. Also, the particularly strong red-shift of the Bragg peak maximum induced by the binding of catechol-3,5-disulfonic acid seen at temperatures well above

60 °C (see Figure 5.8a) may possibly originate in secondary attractive interactions, here of the two sulfonate moieties with the boroxole groups,[177] creating additional crosslinked sites that densify the collapsed hydrogel even further.

Having established strong effects of the low molar mass catechols on the IOH's swelling and structural color, the effects of saccharides, which are particularly attractive target analytes for biomedical sensors, were also investigated (Figure 5.8c). Interestingly, even the addition of fructose, which is known to be a monosaccharide that binds strongly to boronic acids, provokes only a rather small effect, with an induced red-shift of about 7 *nm* of the Bragg peak maximum at 25 °C. The other saccharides listed in Table 4.2, including the polymeric ones, had even smaller effects on the swelling. In contrast, glycopolymer PXM-1 that bears a xylitol derived polyol motif, affected the swelling of **IOH-boroxol** strongly, inducing, *e.g.*, a red-color shift at 35 °C of about 130 *nm* (Figure 5.8d). When reducing the concentration of PXM-1 to 1 $mmol{\cdot}L^{-1}$ (based on the repeat unit), the Bragg peak maximum still shifts by nearly 40 *nm*. Accordingly, such a strong binding effect in combination with the broad phase transition of the OEGMA-based hydrogels enables also quantitative measurements over a wide concentration range of the analyte, after calibrating the concentration dependent shifts of the Bragg peak maximum (Figure 5.9a). In analogy to the effects observed during the modulated cloud point measurements of the soluble copolymer analogue **P-boroxol**, the analyte induced color shifts become less pronounced when the hydrophilicty of the polymer analyte decreases. Though containing the identical glycomonomer, *i.e.*, the identical boroxole binding motif, the shifts of the Bragg peak maxima decrease rapidly with the hydrophobicity of the maleimide repeat unit in the glycocopolymer series PXM. Whereas at, *e.g.*, 25 °C, PXM-1 and PXM-2 induce red-shifts of the Bragg peak of **IOH-boroxol** by 105 *nm* and 53 *nm*, respectively, the addition of PXM-3 leaves the position of the Bragg peak virtually unaffected (Figure 5.8d).

Importantly, the control experiments showed that the interaction of potential analytes with the non-functionalized **IOH-0** do not induce notable changes of the IOH at a fixed temperature and pH value, even when adding the analytes showing the biggest effects on **IOH-boroxol**, such as low molar mass Alizarin S or high molar mass PXM-1 (Figure 5.9b). Also, it was shown that the effects induced by the addition of the diols are reversible. After washing **IOH-boroxol** with a solution containing low molar mass boroxole, the induced color shift is reversed, and the original temperature dependent shift of the Bragg peak is regained over the full temperature range (Figure 5.9c). All these results demonstrate that strong and selective effects occur for the binding of specific diols/polyols to boroxole-functionalized **IOH-boroxol**, establishing such functional IOHs as attractive platforms for facile and effective sensing of low as well as high molar mass analytes.

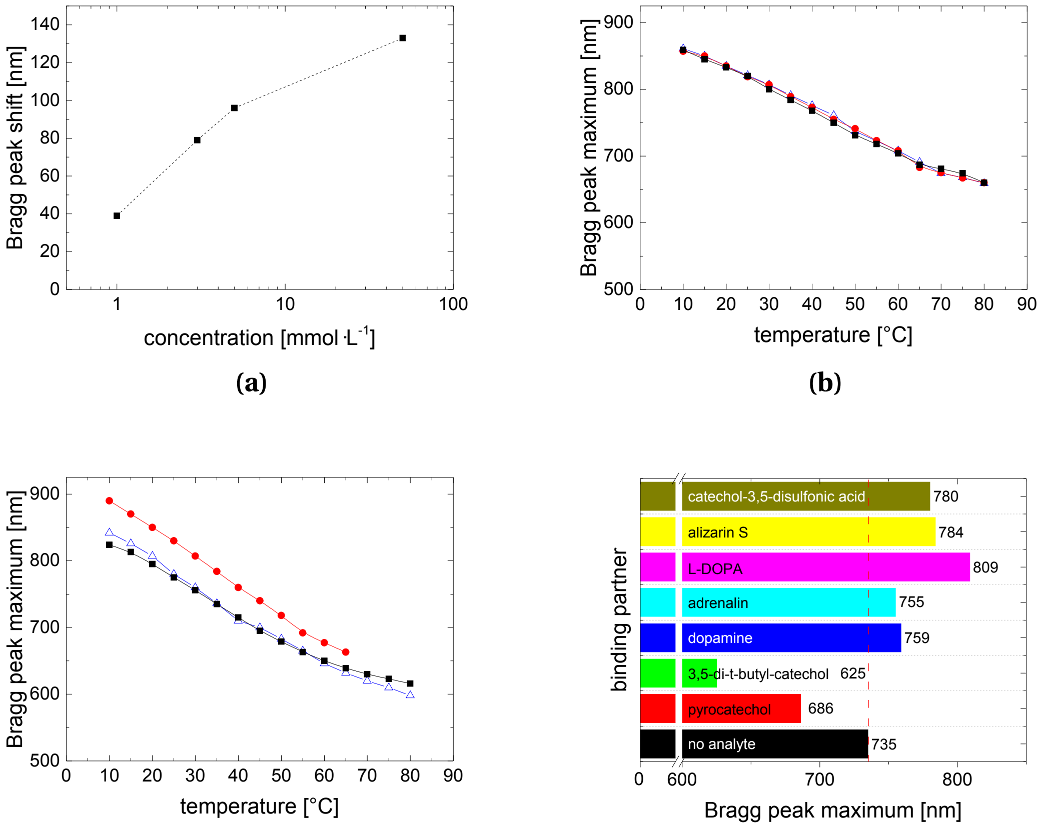

(a) (b)

(c) (d)

Figure 5.9: Evolution of the position of the Bragg peak maximum of (a,c,d) functionalized **IOH-boroxol** and (b) non-functionalized inverse opal hydrogel **IOH-0** in PBS at pH = 7.4; (a) with increasing concentrations of glycopolymer PXM-1 (content of repeat units) at 37 °C; (b) in absence (■) and in presence (50 $mmol{\cdot}L^{-1}$) of analyte Alizarin S (●), or PXM-1 (△); (c) before (■) and after adding Alizarin S (●), and after subsequent washing a with solution containing free benzoboroxole(△); (d) induced by the addition of selected analytes at 35 °C.

Small molecules penetrate in the structured part of the hydrogel and provoke a volume change after binding. Moreover, a small molecule can also diffuse in the overall hydrogel, even in the non-structured part. According to the equation Equation (5.3) described by Peppas *et al.* for poly-(2-hydroxyethyl methacrylate) [192, 193] with a content of 19 *mol.*-% of crosslinker, and a swelling ratio (SR) of 2.0, the mesh size (ξ) is estimated to be around 1.2 *nm*.

$$\xi = d_{C-C} \cdot \frac{1}{\sqrt{\chi}} \cdot \sqrt{C_n} \cdot \sqrt[3]{\mathrm{SR}} \tag{5.3}$$

With d as the length of C-C bond (d_{C-C} = 1.54 Ångström), C_n as a characteristic ratio for polymethacrylates (C_n = 6.9), and χ as the content of effective crosslinker. For the calculation all the crosslinker molecules (19 *mol.*-%) were considered to bridge between two polymer chains, excluding in that way loop formation. This equation describes the mesh size of ideal networks, where the crosslinker is supposed to be homogenously distributed in the polymer chain. Therefore, small molecules (< 1.2 *nm*) can a priori diffuse in the overall hydrogel, whereas bigger molecules (> 1.2 *nm*) can only penetrate the structured part, where the pores are bigger than 400 *nm*.

The next section discuss whether larger analytes such as proteins can show a similar color selective color shift, despite their size, which should restrict their diffusion in the hydrogel.

Biotin – Avdin

While the glycopolymers of the PXM copolymer series are rather large, and share many structural similarities to polysaccharides, they are poor models for another key class of biomolecules crucial for biological interactions, namely the proteins. Thus, it was interesting to explore also a model system able to mimic protein based biological interactions. For this purpose, classical model systems based on biotin – avidin interaction are used, even if the extremely high binding constant (dissociation) is not representative for most biological systems (pK_d = 15).

The incorporation of the rather large proteins into the hydrogel is challenging. Note that the size of an avidin tetramer is around 5.6 × 5.0 × 4.0 nm^3.[194] Therefore, the protein is a priori too large to diffuse in the non-structured part of the IOH, which should restrict the hydrophilicity change of the IOH to the structured part. In order to estimate this size effect, the IOHs were incubated with avidin that is conjugated with fluorescein. This fluorescent label enables after washing to indentify *via* laser scanning microscopy (LSM), in which part of the IOH the proteins have been bound. Figure 5.10 shows 4 micrographs, on the top-left a top view of **IOH-biotin** where avidin-fluorescein remains after washing, due to the coordination between avidin and biotin groups embedded in the IOH. The micrograph below (bottom-left) illustrates the same **IOH-biotin** as in the left, but in a perpendicular view. On the top-right, the same experiment was carried out but this time using hydrogel devoid of biotin, **IOH-0**. In order to evaluate the influence of the structured part, **H-biotin** was also tested (bottom-right).

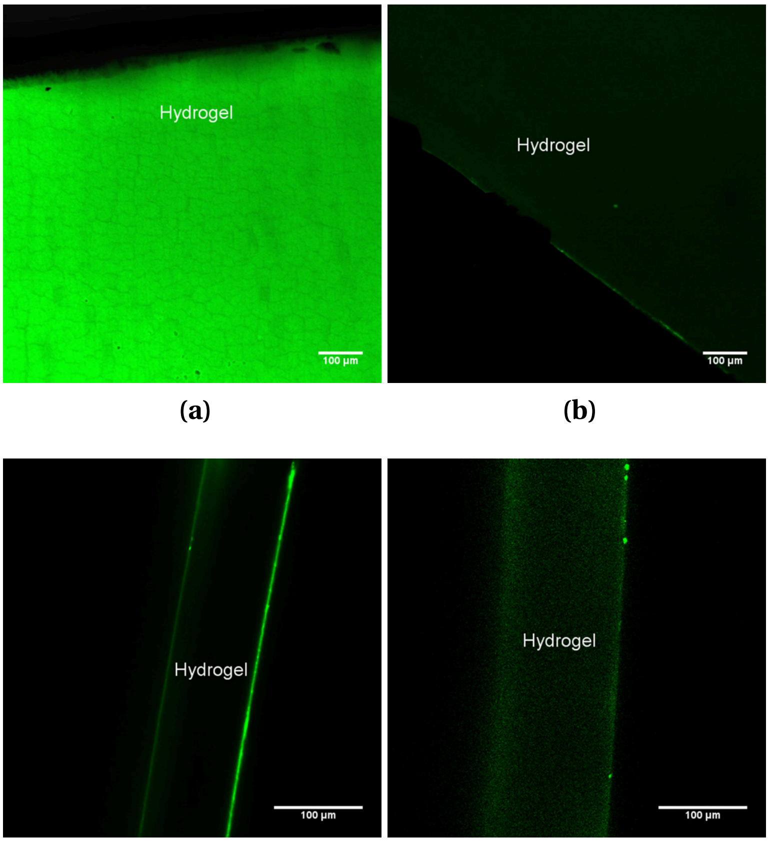

(a) **(b)**

(c) **(d)**

Figure 5.10: Fluorescent micrographs of structured inverse opal hydrogel and non-structured hydrogel after incubation with avidin-fluorescein and subsequent washing; top view of (a) **IOH-biotin** and (b) **IOH-0**; side view of (c) **IOH-biotin** and (d) **H-biotin**. The intensities of (b) and (d) were magnified *vs.* (a) and (c).

Figure 5.10a shows the presence of avidin on the **IOH-biotin** surface, even after washing the bound avidin remains present. In contrast, the IOH devoid of biotin (**IOH-0**) does not show comparable fluorescence intensity; most of the avidin is released by washing with PBS (Figure 5.10b). **IOH-biotin** was tilted by 90 °, and cut to show of the inside diffusion of the avidin. Figure 5.10c illustrates clearly an non-fluorescent area included into two thin fluorescent lines. These two fluorescent lines represent the border of the IOH. The line at the right shows a much higher intensity than the line at the left. This indicates that the right side is more concentrated in avidin. The thickness of the right fluorescent layer is about 7 μm, whereas the thickness of inverse opal structure measured by SEM was 12 μm. Therefore, the avidin diffuse better the right side of the **IOH-biotin**. This shows that this layer is presumably the structured part of the IOH. Importantly, a biotinylated non-structured hydrogel (**H-biotin**) was also tested (Figure 5.10d). This hydrogel shows not only a much weaker fluorescence intensity, which indicates a much lower amount of avidin bound, but also, the absence of a strongly intense fluorescent layer at the edge of the hydrogel.

Thus, it can be concluded from this experiment that the structured part of the IOH enables avidin to penetrate the film, while the rest of the hydrogel is virtually impermeable to avidin under the applied conditions.

The avidin-responsive behavior of **IOH-biotin** was investigated in PBS (pH = 7.4) *via* spectrometry (Figure 5.11a). Figure 5.11a illustrates the red-shift of the Bragg peak maximum, which is at least shifted by 36 *nm* at 10 °C, and maximally about *ca.* 134 *nm* at 45 °C. The shapes of the curves are similar to broad transitions observed with **IOH-boroxol** in Section 5.4.2. The Bragg peak shifts occur for this sample not from the visible electromagnetic range to another visible range, but from visible to infra-red. For instance at 25 °C, the Bragg peak maximum is at 746 *nm*, which leads to a red color that vanishes upon avidin addition, due to the red shift of the Bragg peak at 834 *nm* in the infra-red region. In agreement with the fluorescence experiment, the avidin is mostly washed out for an IOH devoid of biotin (**IOH-0**) , and so only 15 *nm* Bragg peak shift is observed 25 °C *vs.* 88 *nm* for a biotinylated IOH (**IOH-boroxol**). This selective effect demonstrates also nicely the low-fouling properties of the polymer matrix, which inhibits unspecific adsorption of proteins, so that the binding between biotin and avidin becomes selective (Figure 5.11b).

Concentration dependent swelling studies showed, that the interaction of avidin with **IOH-biotin** is strong enough to produce still a 25 *nm* red-shift at 76 $nmol{\cdot}L^{-1}$ analyte concentration (Figure 5.12a) under physiological conditions (pH = 7.4, T = 37 °C). When **IOH-biotin** after binding of avidin is washed with free biotin solution, the hydrophilic avidin is slowly released, which leads to a decrease of the hydrophilicity manifested by a blue-shift of the Bragg peak until a position close to the initial

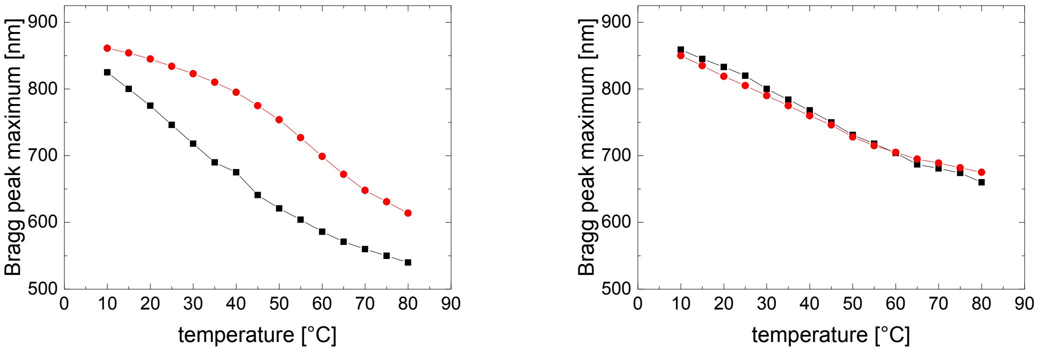

(a)

(b)

Figure 5.11: Evolution of the position of the Bragg peak maximum for (a) functionalized (**IOH-biotin**) and (b) non-functionalized (**IOH-0**) inverse opal hydrogels with temperature in PBS at pH = 7.4, in absence (■) and in presence (0.5 $g \cdot L^{-1}$) of avidin (●).

wavelength before the protein binding (Figure 5.12b). For instance at 25 °C, **IOH-biotin** exhibits originally a Bragg peak at 758 *nm*, whereas after avidin binding, its Bragg peak is red-shifted to 834 *nm*. After subsequent washing cycles with a solution containing free biotin, the Bragg peak is blue-shifted back to its initial position before the incubation with avidin (758 *nm*). These findings prove that the volume change is due to the binding of avidin, and moreover, that the swelling can be turned-off *via* competitive binding of avidin to biotin fixed in the hydrogel and free biotin in solution.

All the studies on thermoresponsive polymers presented so far were performed with IOHs that were made of MEO$_2$MA and OEGMA475. In order to highlight the importance of the thermoresponsive behavior of the IOHs to transduce the protein binding into a swelling signal, two additional IOH systems without thermoresponsive behavior were synthesized. While both IOH systems incorporate **biotin-MA** as receptor for avidin, and OEGDMA550 as crosslinker, the polymer matrix was varied: a more hydrophilic system made of OEGMA475 (**IOH-OEGMA-biotin**), and a less hydrophilic system based on HEMA (**IOH-HEMA-biotin**) were synthesized.

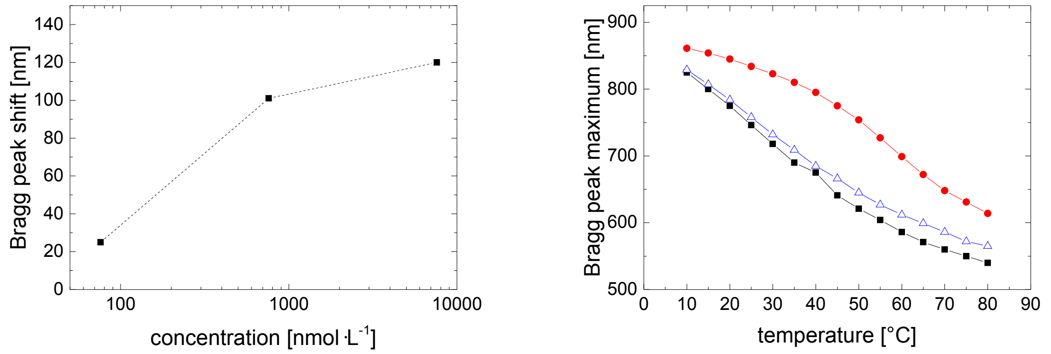

(a) **(b)**

Figure 5.12: Evolution of the position of the Bragg peak maximum of functional inverse opal hydrogel (**IOH-biotin**) in PBS at pH = 7.4; with (a) increasing concentrations of avidin at 37 °C; with (b) temperature, before (■) and after adding avidin (●), and after subsequent washing with solution containing free biotin (△).

The **IOH-OEGMA-biotin** system did not show any Bragg peak, due to the too strong hydrophilicity of the polymer matrix, which apparently leads to a too small refractive index contrast (Δn) between the polymer and water. In contrast, **IOH-HEMA-biotin** shows a Bragg peak around *ca.* 685 *nm* (at 35 °C). However, its Bragg peak blue-shifted only marginally by 2 *nm* upon avidin binding (*vs.* a 121 *nm* red-shift for **IOH-biotin**).

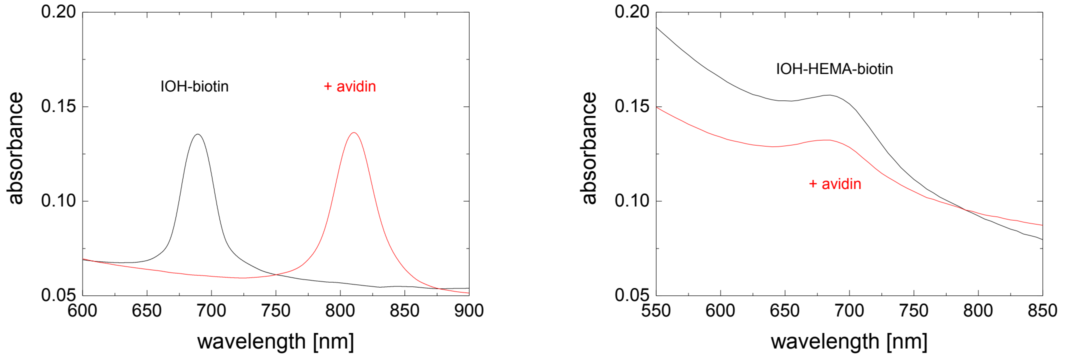

(a) **(b)**

Figure 5.13: Evolution of the Bragg peak wavelength at 35 °C for (a) thermoresponsive (**IOH-biotin**) and (b) non-thermoresponsive (**IOH-HEMA-biotin**) inverse opal hydrogels in PBS at pH = 7.4, in absence (——) and in presence (0.5 $g{\cdot}L^{-1}$) of avidin (——).

While the biotin moieties are essential to interact with avidin, the hydrogel must be able transduce the hydrophilic change into a swelling change. Therefore, thermoresponsive polymers are the key to build such hydrogel sensors, which change their properties upon a small change of environment. This interdependence implies a dual responsive IOH system (to analyte and to temperature), as the thermoresponsive behavior is crucial to achieve an effective isothermal analyte sensing.

IOH-biotin can strongly and selectively detect the presence of protein of avidin by a simple color shift, despite its size makes avidin already a challenging model system for obtaining huge Bragg peak shifts, up to 130 *nm*. This model system takes advantage of the strong binding constant between biotin and avidin, which is the highest known ligand interaction in biology. For this reason, IOH based on other model systems with lower and more classic binding constants, such as D-mannose and concanavalin A will be discussed in the next section.

D-Mannose – Concanavalin A

Similar to avidin, the protein concanavalin A is composed of tetramers, having an overall size of $4.2 \times 4.0 \times 3.9\ nm^3$. [162] Thus, ConA is expected to penetrate as well as avidin into the structured part of the IOH films (see Section 5.4.2). ConA is a quite hydrophilic protein, so the Bragg peak maximum of an IOH functionalized with mannose moieties (**IOH-mannose**) is expected to red-shift upon ConA binding.
Still for D-mannose – ConA, this effect should be less pronounced than for biotin – avidin, as the binding constant is much smaller than for biotin – avidin. Also, the hydrophilicity change between the bound mannose-ConA pair and the unbound mannose moiety should be weaker than for a bound biotin-avidin pair and free a biotin group, since the mannose group is soluble in water, while the biotin moiety is not.

Even if the silica template used was composed of the same silica particles as for the other IOHs ($d = 415\ nm$), the Bragg peaks of the final **IOH-mannose** were observed in the higher wavelength region. This is due to the post-treatment of the **IOH-mannose-Ac** precursor, which increases the hydrophilicity of the IOH by cleaving the acetyl protecting groups present in **mannose-A**.

Although ConA is a hydrophilic molecule, Figure 5.14a exhibited a surprising shrinking of the IOH upon ConA binding. It is assumed that this blue-shift of the Bragg peak is provoked by the tetravalency of ConA, which behaves as a crosslinker binding several mannose moieties. This behavior matches with the observations in Section 4.7.1, where ConA can induce a collapse of the soluble copolymer **P-mannose**.

For instance at 25 °C, the binding of ConA blue-shifts the Bragg peak of **IOH-mannose** by 51 *nm*. In contrast, the control IOH devoid of mannose (**IOH-0**) does not show a significant Bragg peak shift upon exposure to ConA (Figure 5.14b).

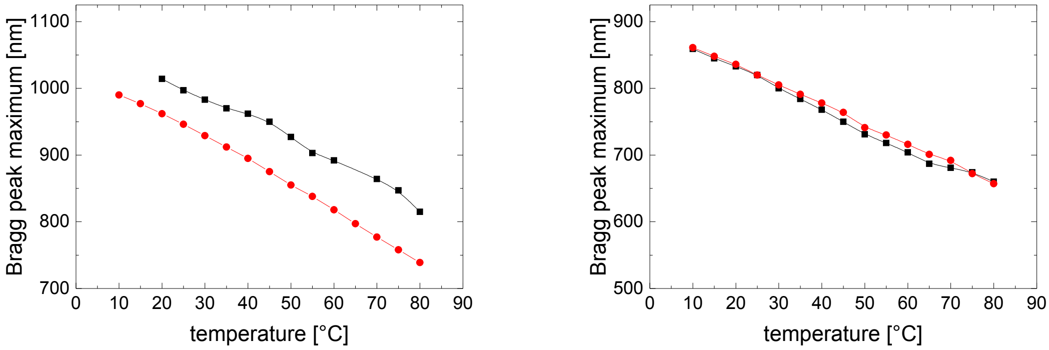

(a) **(b)**

Figure 5.14: Evolution of the position of the Bragg peak maximum for (a) functionalized (**IOH-mannose**) and (b) non-functionalized (**IOH-0**) inverse opal hydrogels with temperature in PBS at pH = 7.4, in absence (■) and in presence (0.5 $g{\cdot}L^{-1}$) of ConA (●).

This ability of ConA for binding multiple sugar groups was used, for instance by Miyata *et al.*, to crosslink glycopolymers.[173] They also observed that the SR of their hydrogels depended on the ConA concentration, but also on the presence of glucose molecules *via* competitive binding of ConA to sugar untits attached in the matrix and glucose in solution. Therefore, the presence of glucose decreases the crosslinking density, which leads to an increase of the SRs. This competitive essay was repeated with **IOH-mannose**, instead of glycopolymers. **IOH-mannose** previously shrunk *via* ConA binding was swollen *via* exposure to free mannose (see Figure 5.15b). This leads to a red-shift of the Bragg peak maximum of the **IOH-mannose**. For instance at 25 °C, the Bragg peak is shifted back of 34 *nm*, which signifies that the ConA are still present in the matrix.

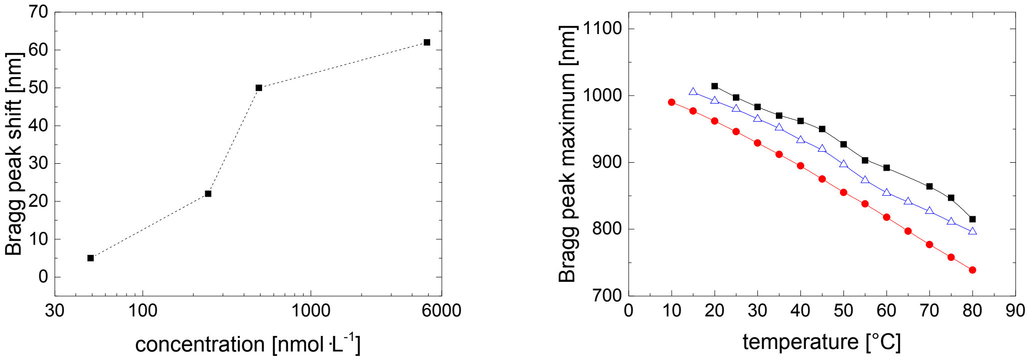

(a)

(b)

Figure 5.15: Evolution of the position of the Bragg peak maximum of functional inverse opal hydrogel (**IOH-mannose**) in PBS at pH = 7.4 ; with (a) increasing concentrations of ConA at 37 °C; with (b) temperature, before (■) and after adding avidin (●), and after subsequent washing with solution containing free mannose (△).

IOH-mannose exhibits a slightly lower sensitivity compared to **IOH-biotin**. Thus at 37 °C with a concentration of 49 $nmol \cdot L^{-1}$ only a Bragg peak shift of 5 nm was observed. Nevertheless, for higher concentration (> 490 $nmol \cdot L^{-1}$) the finding that such a large protein with a rather low binding constant can affect and modify the structure in a way to reduce or increase the wavelength of interference light by up to 50 nm, is already surprising.

6 Further Systems

6.1 Anti-Bodies Immobilization on Hydrogel Surfaces

In order to investigate specific interactions between hydrogels and analytes larger than proteins, bacteria analytes observable *via* optical microscopy were chosen (> 1 μm). Similarly to the systems discussed in Section 5.4.2, the hydrogel must specifically interact with the analyte to enable a specific detection. The model systems chosen were *Escherichia coli* (**E. coli**) (wild type, size ≈ 2 μm) and a specific anti-body for their pili (K99) **AB E. coli**, and *Salmonela thyphimurium* (attenuated, size ≈ 2-5 μm) (**S. thyp**) and the specific anti-body **AB S. thyp**. *Pseudomonas putida* (wild type, size ≈ 2-5 μm) was used as control analyte.

In contrast the systems presented in Section 5.4.2, which contain recognition units incorporated during the polymerization, the recognition unit (here: **AB E. coli**) is immobilized in a post-polymerization step on the hydrogel surface *via* peptid coupling. This strategy enables versatile anti-body immobilizations. First, hydrogels that incorporate protected carboxylic groups were synthesized (**H-COO*t*Bu**). To this purpose, a methacrylate monomer kindly provided by Dr. M. Päch (Fraunhofer IAP), which contains a OEG-spacer separated carboxylic group protected with *tert*-butyl alcohol, as used. After radical copolymerisation with MEO_2MA and OEGMA475, the carboxylate moieties in the functional monomer were liberated with trifluoroacetic acid, leading to hydrogels, which have free carboxylic acid groups (**H-COOH**), see Figure 6.1.

Secondly, **AB E. coli**, which contains primary amines, was immobilized on the hydrogel under mild conditions. The coupling used 1-ethyl-3-(3-dimethylaminopropyl) carbodiimide (EDC) / N-hydroxysuccinimide (NHS) in water (pH = 7.4), in order to preserve the structure of the anti-body, and to maintain its activity.

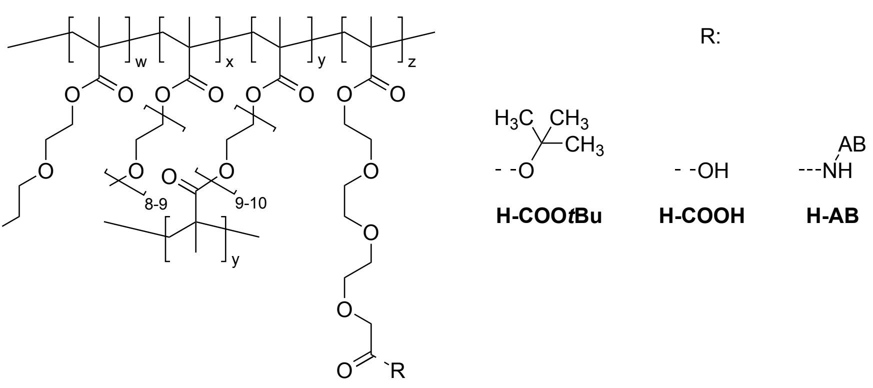

Figure 6.1: Scheme of the quaternary functional copolymer hydrogels: protected **H-COO*t*Bu**, deprotected **H-COOH**, anti-body-functionalized **H-AB**.

These studies were conducted in collaboration with Dr. R. Niedl (Biological Physics Dept., University of Potsdam), who provided the cell cultures and the anti-bodies.[195]

For a first test, non-structured hydrogels were prepared (see, Section 4.8.1 and Chapter 8) to establish the success not only of the immobilization but also of the bacteria binding. After the functionalization of the hydrogels with **AB E. coli** and **AB S. thyp**, the hydrogels were incubated 1 *h* in bacteria solutions (**E. coli**, **S. thyp**, **P. putida**) ($\approx 10^5$ $cell \cdot mL^{-1}$). The hydrogels was washed with stirring in water to remove the non-attached bacteria. The surface of the hydrogels were then analyzed *via* optical microscopy (see Figure 6.2)

Figure 6.2 shows that after the incubation and washing, the anti-body-functionalized hydrogels (**H-AB E. coli** and **H-AB S. thyp.**) contain on their surface a high density of bacteria, in contrast to non-functionalized hydrogels (**H-COOH**). Moreover, the density of bacteria is particularly high when the anti-body correspond to its incubated partner bacteria, such as **AB E. coli-E. coli** or **AB S. thyp-S. thyp**, and the anti-body-functionalized hydrogels discriminate with a high selectivity the non-partner bacteria. The selective binding is attributed to the low-fouling properties of the hydrogel matrix on the one hand, and to the high selectivity of the immobilized anti-bodies on the other hand.

Note that the bacteria present on the micrographs are fixed to the hydrogel surface, but still can slightly wiggle. This indicates that the attached bacteria are alive, but despite of their movements they can not be released. Moreover, it could be shown that the thermoresponsive nature of the polymer matrix (**H-AB E. coli**) was maintained,

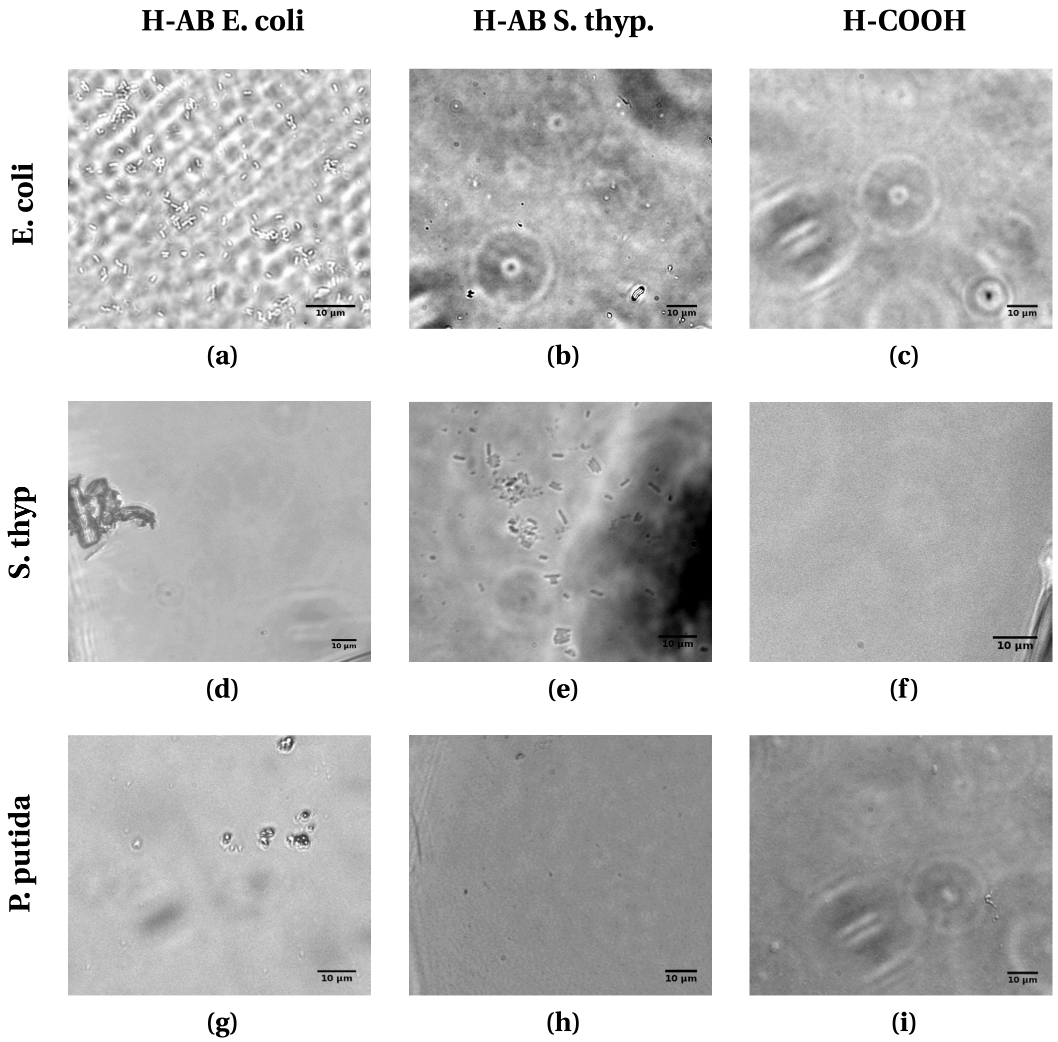

(a) (b) (c)

(d) (e) (f)

(g) (h) (i)

Figure 6.2: Micrographs of anti-body-functionalized (**H-AB E. coli** (a-c) and **H-AB S. thyp.** (d-f)) and non-functionalized hydrogels (**H-COOH** (g-i)) after incubation in bacteria solution (**E. coli** (a,d and g), **S. thyp** (b,e and h) and **P. putida** (e,f and i)) and washing in PBS (pH = 7.4).

and that the fixed bacteria are not released upon heating. These findings indicate a strong binding between the immobilized **AB E. coli** and **E. coli**.[195]

More in detail, when incubated with **E. coli**, **H-AB E. coli** exhibit a bacteria density of 6027 $cell{\cdot}cm^{-2}$, whereas no bacteria are found with a non-functionalized hydrogel (**H-COOH**). **S. thyp** and **P. putida** show a much weaker affinity with **H-AB E. coli**, which leads to a density of bacteria about 50 and 80 $cell{\cdot}cm^{-2}$. When the anti-body for **S. thyp** is incorporated on the hydrogel surface, attenuated binding can be observed. The density of **S. thyp** on **H-AB S. thyp.** is about 960 $cell{\cdot}cm^{-2}$, whereas in the absence

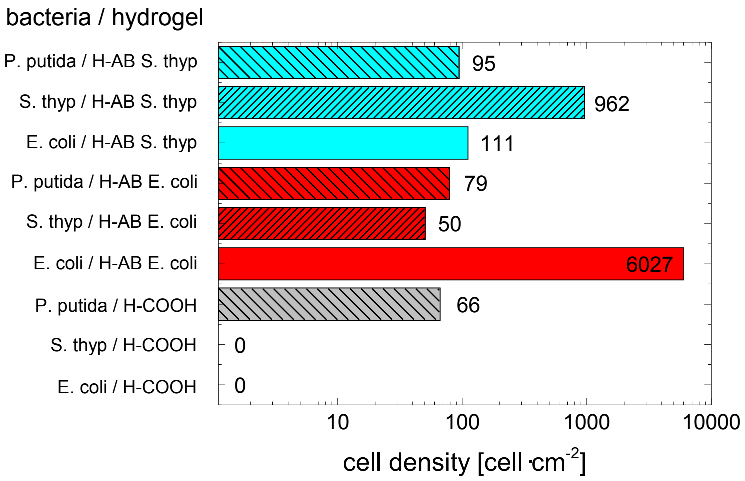

Figure 6.3: Evolution of the bacteria densities of anti-body-functionalized (**H-AB E. coli** and **H-AB S. thyp.**) and non-functionalized hydrogels (**H-COOH**) after incubation in bacteria solution **E. coli**, **S. thyp** and **P. putida** and washing in PBS (pH = 7.4).

of **AB S. thyp**, the bacteria are fully pulled out. Most of the non-specific bacteria (**E. coli** and **P. putida**) are washed out (111 and 95 $cell{\cdot}cm^{-2}$, respectively). **P. putida** shows always a weak affinity to the surface of the hydrogels whether they are functionalized (**H-AB E. coli** and **H-AB S. thyp.**) or not (**H-COOH**). Their density of bacteria are, respectively, 79, 95 and 66 $cell{\cdot}cm^{-2}$.

Note that it is not possible directly to compare **H-AB E. coli** *vs.* **H-AB S. thyp.**, since the concentration of **AB S. thyp** was *ca.* 75 times lower than of **AB E. coli**, due to the high price of **AB S. thyp** (see Chapter 8). Nevertheless, anti-body-functionalized hydrogels seem to exhibit a specific affinity to **E. coli** or **S. thyp**. Therefore, anti-body-functionalized inverse opal hydrogels were also tested in order to see if these attached bacteria were able to induce a shift of the Bragg peak position, even if they can not be expected to penetrate into the structure IOH membrane. For this, the **AB E. coli-E. coli** system was chosen due to high binding efficiency (Figure 6.3).

6.2 Anti-Body – Bacteria as Model Systems for IOH

Bacteria such as **E. coli** can a priori not penetrate into the pores of the IOHs, which exihibit a diameter of around 500 *nm*. Nevertheless, the model system **E. coli** - **AB E. coli** was tested with inverse opal hydrogels since in Section 6.1, high binding affinity between **E. coli** and **AB E. coli** was observed. While anti-body-functionalized inverse opal hydrogels were synthesized according to the procedure described in Section 5.2, their functionalizations were conducted in analogy to the non-structured hydrogels presented in Section 6.1.

After deprotection of the carboxylic acid moieties, the IOH exhibit a strong red-shift of their Bragg peak position. For instance at 25 °C, the reflected wavelength increase from 770 to 939 *nm*. Moreover, the evolution of the Bragg peak shift with the temperature is less pronounced once the carboxylic groups incorporated into the **IOH-COO*t*Bu** are deprotected (**IOH-COOH**). These effects are attributed to the increase of hydrophilicity produced by the carboxylic moieties.

The functionalization by **AB E. coli** of the **IOH-COOH** surface produces only a weak blue-shift of the Bragg peak position from 939 *nm* to 933 *nm*, at 25 °C. This might qualitatively indicate that the functionalization did not work well. Yet, the previous experiment (Section 6.1) shows that bacteria bind to the functionalized hydrogels. Accordingly, the anti-bodies should also be present on the IOH surface. Possibly, their hydrophilicity is too close to the hydrophilicity of the polymer matrix to provoke a notable shrink or expansion.

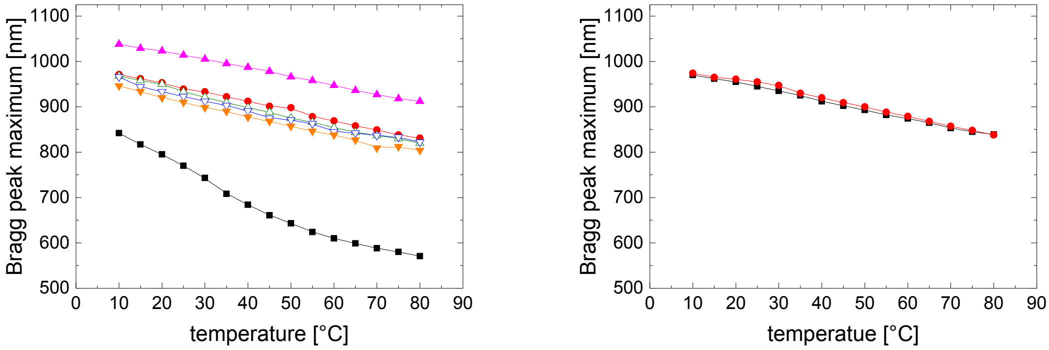

(a) **(b)**

Figure 6.4: Evolution of the position of the Bragg peak maximum of functional inverse opal hydrogel (**IOH-AB E. coli**) and non-functional inverse opal (**IOH-COOH**) with increasing temperature in PBS at pH = 7.4 ; (a) **IOH-COO*t*Bu** (■), deprotected **IOH-COOH** (●), functionalized **IOH-AB E. coli** (△), **IOH-AB E. coli** in presence of **E. coli** before washing (▲), **IOH-AB E. coli** in presence of **E. coli** after washing (▽), **IOH-AB E. coli** in presence of **P. putida** after washing (▼); (b) deprotected **IOH-COOH** in absence (■), and in presence (●) of **E. coli** before washing.

Once the **IOH-AB E. coli** is washed with PBS (pH = 7.4), the Bragg reflection stays almost unchanged (923 *nm* at 25 °C). With the **P. putida** analyte as control, similar observations are made. For instance at 25 °C, the Bragg peak maximum is around 910 *nm*. This seems a priori to indicate that the presence of the **AB E. coli** cannot generate sufficient swelling upon bacteria binding. This is not surprising since the bacteria only interact with the outer surface of the IOH, but not with the inner parts of the porous inverse opal membrane.

Surprisingly, in presence of a high concentrated solution of **E. coli** ($\approx 10^5$ $cell{\cdot}mL^{-1}$), before washing, the **AB E. coli**-functionalized-IOH (**IOH-AB E. coli**) exhibits at 25 °C a red-shift from 933 *nm* to 1014 *nm* of the Bragg peak maximum. This effect is not fully understood yet, since after washing the Bragg peak is shifted back (923 *nm* at 25 °C). Nevertheless, Figure 6.4b suggests that this effect is correlated to the presence of **AB E. coli**. Control **IOH-COOH**, with the same conditions, before washing do not exhibit a comparable red-shift, from 945 to 955 *nm* in the presence of **E. coli** (at 25 °C). One may thus speculate, that the IOH structure is sufficiently deformed by the binding of **E. coli** to generate a signal, although the bacteria cannot enter into the pores.

Note that since the deprotection of the IOH, the intensity of the Bragg peak were extremely low (*Abs.* ≈ 0.005). This is presumably due to an excessive amount of water in the swollen IOH, which reduces the refractive index contrast within the PhC. This contributes to an additional uncertainty concerning the exact Bragg peak position.

The effects seem most interesting, though being rather weak. Clearly, further studies will be needed in order to confirm if the effect observed before washing of **E. coli** is specific, or not.

Obviously, the combination of a systems based on porous IOH, and anti-bodies – bacteria interactions, is questionable. In the cases of benzoboroxole – 1,2-diols, biotin – avidin, or mannose – ConA, strong effects were obtained, due to the good diffusion of the analytes into the IOH (see Chapter 5). This scenario is not possible with bacteria, since their sizes surpass the average pore sizes.

If the local deformations of functionalized PhC surfaces produced by selective interactions with bacteria could indeed induce a Bragg peak shift, then simpler approaches should be also investigated, since pores are no longer necessary. Therefore strategy using non-porous PhCs, such as hydrogels with embedded silica particles (see Figure 1.6

- hybrid material) combined with anti-bodies – bacteria systems may be considered.

Despite these not conclusive experiments, functionalizable non-structure hydrogels, which incorporate carboxylic groups (**H-COOH**) seem a priori to be an attractive platform for the immobilization of anti-bodies. **H-COOH** combines a rather simple and versatile orthogonal functional group, as carboxylic acid, and a thermoresponsive character implemented by the OEG side chains in the matrix. Moreover, such hydrogels mainly made of OEGMA derivatives are expected to be biocompatible, and should show low-fouling properties. Therefore, such IOH systems may definitely have applications in biology, particularly, when specific interactions with bacteria are required, such as for drug delivery systems, or for diagnostic devices.

7 Summary and Conclusion

The aim of this work was the elaboration and the evaluation of hydrogel-based photonic crystals, which are able to detect specifically not only small but also large analytes *via* a simple change of their structural color. For this purpose, stimuli-sensitive inverse opal hydrogels (IOHs) were developed *via* a multi-step method. First spherical monodisperse silica particles were assembled as colloidal crystals (CCs). After polymerization of an embedding hydrogel matrix, and etching of the silica template, replica hydrogels, namely inverse opal hydrogels, were obtained.

In order to obtain selective diagnostic platforms, stimuli-responsive hydrogels were developed, which were made of (oligo ethylene glycol) methacrylate derivatives (OEGMAs) combined with functional recognition units. Such OEGMA derivatives are supposed to be biocompatible and to inhibit the adsorption of non-specific analytes. These polymers could be tailored so that they exhibit a volume phase transition, which is shifted by the binding of a selective analyte, due to a change of the overall hydrophilicity. Analogously, for the appropriately designed IOHs, this selective binding triggered the volume phase transition of the hydrogels. In this way, the recognition process, which is directly translated into a swelling of the hydrogel, could be amplified by the thermoresponsive nature of the OEG chains. Moreover, the OEG-based IOHs exhibit broad volume phase transitions and therefore enabled these systems to be even useful to quantify the analytes.

Various selective recognition units for proton, saccharides, catechols, glycopolymers and proteins were synthesized and incorporated into the polymers matrix, which succeeded to induce a specific color change. Control experiments showed unambiguously that the color changes produced, result from the selective binding the incorporated recognition units and the analytes. Thus it was demonstrated that it is indeed possible to detect even macromolecules qualitatively and quantitatively by simple color changes.

First, the phase transition of analogue non-crosslinked polymers were evaluated *via* turbidimetry. In order to verify the ability of the selected analytes (1,2-diols, avidin, concanavalin A), to induce changes the overall hydrogels hydrophilicity, the cloud point shift of functionalized analogue polymers induced by analyte binding was used as a fast method to evaluate the binding events.

The successful functionalized polymer systems were then transferred to IOHs, which were realized as 10 μm thin CC films made of about 40 layers of assembled silica particles. After polymerization of the surrounding hydrogel matrix and dissolution of the silica template, the free-standing hydrogels exhibited regular internal structure with interconnected pores of ≈ 500 nm diameter. This particular structure enabled even large analytes, such as glycopolymers, or proteins such as avidin and concanavalin A to diffuse into the hydrogel.

For the inverse opal hydrogels (IOHs), analyte binding resulted in a specific and pronounced modulation of their structural colors due to the induced shifts of the optical band gap. This was assessed by measuring the isothermal shift of their diffraction peak (Bragg peak) *via* UV-vis spectrometry, revealing remarkably high signals (up to 150 nm of Bragg peak shift). This and the specific size of the template particles chosen enabled easy detection even by the naked eyes. Typically, hydrophobic analytes provoke a shrinking of IOH, whereas hydrophilic analytes provoke a swelling. Both effects are useful, leading to blue- and, respectively, red-shifts of the Bragg peak position. The success of these new responsive IOHs resides in the combination of a highly structured porosity, a thermoresponsive polymer matrix , and a high binding selectivity between the target analytes and the recognition units incorporated in the polymers.

Moreover, in preliminary experiments, even bigger analyte – recognition systems, such as anti-body – bacteria, were immobilized covalently on the hydrogel as well as inverse opal hydrogel surfaces. These systems showed also selective affinity between the anti-body-functionalized hydrogel surfaces and the appropriate bacteria; these interactions were so strong that they could not be untied by heating. Surprisingly, when these recognition systems were transferred to IOHs, weak but notable effects on the Bragg peak position were observed. The possible response mechanism is not clear. This most attractive aspect, *i.e.* the selective and most simple, direct detection of bacteria, requires further investigations in the future, and if positively confirmed, would represent a major breakthrough in molecular recognition and biosensor devices.

8 Experimental Part

8.1 Chemicals

chemical	formula	purity [*wt.*-%]	CAS	supplier
anti-body **E. coli** K99 Pilus	-	-	ABIN235024	ABO
anti-body **S. thyp** 0-4 (1E6)	-	-	MA-1-22693	ThermoFischer
adrenaline	$C_9H_{13}NO_3$	99	51-43-4	Alfa Aesar
alizarin S	$C_{14}H_7NaO_7S$	99	130-22-3	Fluka
aluminium oxide activity 90 neutral (0.063-0.200 mm / 70-230 mesh ASTM)	Al_2O_3		1344-28-1	Merck
2-aminoethyl methacrylate hydrochloride	$C_6H_{11}O_2N \bullet HCl$	99,5	2420-94-2	Aldrich
aqueous ammonia	NH_3	28-30	7664-41-7	Acros
avidin	-	-		BNLfood
avidin-fluorescein conjugate	-	-		Sigma-Aldrich
2,2'-azobisisobutyronitrile	$C_8H_{12}N_4$	98	78-67-1	Acros
D-biotin	$C_{10}H_{16}N_2O_3S$	99	58-85-5	Iris Biotech
bovine serum albumin	-	-	-	Sigma-Aldrich
CASO-agar	-	-	-	Roth
CASO-media	-	-	-	BD
catechol	$C_6H_6O_2$	99	120-80-9	Riedel-de Haën
catechol-3,5-disulfonic acid disodium salt monohydrate	$C_6H_4Na_2O_8S_2 \bullet H_2O$	97	270573-71-2	Alfa Aesar
concanavalin A	-	-	-	Roth
cis-cyclohexane-1,2-diol	$C_6H_{12}O_2$	98	1792-81-0	Sigma-Aldrich
trans-cyclohexane-1,2-diol	$C_6H_{12}O_2$	98	1460-57-7	Sigma-Aldrich
dextran ($M_n = 70\ kg \cdot mol^{-1}$)	$(C_6H_{10}O_5)_n$	-	9004-54-0	Fluka
di(ethylene glycol) methylether methacrylate	$C_9H_{16}O_4$	95[a]	45103-58-0	Aldrich
dichloromethane	CH_2Cl_2	-	75-09-2	J.T. Baker
N,N'-dicyclohexylcarbodiimide	$C_{13}H_{22}N_2$	99	538-75-0	Fluka
N,N'-diisopropylethylamine	$C_8H_{19}N$	99	7087-68-5	Merck
dimethylformamide	C_3H_7NO	99.9	68-12-2	Merck

chemical	formula	purity [*wt.-%*]	CAS	supplier
1,4-dioxane	$C_4H_8O_2$	99.5	123-91-1	Roth
L-DOPA	$C_9H_{11}NO_4$	95	59-92-7	Cayman Chemical
dopamine hydrochloride	$C_8H_{11}NO_2 \bullet HCl$	99	62-31-7	Alfa Aesar
ethanol	C_2H_6O	99.5	64-17-5	ChemSolute
fructose	$C_6H_{12}O_6$	99	57-48-7	Aldrich
galactose	$C_6H_{12}O_6$	98	59-23-4	Aldrich
glucose	$C_6H_{12}O_6$	99	50-99-7	AppliChem
hydrofluoric acid	HF	10	7667-39-3	ChemSolute
hydrogen peroxide	H_2O_2	30	7722-84-1	Acros
N-hydroxysuccinimid	$C_4H_5NO_3$	97	6066-82-6	Fluka
Irgacure2010	-	-	-	Ciba
LB-agar	-	-	-	Formedium
LB-media	-	-	-	Sigma-Aldrich
maltopentose	$C_{30}H_{52}O_{26}$	95	34620-76-3	Carbosynth
myo-inositol	$C_6H_{12}O_6$	99	87-89-8	Aldrich
scyllo-inositol	$C_6H_{12}O_6$	99	488-59-8	TCI
octane-1,8-diol	$C_8H_{18}O_2$	98	629-41-4	Sigma-Aldrich
oligo(ethylene glycol) dimethacrylate ($M_n = 550\ g \cdot mol^{-1}$)	$C_8H_{10}O_3\text{-}(C_2H_4O)_n$	-[b]	25852-47-5	Aldrich
oligo(ethylene glycol) methylether methacrylate ($M_n = 475\ g \cdot mol^{-1}$)	$C_5H_8O_2\text{-}(C_2H_4O)_n$	-[c]	26915-72-0	Aldrich
pinacol	$C_6H_{14}O_2$	98	76-09-5	Sigma-Aldrich
poly(vinyl alcohol), ($M_w = 31\text{-}50\ kg \cdot mol^{-1}$), 98-99% hydrolyzed	$(C_2H_4O)_n$		9002-89-5	Sigma-Aldrich
potassium carbonate	K_2CO_3	99	584-08-7	Aldrich
propargyl acrylate	$C_6H_6O_2$	98	10477-47-1	Aldrich
ribose	$C_5H_{10}O_5$	98	50-69-1	Alfa Aesar
sorbitol	$C_6H_{14}O_6$	98	50-70-4	Sigma-Aldrich
sulphuric acid	H_2SO_4	98	7664-93-9	ChemSolute
3,5-di-*tert*-butyl-catechol	$C_{14}H_{22}O_2$	98	1020-31-1	Sigma-Aldrich
tetraethyl orthosilicate	$SiC_8H_{20}O_4$	99	78-10-4	Merck
triethylamine	$C_6H_{10}N$	99	121-44-8	Acros
trifluoroacetic acid	$C_2HF_3O_2$	99	76-05-1	Roth
xylitol	$C_5H_{12}O_5$	98	87-99-0	Roth

[a] + 300 *ppm* BHT and 100 *ppm* MEHQ as inhibitors,

[b] + 270-330 *ppm* BHT and 80-120 *ppm* MEHQ as inhibitors,

[c] + 200 *ppm* BHT and 100 *ppm* MEHQ as inhibitors.

8.2 Methods

8.2.1 UV-vis Spectroscopy

UV-spectra were recorded with a Cary 50 UV-Vis spectrophotometer (Agilent, Germany) equipped with a thermoelectric Peltier element for temperature control. Measurements were done with a scan rate of 600 $nm{\cdot}min^{-1}$. Measurements were performed using a demountable quartz cuvette (Hellma Analytics, Germany, 106-QS light path 0.5 mm) to guarantee the strictly perpendicular position of the hydrogel to the laser beam in the spectrometer.

IOHs were incubated in a solution of the presumed binding ligand overnight. 1 h before the measurement, the IOHs were washed six times with ultra-pure H_2O in order to remove unbound ligand. Finally, IOHs were soaked in phosphate-buffered-saline (PBS) solution, to establish a pH value of 7.4. While the samples were heated from 10 $^\circ C$ to 80 $^\circ C$, the transmitted light was measured every 5 $^\circ C$. Figures 3.10, 3.11a, 5.4a, 5.6a, 5.7b, 5.13a and 5.13b were smoothed using OriginPro® (Savitzky-Golay method).

8.2.2 Turbidimetry

Cloud points of the polymers in PBS at pH = 7.4 solutions of 3.0 $g{\cdot}L^{-1}$ were determined in a spectrophotometer Cary 50 UV-Vis spectrophotometer (Agilent, Germany), which was thermostatted *via* a thermoelectric Peltier element. The temperature of the onset of turbidity was taken for the cloud point. Normalized transmittance at 700 nm was monitored as a function of temperature with heating cycles at rates of 1 $K{\cdot}min^{-1}$(cell path length 10 mm).

8.2.3 Dynamic Light Scattering

Sizes of the silica particles were determined with a high performance particle sizer (HPPS, Malvern Instrument, United Kingdom) equipped with a He-Ne laser ($\lambda = 633$ nm) and a thermoelectric Peltier element to control the temperature. The apparatus was operated in backscattering mode at a scattering angle of 173°. Samples were diluted with ultra-pure H_2O to a concentration of 2 $g{\cdot}L^{-1}$ prior to measurements.

Measurements were carried out at 20 °C, averaging over five runs. Size histograms were produced using Malvern ZetaSizer Software using 300 classes between 1 and 1000 *nm*.

8.2.4 Atomic Force Microscopy [1]

The micrographs were recorded with an AFM unit from NT-MDT (Russia) with solver SPM. The AFM has a lateral resolution better than $x, y \approx 50$ *nm* and vertical resolution of $z \approx 0.1$ *nm*. Measurements were carried out in tapping mode using silicon cantilevers from μ-mash Russia (NSG10, 15 *nm* tip radius)

8.2.5 Scanning Electron Microscopy

Opal [2]

The silica opals assembled on a silicon plate were photographed using a Scanning Electron Microscope Zeiss Ultraplus (Zeiss, Germany) at an accelerating voltage of 1 *kV*.

Inverse Opal Hydrogel [3]

The inverse opal hydrogel samples, kept at 25 °C, were frozen in liquid nitrogen (-196 °C) at atmospheric pressure, and subjected to freeze-fracturing in a Gatan Alto 2500 cryo-preparation chamber at -150 °C. Freeze-etching was realized at -98 °C for 45 *s*. After etching, the temperature of the sample was lowered to -130 °C for sputtering with platinum. The sample was transferred into a cryo high resolution-scanning electron microscope S-4800 from Hitachi. The SEM micrographs were obtained at a stage temperature of -145 °C and -100 °C at an accelerating voltage of 2 *kV*.

---

[1] Measurements performed by B. Stiller, University of Potsdam.

[2] Measurements performed by Dr. F. Jaiser, University of Potsdam.

[3] Measurements performed by Dr. B. Tiersch, University of Potsdam.

8.2.6 Laser Scanning Microscopy [4]

The micrographs were recorded with a laser scanning microscope (LSM) 780 (Zeiss, Germany) with the extension wavelength (laser) was 488 *nm* and emission 520 *nm* (+ 20 *nm*) (adjusted by slider). The pictures were taken with a 40× plan Apochromate Objective (1.4 oil, DIC 27).

8.2.7 Optical Microscopy [5]

The micrographs were recorded with a optical microscope in transmission AX71 (Olympus, Germany). The pictures were take with a 40× plan Apochromate Objective (1.4 oil, DIC 27).

8.2.8 Size Exclusion Chromatography [6]

Size exclusion chromatography (SEC) was run at 50 °C in DMF (flow rate 1 $mL{\cdot}min^{-1}$) using a Spectra Physics Instruments apparatus equipped with a UV-detector SEC-3010 and a refractive index detector SEC-3010 from WGE Dr. Bures (columns: guard (7.5 × 75 *mm*), PolarGel-M (7.5 × 300 *mm*)). SEC measurements were calibrated with linear polystyrene standards (PSS, Germany).

8.2.9 NMR Spectroscopy [7]

^{1}H-NMR (300 *MHz*) and ^{13}C-NMR (75 *MHz*) spectra were recorded with a Bruker Avance 300 spectrometer (Bruker, USA). In absence of TMS in addition to the solvent, the solvent peak was used as reference.

---

[4] Measurements performed by Dr. R. Niedl, University of Potsdam.

[5] Measurements performed by Dr. R. Niedl, University of Potsdam.

[6] Measurements performed by S. Stegmann, Fraunhofer IAP.

[7] Measurements performed by A. Krtitschka, University of Potsdam.

8.2.10 Mass Spectrometry [8]

Mass spectra were recorded with a GC-MS Trace DSQ II or ESI-Q-TOFmicro depending on the solubility of the substances.

8.2.11 Elemental Analysis [9]

Elemental analysis were performed with a FlashEA 1112 CHNS/O Automatic Elemental Analyser with 2 Autosampler MAS200R (Thermo Scientific, USA).

8.3 Synthesis of Silica Nanoparticles

Following an analogous method developed by Stöber *et al.*,[47] spherical silica nanoparticles were synthesized. The formulation of particles are presented in Table 8.1.

Monodisperse silica particles were prepared by mixing TEOS (previously distilled) and ethanol in a 500 *mL* round bottom flask. In parallel, NH_4OH (28 *wt.*-%) and ultra-pure H_2O were mixed in a second 500 *mL* round bottom flask. Both solutions were kept at constant temperature for 30 *min* while stirring magnetically (350 *rpm*) with a stir bar (egg-shaped, length 4 *cm*), before the TEOS/ethanol solution was rapidly poured into the aqueous ammonia. While continuously stirring, the mixture was kept at constant temperature overnight. Silica nanoparticles were purified *via* centrifugation (Thermo Scientific, USA, SL 40 FR) for 30 *min* at 4000 *rpm*, and redispersion in ethanol using an ultrasonic bath; this procedure was repeated 6 times. The solid content was determined gravimetrically, indicating a yield of > 95 %.

The monodisperse particles were characterized *via* dynamic light scattering (DLS), see Table 2.2.

---

[8] Measurements performed by S. Früstenberg, University of Potsdam.

[9] Measurements performed by Dr. H. Wetzel, Fraunhofer IAP.

Table 8.1: Type and amounts of the reagents engaged for synthesizing the monodisperse silica particles (**SiO_2-**).

	TEOS[a] $[mol{\cdot}L^{-1}]$ / $[mmol]$ / $[mg]$ /	ethanol[a] $[mol{\cdot}L^{-1}]$ / $[mmol]$ / $[mg]$ /	ultra-pure H_2O[a] $[mol{\cdot}L^{-1}]$ / $[mmol]$ / $[mg]$ /	NH_4OH[a] $[mol{\cdot}L^{-1}]$ / $[mmol]$ / $[mg]$ /	T [°C]	addition velocity $[mL{\cdot}min^{-1}]$
SiO_2-1	0.12 / 24.0 / 5.0	10.75 / 2151.1 / 99.1	13.8 / 1626.0 / 29.2	2.3 / 810.3 / 28.4	30	125
SiO_2-2	0.12 / 24.0 / 5.0	10.75 / 2151.1 / 99.1	13.8 / 1626.0 / 29.3	2.3 / 810.3 / 28.4	30	250
SiO_2-3	0.12 / 24.0 / 5.0	10.75 / 2827.4 / 99.1	13.8 / 654.8 / 11.8	4.3 / 1143.9 / 52.7	30	250
SiO_2-4	0.18 / 36.0 / 7.5	10.75 / 2151.1 / 99.1	13.8 / 654.8 / 11.8	4.3 / 1503.6 / 52.7	30	250
SiO_2-5	0.06 / 12.0 / 2.5	10.75 / 2151.1 / 99.1	13.8 / 654.8 / 11.8	4.3 / 1503.6 / 52.7	30	250
SiO_2-6	0.12 / 24.0 / 5.0	10.75 / 2151.1 / 99.1	13.8 / 654.8 / 11.8	4.3 / 1503.6 / 52.7	40	250
SiO_2-7	0.12 / 24.0 / 5.0	10.75 / 2151.1 / 99.1	13.8 / 654.8 / 11.8	4.3 / 1503.6 / 52.7	50	250

[a] Amount in feed.

8.4 Assembly of Silica Opals

The substrats for the silica deposition, which consist in glass slides were first cleaned and hydrophilized with a cleaning solution of H_2SO_4/H_2O_2 (1:1 v/v). The cleaned glass slides were placed into 25 *mL* beakers containing the silica dispersion (**SiO_2-3**) at the desire concentration of silica (0.5 *wt.*-% to 1.5 *wt.*-%), see Table 3.2. The beakers were stored in a thermostat-controlled chamber (30 °C to 45 °C), until the solvent was evaporated completely (see Table 3.2). The beakers were previously cleaned with a dilute solution of HF (2 *wt.*-%).

Note that **SiO_2-3a** was used in Table 3.2 and Figures 3.7 to 3.11. **IOH-0** was synthesized with **SiO_2-3a**, whereas for **IOH-boroxol**, **IOH-biotin**, **IOH-mannose** and **IOH-COO*t*Bu**, **SiO_2-3b** was used.

8.5 Synthesis of Functional Monomers

8.5.1 Benzoboroxole Methacrylamide

The benzoboroxole functionalized monomer (**boroxol-MAm**) was synthesized by C. Hettrich (Fraunhofer IZI, Potsdam-Golm, Germany) following the procedure by Schumacher and colleagues.[147]

8.5.2 Biotin Methacrylate

The synthesis of the biotin functionalized monomer (**biotin-MA**) in two steps was inspired by the synthesis of Liu *et al.*,[160] and by an analogous monomer reported by Buller *et al.*,[142] giving a colorless product and an improved yield as compared to the previously reported synthesis procedure.[160] First, the intermediate biotinyl-N-hydroxysucinimide ester (**biotin-NHS**) was prepared: Biotin (1.00 *g*, 4.09 *mmol*, 1.0 *eq.*) and NHS (0.47 *g*, 4.09 *mmol*, 1.0 *eq.*) were dissolved in dry DMF (30 *mL*) at 60 °C. N,N'-dicyclohexylcarbodiimide (1.10 *g*, 5.32 *mmol*, 1.3 *eq.*) was added while stirring the solution, and stirring of the mixture was continued overnight at room temperature. The precipitate of N,N'-dicyclohexylurea was filtered off, and washed with DMF. The filtrate was concentrated *in vacuo*, and precipitated into diethyl ether. The precipitate formed was recovered by filtration, washed with cold isopropanol and dried *in vacuo*. A colorless powder was obtained (1.24 *g*, 85%).

In the second step, **biotin-NHS** was converted to biotininyl-2-aminoethyl methacrylate. **biotin-NHS** (1.17 *g*, 3.41 *mmol*, 1.0 *eq.*), 2-aminoethyl methacrylate (0.57 *g*, 3.41 *mmol*) and 2,6-di-*tert*-butyl-4-methylphenol (BHT, 0.08 *g*, 0.34 *mmol*, 0.1 *eq.*) were dissolved in DMF (20 *mL*) at ambient temperature while stirring, and triethylamine

(0.69 *g*, 6.83 *mmol*, 2.0 *eq.*) was added. The reaction mixture was stirred overnight at ambient temperature. The mixture was filtered, the filtrate concentrated *in vacuo*, and precipitated into diethyl ether. The precipitate was recovered by filtration, washed with cold isopropanol and dried *in vacuo*. Biotin methacrylate (**biotin-MA**) was obtained as colorless powder (0.41 *g*, 34%).

^{1}H-NMR (300 *MHz*, DMSO-d6): δ = 7.96 (br, 1H), 6.55-6.25 (m, 2H), 6.06 (s, 1H), 5.68 (m, 1H), 4.31 (dd, J = 7.3, 5.0 *Hz*, 1H), 4.20-4.11 (m, 1H), 4.08 (t, J = 5.6 *Hz*, 2H), 3.17-3.00 (m, 3H), 2.82 (dd, J = 12.4, 5.0 *Hz*, 1H), 2.58 (d, J = 12.3 *Hz*, 1H), 2.07 (t, J = 7.3 *Hz*, 2H), 1.88 (s, 3H), 1.71-1.24 (m, 6H).
^{13}C-NMR (75 *MHz*, DMSO-d6): δ = 173.30, 167.40, 163.61, 136.64, 126.73, 63.94, 61.92, 60.09, 56.25, 38.33, 35.99, 28.99, 28.88, 26.07.

MS (EI): m/z calcd. for $C_{16}H_{25}N_3O_4S$: 355,16; found: signals at 227, 269, 296, 356 $(m+1)^+$.

8.5.3 Mannose Acrylate

The mannose functionalized monomer (**mannose-A**) was synthesized adapting a recipe of Bock *et al.*[196] Propagyl acrylate (0.107 *g*, 0.969 *mmol*, 1 *eq.*), azidomannose (0.375 *g*, 0.969 *mmol*, 1 *eq.*), $(PPh_3)_3CuBr$ (0.090 *g*, 0.097 *mmol*, 10 *mol.*-%) and DIPEA (0.376 *g*, 2.91 *mmol*, 3 *eq.*) were dissolved in dry dichloromethane (3 *mL*). The reaction mixture was stirred overnight at 50 °C bath temperature. After cooling, the mixture was extracted with water, which subsequently was washed by dichloromethane. The organic phases were combined, concentrated and dried *in vacuo*. A yellow-brown oil was obtained (0.232 *g*, 60%), which still contained approximately 10 *mol.*-% of $(PPh_3)_3CuBr$. As the complex proved to be very difficult to remove completely from the monomer, while being readily separable from the polymers, the crude monomer obtained was engaged directly in the copolymerizations, after having verified that the polymerization was not impeded by the residual amounts of the complex.

^{1}H-NMR (300 *MHz*, $CDCl_3$): δ = 7.90 (s, 1H), 6.45 (dd, J = 17.3, 1.2 *Hz*, 1H), 6.17 (dd, J = 5.6, 4.8 *Hz*, 1H), 5.88 (dd, J = 10.4, 1.2 *Hz*, 1H), 5.74–5.65 (m, 1H), 5.42–5.21 (m, 5H), 4.40–4.16 (m, 2H), 4.04–3.91 (m, 1H), 2.14–2.09 (m, 12H).
^{13}C-NMR (75 *MHz*, $CDCl_3$): δ = 171.15, 170.34, 170.12, 169.65, 166.33, 143.03, 132.05, 128.05, 123.81, 84.89, 75.67, 71.06, 69.21, 65.31, 62.46, 54.39, 20.87, 20.80, 20.64, 20.54.

MS (HR-ESI): m/z calcd. for $C_{20}H_{25}N_3O_{11} + H^+$: 484,1567; found: 484,1526 $(m+1)^+$.

8.6 Synthesis of Polymers

The copolymers were synthesized following a common procedure. The amounts of monomers and solvent used for the specific samples are summarized in Table 8.2. In the reaction, AIBN (1 *mol.*-%) and the monomers were dissolved in a given solvent (80 *wt.*-%) in a round bottomed flask, which was sealed by a septum. The reaction mixture was deoxygenated by purging with nitrogen for 30 *min*. Then the mixture was heated to 60 °C and stirred for two days.

Table 8.2: Type and amounts of the reagents engaged for synthesizing copolymers **P-0**, **P-boroxol**, **P-biotin** and **P-mannose-Ac** .

	MEO_2MA^a	$OEGMA475^a$	functional monomer[a]	solvent	yield
	[*mmol*] / [*mg*] / [*mol.*-%]	[*mmol*] / [*mg*] / [*mol.*-%]	[*mmol*] / [*mg*] / [*mol.*-%]	[*mL*]	[%]
P-0	10.63 / 2000 / 92 /	0.920 / 439 / 8 /	-	13.9 (ethanol)	92
P-boroxol	1.640 / 310 / 76	0.252 / 120 / 12	0.346^b / 75^b / 13^b	1.95 (1,4-dioxane)	84
P-biotin	2.184 / 411 / 78	0.336 / 160 / 12	0.280^c / 100^c / 10^c	2.83 (DMF)	93
P-mannose-Ac	1.960 / 369 / 78	0.301 / 143 / 12	0.251^d / 100^d / 10^d	3.1 (ethanol)	83

[a] Amount in feed,
[b] **boroxol-MAm** as functional monomer,
[c] **biotin-MA** as functional monomer,
[d] **mannose-A** as functional monomer.

The reaction was stopped by introducing air into the system and cooling. The mixture was concentrated *in vacuo*, and the crude product was purified by dialysis against water during one week (Roth ZelluTrans membrane, nominal molecular cut off 4000-6000). The polymer was isolated by freeze drying. Yield was determined gravimetrically.

The mannose moiety in copolymer (**P-mannose-Ac**) was deprotected by applying aqueous K_2CO_3 (10 $g{\cdot}L^{-1}$, pH = 10) overnight at room temperature. The thus obtained copolymer was purified by dialysis against water during one week (Roth ZelluTrans membrane, nominal molecular cut off 4000-6000), and recovered by lyophilization.

The polymers were analysed *via* NMR spectroscopy, SEC and turbidimetry (see Table 8.3).

Table 8.3: Type and amounts of the reagents present in copolymers **P-0**, **P-boroxol**, **P-biotin** and **P-mannose**.

	MEO_2MA^a	$OEGMA475^a$	functional monomer^a	$M_n^{app\ b}$ / $M_w^{app\ b}$	CP^c
	[$mol.$-%]	[$mol.$-%]	[$mol.$-%]	[$kg{\cdot}mol^{-1}$]	[°C]
P-0	90	10	-	43 / 203	31.0
P-boroxol	75	11	14^d	28 / 337	28.0
P-biotin	80	10	10^e	48 / 222	35.5
P-mannose	83	15	2^f	27 / 87	39^g / 43.5^h

[a] Molar fraction determined *via* NMR,
[b] Molar mass determined *via* SEC,
[c] Cloud point determined *via* turbidimetry,
[d] **boroxol-MAm** as functional monomer,
[e] **biotin-MA** as functional monomer,
[f] **mannose-A** as functional monomer.
[g] Before deprotection,
[h] After deprotection.

8.7 Synthesis of Hydrogels and Inverse Opal Hydrogels

UV crosslinking was conducted in a UVA-Cube 100 (Hönle, Germany) radiation chamber equipped with a 100 W iron doped mercury vapor lamp, using a glass sheet as filter (cut off 310 *nm*). The distance between the lamp and the samples was about 20 *cm*.

For fabricating the non-structured hydrogels, the polymerizable mixture was typically prepared, as exemplified for **H-0** (see also Table 8.4). MEO_2MA, OEGMA475, OEGDMA550 and Irgacure2010 (2 *mol.-%*) were dissolved in the reaction solvent (1:1 v/v H_2O/ethanol).
The mixture was then injected into a home-made mold, consisting of two hydrophilized glass slide (76 *mm* × 26 *mm*, Carl Roth (Karlsruhe, Germany)), which were separated by a 100 μm thin spacer frame (inner dimensions: 70 *mm*× 20 *mm*) made of Parafilm M (Neehah, USA). The filled and sealed mold (with clamps) was cured at ambient temperature by irradiation with UV-light for 30 *min*. Subsequently, the hydrogel was washed with the reaction solvent (1:1 v/v H_2O/ethanol) for several hours, and then incubated for two days in ultra-pure H_2O with regular H_2O changing (every 12 *h*).

For fabricating the inverse opal hydrogels, the polymerizable mixture was prepared by analogy to unfunctionalized hydrogels (Table 8.4). These mixtures were then injected into a home-made mold, consisting of one hydrophilized glass slide on the top, and one glass slide with a deposition of the silica opal template on the bottom, which were separated by a 100 μm thin spacer frame. The filled and sealed mold (with clamps) was cured at ambient temperature by irradiation with UV-light for 30 min. After washing with reaction solvent for several hours and rinsing with ultrapure water, the silica filled hydrogels were stored in dilute aqueous HF (2 *wt.*-%) for 2 days, to dissolve the silica template particles, thus yielding the inverse opal hydrogel. The IOH was finally cleaned by several washings and a final extraction lasting 2 days in ultra-pure H_2O, replacing the washing water every 12 *h*.

Table 8.4: Type and amounts of the reagents engaged for synthesizing the non structured hydrogels (**H-**) and the inverse opal hydrogels (**IOH-**): **H/IOH-0**, **H/IOH-boroxol**, **H/IOH-biotin**, **H/IOH-mannose** and **H/IOH-COO*t*Bu**.

	MEO$_2$MA[a] [*mmol*] / [*mg*] / [*mol.*-%]	OEGMA475[a] [*mmol*] / [*mg*] / [*mol.*-%]	OEGDMA550[a] [*mmol*] / [*mg*] / [*mol.*-%]	functional monomer[a] [*mmol*] / [*mg*] / [*mol.*-%]	solvent [μL]
H-0a	1.000 / 188 / 80	0 / 0 / 0	0.250 / 326 / 20	-	436 (1:1 v/v H_2O/ethanol)
H-0b	1.000 / 188 / 70	0.143 / 143 / 10	0.286 / 286 / 20	-	552 (1:1 v/v H_2O/ethanol)
H-0c	1.000 / 188 / 60	0.333 / 158 / 20	0.333 / 183 / 20	-	708 (1:1 v/v H_2O/ethanol)
H-0d	1.000 / 188 / 50	0.600 / 285 / 30	0.400 / 220 / 20	-	926 (1:1 v/v H_2O/ethanol)
H-0e	1.000 / 188 / 40	1.000 / 475 / 40	0.500 / 275 / 20	-	1254 (1:1 v/v H_2O/ethanol)
H-0f	1.000 / 188 / 85	0.143 / 68 / 12	0.029 / 16 / 3	-	364 (1:1 v/v H_2O/ethanol)
H-0g	1.000 / 188 / 83	0.143 / 68 / 12	0.060 / 33 / 5	-	386 (1:1 v/v H_2O/ethanol)
H-0h	1.000 / 188 / 79	0.142 / 68 / 11	1.127 / 70 / 10	-	436 (1:1 v/v H_2O/ethanol)
H-0i	1.000 / 188 / 74	0.142 / 68 / 11	0.202 / 111 / 15	-	490 (1:1 v/v H_2O/ethanol)
H-0j	1.000 / 188 / 66	0.143 / 68 / 9	0.381 / 210 / 25	-	622 (1:1 v/v H_2O/ethanol)

	MEO_2MA[a]	OEGMA475[a]	OEGDMA550[a]	functional monomer[a]	solvent
	[*mmol*] / [*mg*] / [*mol.*-%]	[*mmol*] / [*mg*] / [*mol.*-%]	[*mmol*] / [*mg*] / [*mol.*-%]	[*mmol*] / [*mg*] / [*mol.*-%]	[μL]
IOH-0	1.000 / 188 / 68	0.176 / 84 / 12	0.294 / 162 / 20	-	580 (1:1 v/v H_2O/ethanol)
H/IOH-boroxol	1.000 / 188 / 62	0.177 / 85 / 11	0.322 / 177 / 20	0.113[b] / 25[b] / 7[b]	650 (1,4-dioxane)
H/IOH-biotin	1.000 / 188 / 57	0.175 / 83 / 10	0.333 / 183 / 19	0.246[c] / 88[c] / 14[c]	705 (DMF)
H/IOH-mannose	1.000 / 188 / 57	0.175 / 88 / 10	0.333 / 183 / 19	0.246[d] / 98[d] / 14[d]	621 (ethanol)
H/IOH-OEGMA-biotin	-	1.005 / 477 / 67	0.285 / 102 / 19	0.210[c] / 75[c] / 14[c]	871 (DMF)
H/IOH-HEMA-biotin	0.402[e] / 52[e] / 67[e]	-	0.114 / 63 / 19	0.084[c] / 30[c] / 14[c]	193 (DMF)
H/IOH-COO*t*Bu	1.000 / 188 / 57	0.175 / 83 / 10	0.333 / 183 / 19	0.246[f] / 82[f] / 14[f]	720 (ethanol)

[a] Amount in feed,

[b] **boroxol-MAm** as functional monomer,

[c] **biotin-MA** as functional monomer,

[d] **mannose-A** as functional monomer,

[e] HEMA instead of MEO_2MA as hydrophobic monomer,

[f] tri(ethylene glycol) methacrylate *tert*-butylacetate as functional monomer.

In the case of **H/IOH-mannose**, the mannose moiety in copolymer was deprotected by applying aqueous K_2CO_3 (10 $g{\cdot}L^{-1}$, pH = 10) overnight at room temperature. The thus obtained hydrogels and inverse opal hydrogels were washed six times with ultra-pure H_2O, and incubated two more days in ultra-pure H_2O, replacing the washing water every 12 *h*.

In the case of **H/IOH-COO*t*Bu**, the hydrogels and the inverse opal hydrogels were were incubated 3 *h* in trifluoroacetic acid (TFA), in order to cleave the *tert*-butyl protective group, conducting to free carboxylic acid functions. The hydrogels were washed six times with ultra-pure H_2O, and incubated two more days in ultra-pure H_2O, replacing the washing water every 12 *h*. Later, the free carboxylic acid groups of the hydrogel were coupled to **AB E. coli** (4.22 μg) or **AB S. thyp** (0.055 μg) in PBS solution (100 μL) in presence of NHS (0.2 $mol{\cdot}L^{-1}$) and EDC (0.4 $mol{\cdot}L^{-1}$) overnight at room temperature. Finally, the functionalized hydrogels inverse opal hydrolgels were washed six times with PBS, and incubated two more days in PBS, replacing the washing buffer every 12 *h*.

8.8 Preparation of the Cell Cultures [10]

For experimental procedure bacteria strains from *Escherichia coli, Pseudomonas putida* and *Salmonella thyphimurium* were used with a concentration of *ca.* 10^5 $cell \cdot mL^{-1}$. Cell suspensions were prepared as follows:

8.8.1 *Escherichia Coli* and *Pseudomonas Putida*

Wild type strains were cultivated in 25 *mL* of LB-media according to Bertani *et al.*, started from frozen samples until stationary stage.[197] Thereafter by streaking on a LB-agar plate single colonies were isolated at 37 °C for **E. coli** and 30 °C for **P. putida** for 24 *h*. For experimental usage single colonies were picked and cultivated in 25 *mL* of LB-media shaking culture for 6 *h* at 37 °C for **E. coli** and 30 °C for **P. putida**. After 6 *h*, 10 μm of cell suspension was filled up with PBS solution (pH = 7.4) to 1 *mL* total volume and directly used for experiments.

8.8.2 *Salmonella Thyphimurium*

S. thyp attenuation strain was cultivated in 25 *mL* of CASO-media from frozen samples until stationary stage.[198] Thereafter by streaking on a CASO-agar plate single colonies were isolated at 30 °C for 24 *h*. For experimental usage single colonies were picked and cultivated in 25 *mL* of CASO-media shaking culture for 6 *h* at 30 °C. After 6 *h*, 10 μm of cell suspension was filled up with PBS solution (pH = 7.4) to 1 *mL* total volume and directly used for experiments.

---

[10] Preparations performed by Dr. R. Niedl, University of Potsdam.

A NMR Spectra

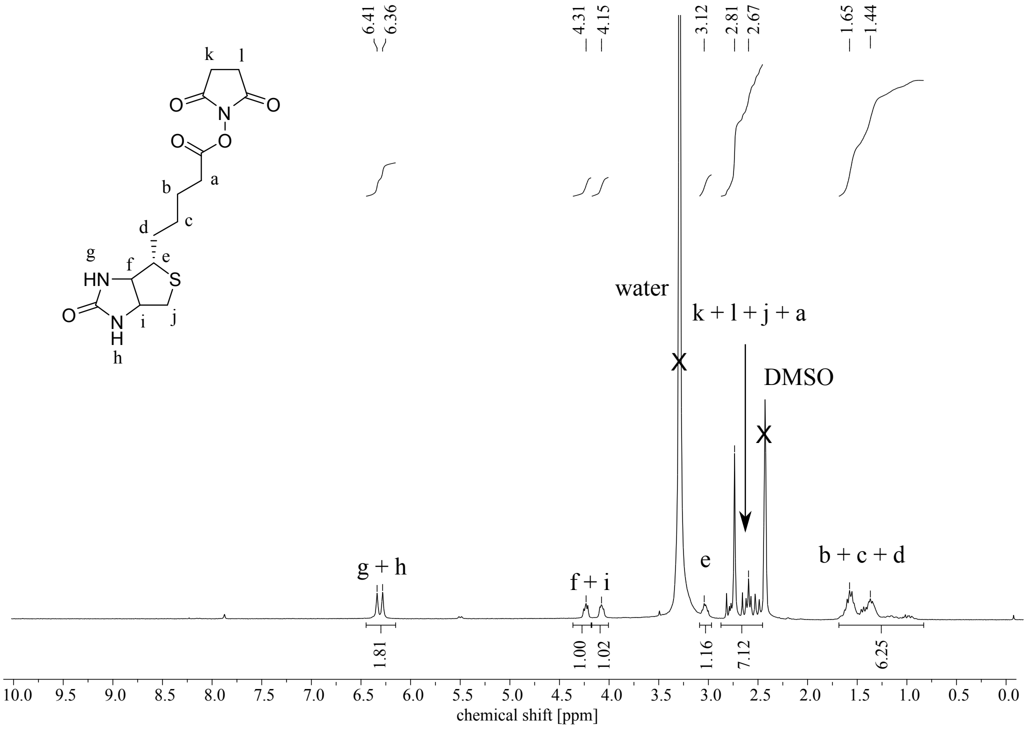

Figure A.1: ^{1}H-NMR spectrum of the intermediate **biotin-NHS** in DMSO-d_6.

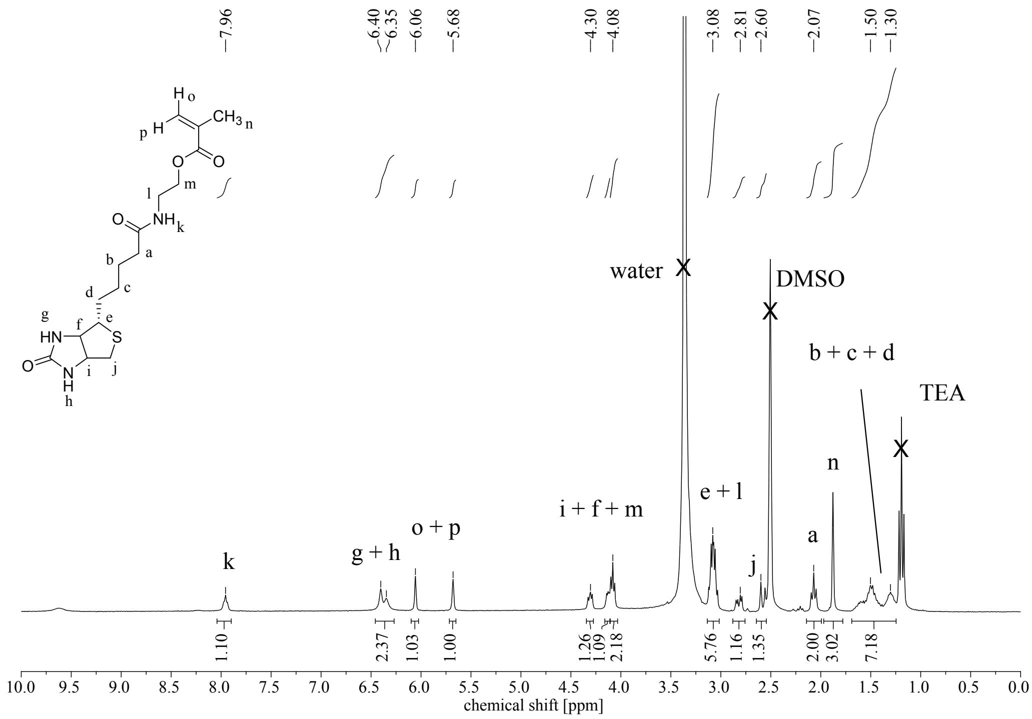

Figure A.2: ^{1}H-NMR spectrum of biotin functionalized monomer **biotin-MA** in DMSO-d$_6$.

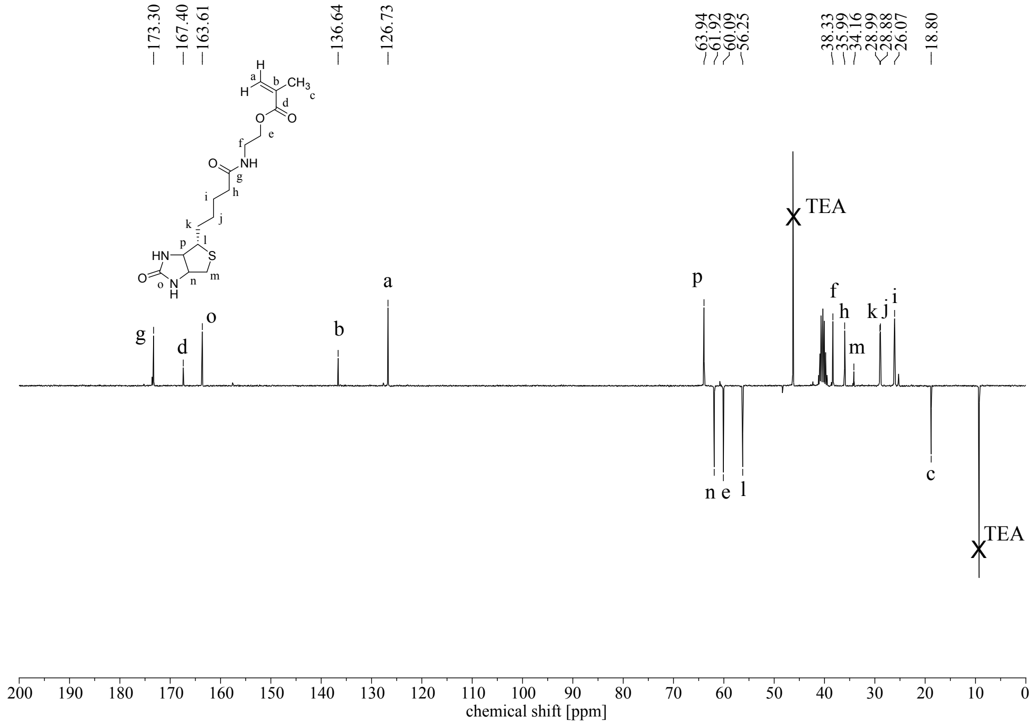

Figure A.3: ^{13}C-NMR (ATP-mode) spectrum of biotin functionalized monomer **biotin-MA** in DMSO-d$_6$.

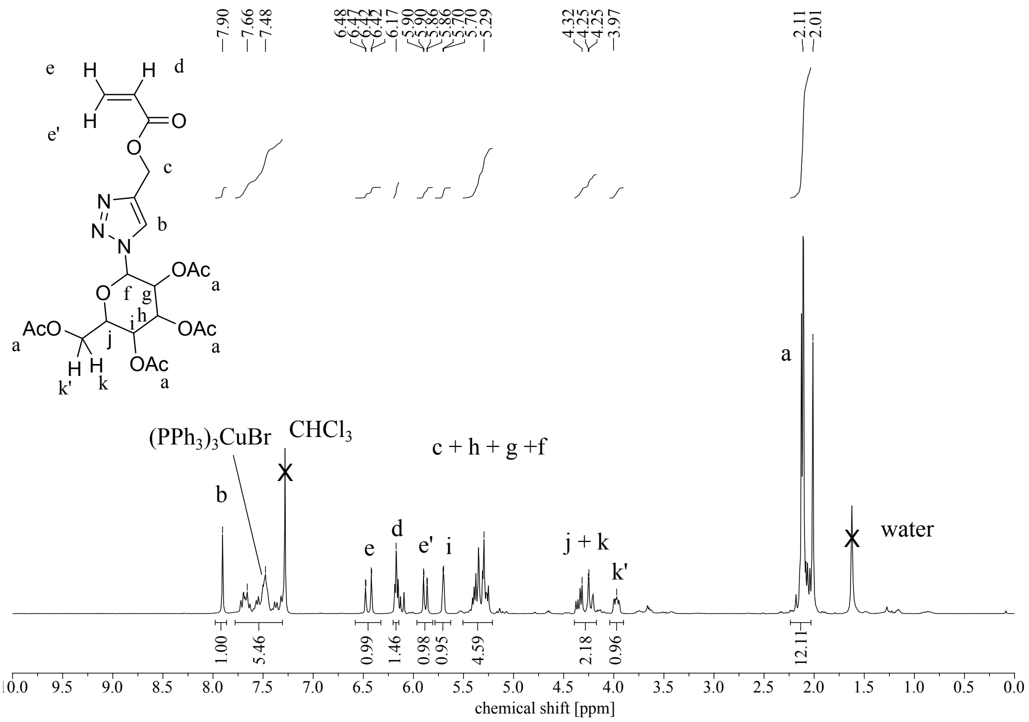

Figure A.4: ^{1}H-NMR spectrum of mannose functionalized monomer **mannose-A** in $CDCl_3$.

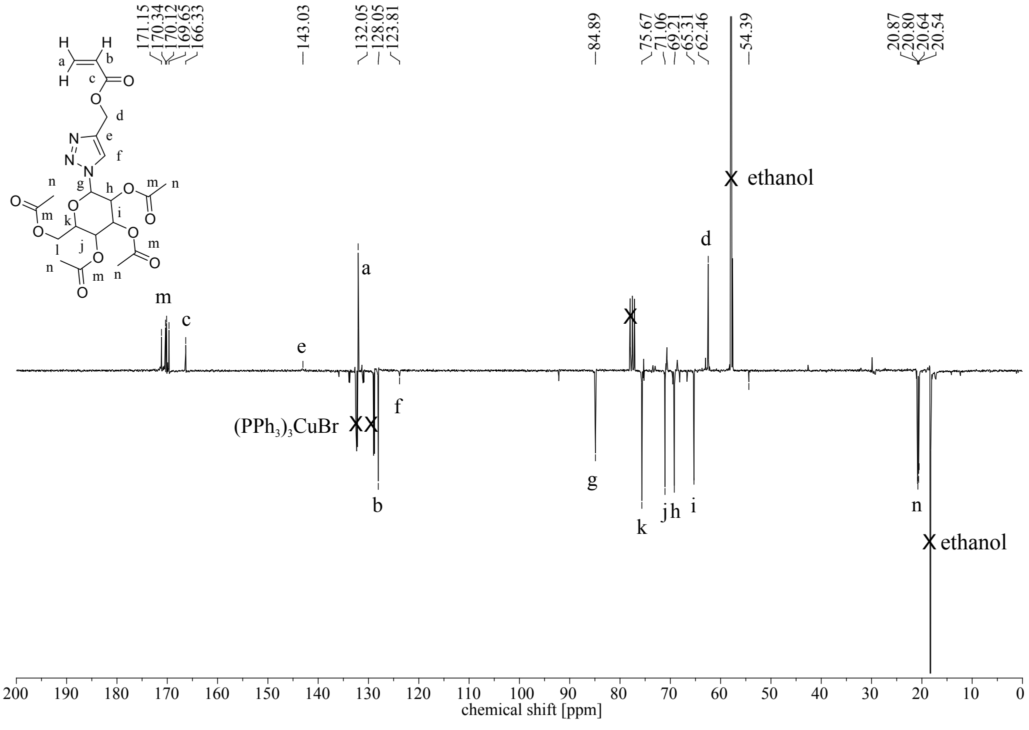

Figure A.5: ^{13}C-NMR (ATP-mode) spectrum of mannose functionalized monomer **mannose-A** in $CDCl_3$.

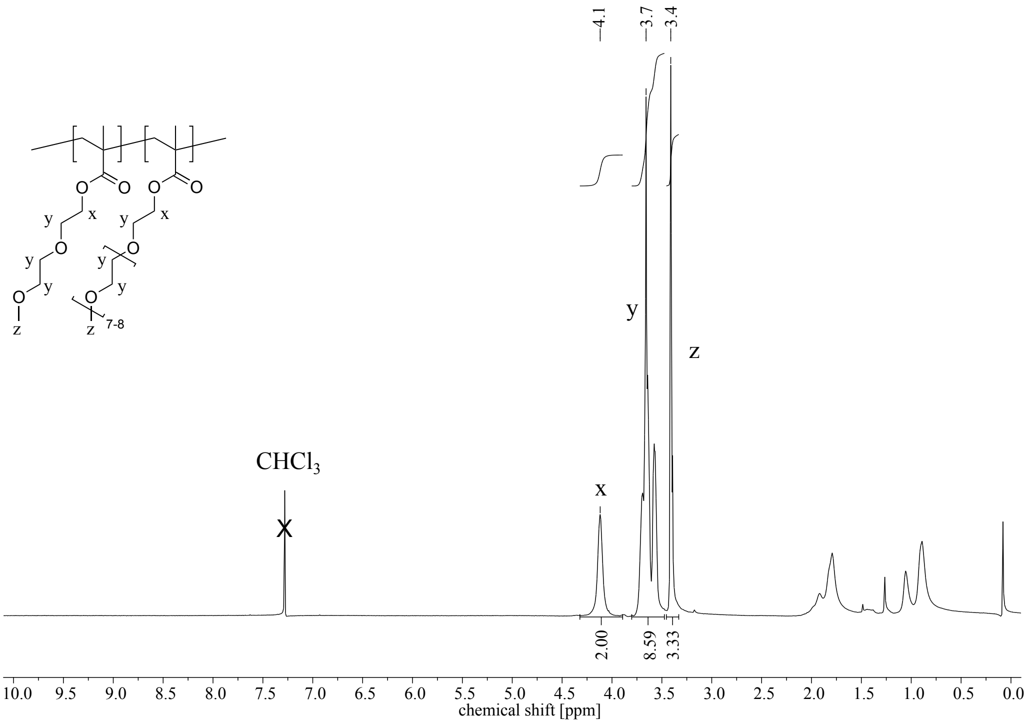

Figure A.6: ^{1}H-NMR spectrum of the reference copolymer **P-0** in $CDCl_3$.

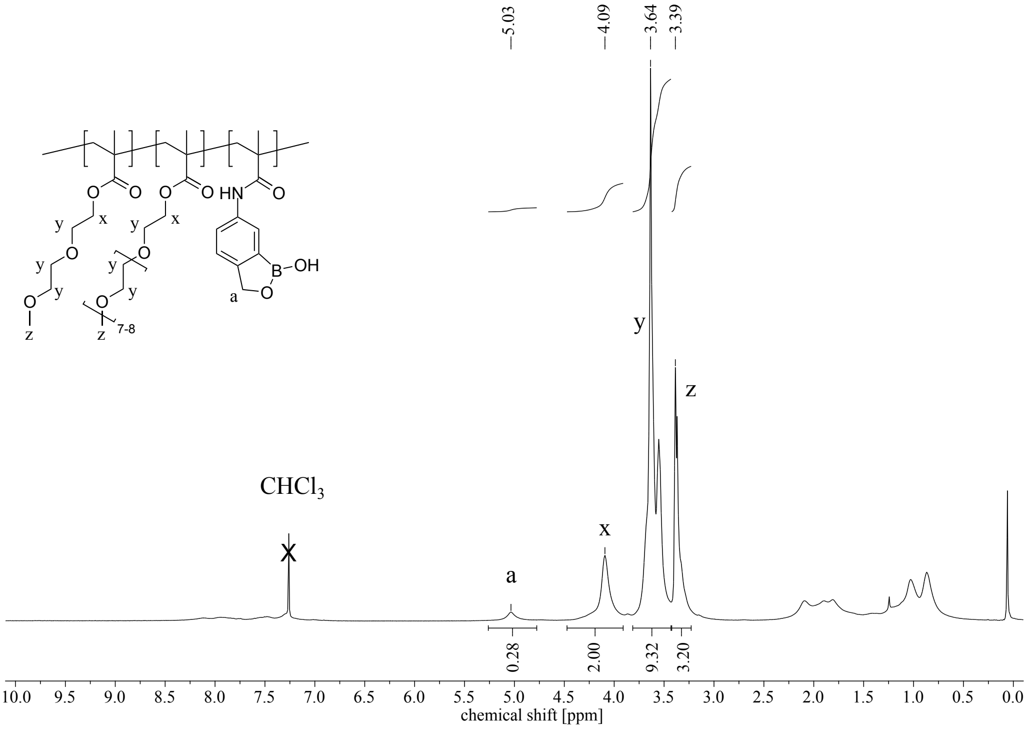

Figure A.7: ^{1}H-NMR spectrum of benzoboroxole functionalized copolymer **P-boroxol** in $CDCl_3$.

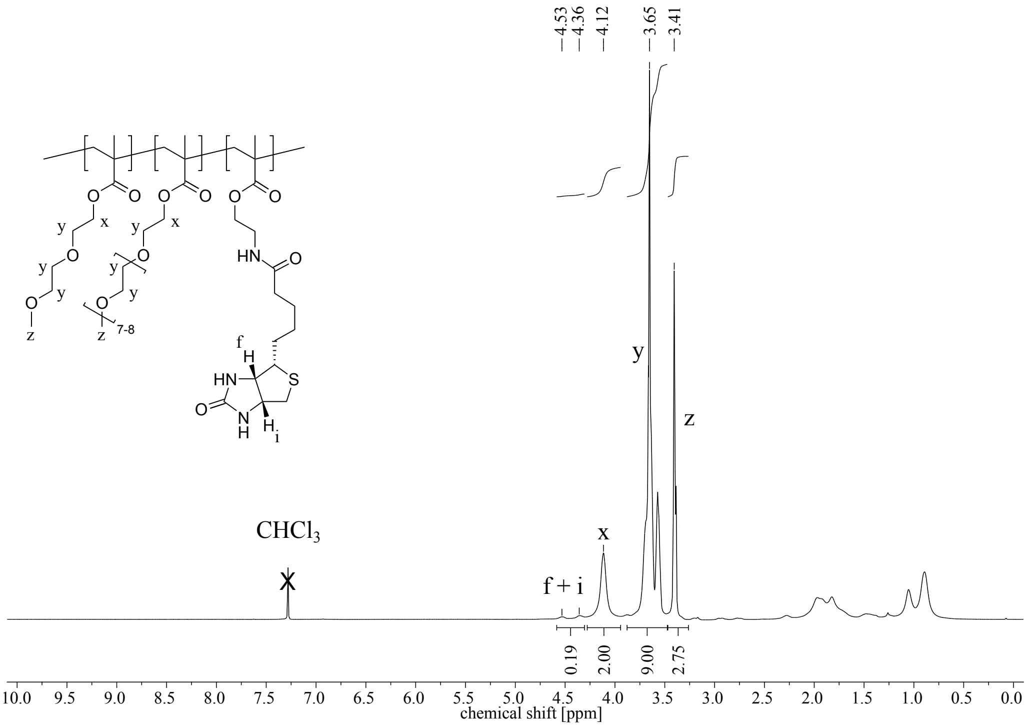

Figure A.8: ^{1}H-NMR spectrum of biotin functionalized copolymer **P-biotin** in CDCl$_3$.

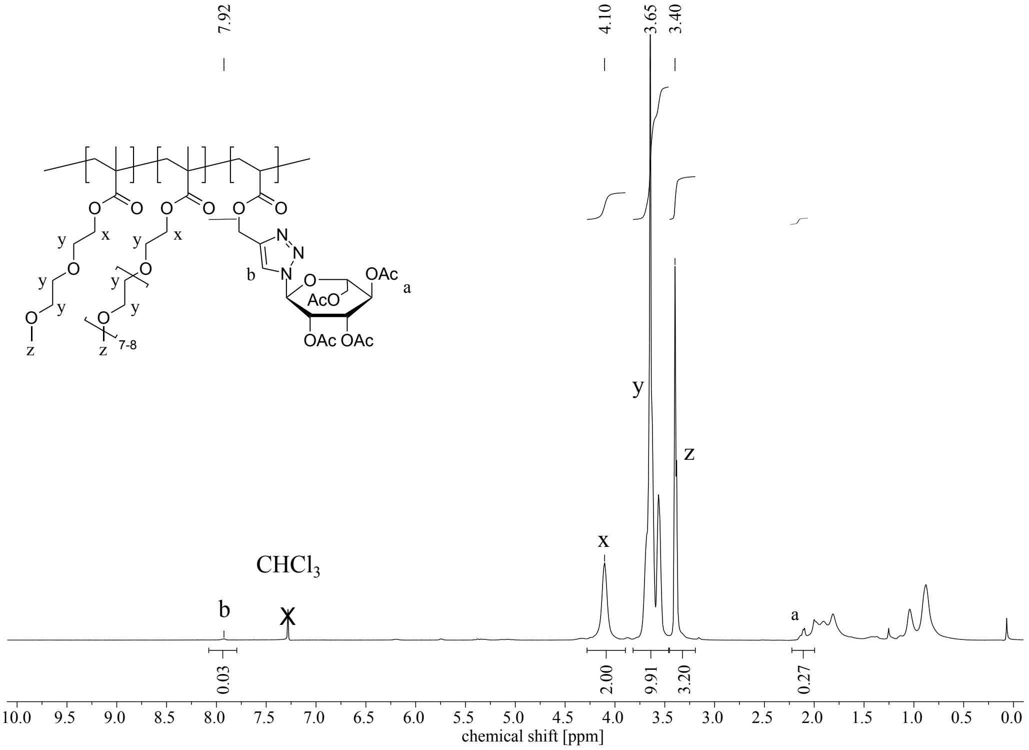

Figure A.9: ^{1}H-NMR spectrum of mannose-Ac functionalized copolymer **P-mannose-Ac** in CDCl$_3$.

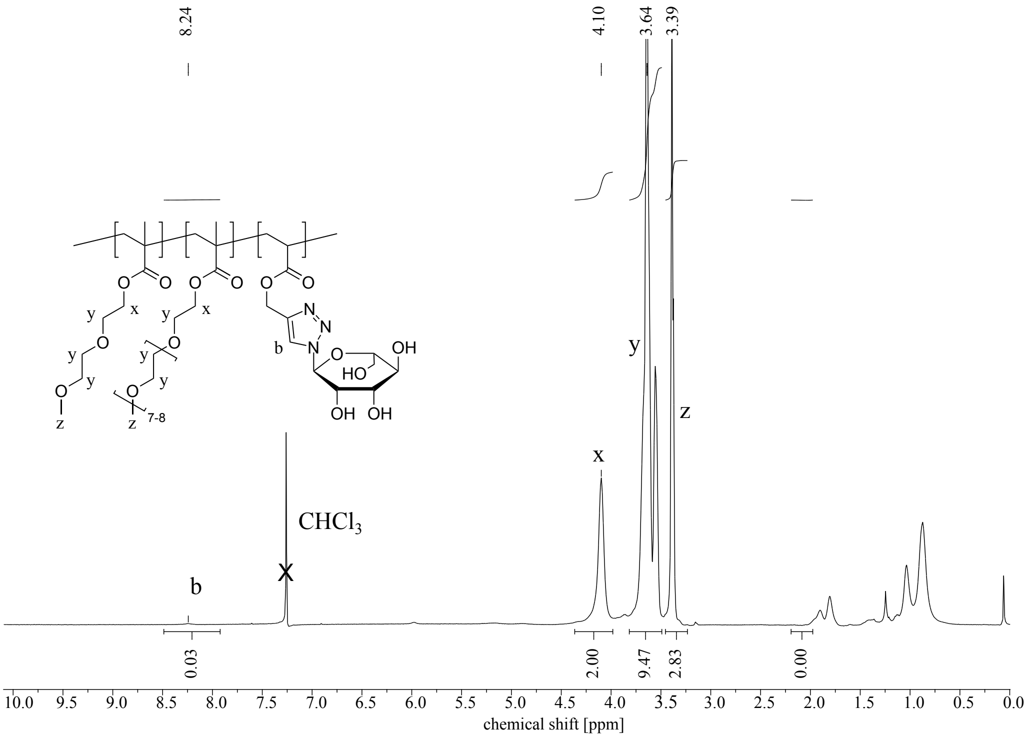

Figure A.10: ^{1}H-NMR spectrum of mannose functionalized copolymer **P-mannose** in $CDCl_3$.

B Solubility Parameters

In order to correlate the Bragg peak positions of **IOH-0** with the solvent "*quality*" (see Section 5.4.1), Hansen solubility parameters of selected organic solvents were compared with molecules with similar structures as OEGMA-hydrogels (Table B.1). Nevertheless, no obvious correlations were found.

Table B.1: Bragg peak positions and intensities of **IOH-0** in selected solvents (see Section 5.4.1).

	n_D^{20} [a] [D]	δ_t [b] [$\mathrm{MPa}^{\frac{1}{2}}$]	δ_d [c] [$\mathrm{MPa}^{\frac{1}{2}}$]	δ_p [d] [$\mathrm{MPa}^{\frac{1}{2}}$]	δ_h [e] [$\mathrm{MPa}^{\frac{1}{2}}$]	λ [f] [nm]	$Abs.$ [g]
diethylene glycol monoethyl ether	-	18.1	16.1	9.2	12.2	-	-
diethylene glycol dimethyl ether	-	18.1	15.7	6.1	6.5	-	-
triethylene glycol	-	27.5	16.0	12.1	18.6	-	-
isopropanol	1.38	23.6	15.8	6.1	16.4	715	0.051
ethanol	1.36	26.5	15.8	8.8	19.4	762	0.029
methanol	1.33	29.6	15.1	12.3	22.3	794	0.037
water	1.33	47.9	15.5	16.0	42.4	816	0.042
acetone	1.36	19.9	15.5	10.4	7.0	838	0.030
DMF	1.43	24.9	14.3	11.9	16.6	913	0.006

[a] refractive index at 20 °C,[199]

[b] total cohesion (solubility) parameter,[125]

[c] dispersion cohesion (solubility) parameter,[125]

[d] polar cohesion (solubility) parameter,[125]

[e] hydrogen bonding cohesion (solubility) parameter,[125]

[f] Bragg peak position at 25 °C,

[g] Bragg peak intensity (in absorbance) at 25 °C.

List of Figures

1.1 Front and oblique views of *Morpho didius* wings in different refractive index media: (a) and (c) in air (n_{air} = 1.00), (b) and (d) in ethanol ($n_{ethanol}$ = 1.36). Perpendicular (e) and parallel (f) view of *Morpho cypris* wings.[5] 2

1.2 Scanning electron micrographs for the cross-section of ground scales of (a) *M. didus*, (b) *M. sulkowskyi*, and (c) *M. rhetenor*, and for a cover scale of (d) *M. adoni*; the bars are (a–c) 1 and (d) 0.5 μm.[8] 3

1.3 (a) black opal photograph by John Cubitto of the Gemological Institute of America, (b) electron micrograph of the surface of a precious opal (after etching by hydrofluoric acid) made of spherically shaped particles ranging from 150 *nm* to 300 *nm* in diameter (magnifition 19,000 ×).[12] 4

1.4 Inverse opal hydrogel pH sensors (a) scanning electron microscope images of an inverse opal hydrogel made of acrylic acid (AcA) and 2-hydroxyethyl methacrylate (HEMA), (b) high-magnification of the same hydrogel showing the interconnected void structure.[20] 5

1.5 Natural species with structural color modulation: (a) the fish *Paracheirodon innesi* displays normally a color of cyan, but after swelling their iridophores, its color changes to yellow,[22] (b) the beetle *Charidotella egregia* changes its color from gold to red after touching its wings, presumably to prevent predation.[23] 6

1.6 Pathway leading to IOHs as autonomous sensor platforms. 8

2.1 Overall reaction of silicon tetrachloride hydrolysis and condensation, in the flame hydrolysis process. 12

2.2 Overall reaction of TEOS hydrolysis and condensation in aqueous media. 14

2.3 Hydrolysis and condensation mechanisms of TEOS in aqueous media under basic conditions.[52] 14

2.4 LaMer diagram of dissolved silicic acid concentration before and after nucleation, with C_N the concentration of silicic acid where the nucleation start, C_0 the concentration of silicic acid where the nucleation stop and C_S the equilibrium of solubility of silicic acid.[60] 17

2.5 Schematic representation of total potential energy *vs.* distance between surfaces in the case of electrostatic (——) and steric (——) stabilization, with V_A attractive van der Waals potential (——) and V_R the repulsive electrostatic potential (——). 19

2.6 Size distribution of the Stöber particles; **SiO$_2$-1** (——), **SiO$_2$-2** (——), **SiO$_2$-3** (——), **SiO$_2$-4** (——), **SiO$_2$-5** (——), **SiO$_2$-6** (——) and **SiO$_2$-7** (——) (see Table 2.1). 24

2.7 Size distribution of the Stöber particles; **SiO$_2$-3a** (——), **SiO$_2$-3b** (——) and **SiO$_2$-3c** (——) (see Table 2.1). 25

3.1 Schematic representation of vertical deposition: a substrate is placed into a dispersion of colloidal particles. 29

3.2 Electron micrographs of two samples with different particles standard deviation (SD_{rel}). The insets show a Fourier transform of $40 \times 40\ \mu m^2$ regions, (a) high regularity, $SD_{rel} = 3.8\%$, (b) low regularity, $SD_{rel} = 14.2\%$. Reproduced from ref. [15]. 30

3.3 Structure of silica opals with fcc lattice, with the planes (111), (220) and (200) marked in grey, and their top-view. 32

3.4 Diffraction of periodical fcc silica opal at the lattice plane (111). 34

3.5 UV-vis reflection (——) and transmission (——) of the plane (111) of a silica opal film. 36

3.6 Illustration of (a) a non-hydrophilized, (b) an hydrophilized glass surface and its influence on the meniscus of the silica solution. 37

3.7 Photographs of the silica colloid deposition **OP-8** at 30° and 80°. 39

3.8 Electron micrograph of silica opal sample **OP-8**, with size particles of 397 ± 2 *nm*, (a-b-c) front view, (d-e-f) face view. 40

3.9 Atomic force micrograph of silica opal sample **OP-8**, with size particles of 387 ± 1 *nm*; (a) topography 10 × 10 μm, (b) topography 3 × 3 μm, (c) 3D representation 3 × 3 μm. 42

3.10 Absorbance of colloidal crystals deposited under different conditions on glass plates. (Table 3.2) 45

3.11 UV-vis analysis of **OP-8** at different incident angles; (a) plots of the absorbance *vs.* wavelength, the diffraction peaks indicated by ↓, ↑ and ← are due to the plane (111), (200)/(-111) and (220), respectively; (b) linearized plot of the Bragg peak position (λ_0^2) of the plane (111) as function of incident angle ($\cos^2(\theta_0)$), with the order of diffraction, $m_{\mathbb{N}} = 1$ 46

4.1 Schematic phase diagram (polymer volume fraction *vs.* temperature): binodal (plain line) and spinodal (dashed line) curves of a polymer solution, exhibiting (a) an upper critical solution temperature (UCST) and (b) a lower critical solution temperature (LCST) 50

4.2 Schematic representation of OEG-bearing thermoresponsive chain below and over LCST-type phase transition temperature. 52

4.3 Molecular structures of various oligo(ethylene glycol) methacrylates (OEGMAs) with the CPs of their homopolymers. Hydrophobic and hydrophilic parts are represented in red and blue, respectively.[127] . . . 54

4.4 Classical thermoresponsive LCST-type polymers with their CPs. From left to right: poly(N-isopropylacrylamide) (P-NiPAm), poly(N-isopropylmethacrylamide) (P-NiPMAm), poly(vinylmethylether) (P-VME), poly(N-vinyl-ε-caprolactam) (P-VCL). 54

4.5 Plots of the measured CPs as a function of the theoretical average number of OEGMA475 units per chain for a series of P-MEO$_2$MA-co-OEGMA475 copolymers of various compositions. Hydrophobic and hydrophilic molecular regions in the copolymer are indicated in red and blue, respectively. Reproduced from [127]. 55

4.6 Schematic presentation of a turbidimetric measurement, (a) situation below and (b) above the phase transition. (c) transmission *vs.* temperature plot of a polymer showing a LCST-type phase transition. 58

4.7 Sensor principle explored in this thesis, based on smart hydrogels functionalized with selective recognition units (red dots): (a) schematic phase diagram in absence (left) and in presence (right) of the analyte, (b) turbidity profile and (c) swelling property change induced by the presence of the corresponding analyte (blue symbol). The green zones in (a) and (b) indicate the temperature range suitable for analyte detection. 60

4.8 Phenyl boronic acid derivatives and benzoboroxoles, from left to right: (a) phenylboronic acid; (b) Wulff-type boronic acids: ortho-dialkylaminomethyl arylboronic acids; (c) 1-hydroxymethyl-phenylboronic acid; (d) benzoboroxole methacrylamide (**boroxol-MAm**); (e) Reaction of a benzoboroxole with 1,2-diol.[145] 62

4.9 Chemical structure of; (a) biotin as anti-avidin; (b) chemically activated biotin; (c) biotin methacrylate (**biotin-MA**) as avidin receptor monomer; (d) Crystal structure of the avidin tetramer showing the subunits in magenta, blue, cyan and red where the four biotin molecules are shown in yellow.[156] 63

4.10 Chemical formula of; (a) acetylated mannose; (b) acetylated azidomannose; (c) acetylated mannose acrylate (**mannose-A**) as concanavalin A recognition monomer. (d) Tetrameric structure of concanavalin A with subunits in red, cyan and green.[171] 64

4.11 Scheme of the radical copolymerization of the binary copolymer **P-0**. . 65

4.12 Scheme of the ternary functional copolymers: **P-boroxol**, **P-biotin** and **P-mannose**. 66

4.13 Plots of the normalized transmittance as a function of the temperature (700 *nm*, 1 $K \cdot min^{-1}$) for aqueous solutions (3 $g \cdot L^{-1}$ in PBS pH = 7.4) of **P-0** (■), **P-boroxol** (●), **P-biotin** (▲), **P-mannose-Ac** (▼) and **P-mannose** (◆). 67

4.14 Thermoresponsive behavior of OEG-derived copolymers in aqueous solutions (3 $g \cdot L^{-1}$in PBS, pH = 7.4) followed by the temperature dependent normalized transmittance at 700 *nm*, and run with rates of 1 $K \cdot min^{-1}$; changes in the heating curves of functionalized **P-boroxol** induced by the addition of selected analytes (1 equivalent relative to the boroxole content, see Table 4.2): (a) no additive (+), *cis*-cyclohexane-1,2-diol (●), *trans*-cyclohexane-1,2-diol (○), scyllo-inositol (▼), myo-inositol (▽), octane-1,8-diol (▲) and pinacol (△); (b) no additive (+), galactose (●), glucose (○), ribose (▼), fructose (▽), sorbitol (▲) and xylitol (△); (c) no additive (+), anthraquinone-2-sulfonic acid (●), PMA (○), dextran (▼), PVA (▽), PXM-1 (▲), PXM-2 (▽) and PXM-3 (×); (d) no additive (+), dopamine (●), adrenaline (○), L-DOPA (▼), catechol-3,5-disulfonic acid (▽), Alizarin S (▲) and 3,5-di-*tert*-butyl catechol (△). 70

4.15 Thermoresponsive behavior of OEG-derived copolymers in aqueous solutions (3 $g \cdot L^{-1}$in PBS, pH = 7.4) followed by the temperature dependent normalized transmittance at 700 *nm*, and run with rates of 1 $K \cdot min^{-1}$; changes in the heating curves of functional **P-0** induced by the addition of selected analytes (1 equivalent relative to the boroxole content in the functionalized analogue **P-boroxol**): no additive (+), Alizarin S (△), PXM-1 (▼). 72

4.16 Thermoresponsive behavior of OEG-derived copolymers in aqueous solutions (3 $g \cdot L^{-1}$in PBS, pH = 7.4) followed by the temperature dependent normalized transmittance at 700 *nm*, and run with rates of 1 $K \cdot min^{-1}$; changes in the heating curves of (a) functionalized **P-biotin** and (b) non-functional **P-0** induced by avidin: (a) 0 $g \cdot L^{-1}$ (+), 0.5 $g \cdot L^{-1}$ (●), 5 $g \cdot L^{-1}$ (△), 10 $g \cdot L^{-1}$ (▼), BSA 50 $g \cdot L^{-1}$ (○); (b) 0 $g \cdot L^{-1}$ (+), 5 $g \cdot L^{-1}$ (●). 73

4.17 Thermoresponsive behavior of OEG-derived copolymers in aqueous solutions (3 $g{\cdot}L^{-1}$in PBS, pH = 7.4) followed by the temperature dependent normalized transmittance at 700 nm, and run with rates of 1 $K{\cdot}min^{-1}$; changes in the heating curves of (a) functionalized **P-mannose-Ac** and **P-mannose** and (b) non-functionalized **P-0** induced by ConA: (a) **P-mannose-Ac** (■), **P-mannose** (+), in presence of 5 $g{\cdot}L^{-1}$ ConA (●), in presence of 10 $g{\cdot}L^{-1}$ ConA (▽); (b) **P-0** (+), in presence of 10 $g{\cdot}L^{-1}$ ConA (●). 74

4.18 Scheme of the radical copolymerization to give the ternary copolymer hydrogel **H-0**. 75

4.19 Scheme of the hydrogel molding process of monomer injection followed by polymerization under UV-light. 76

4.20 Schematic representation of hydrogels (——) with low and high amounts of crosslinker segments (——), ξ being the average mesh size. 77

4.21 Swelling behavior of the P-OEGMA-hydrogels series (**H-0**); (a) Plots of the normalized swelling ratio as function of the temperature in aqueous solutions (PBS pH = 7.4): **H-0a** (■), **H-0b** (●), **H-0c** (▲), **H-0d** (▼), **H-0e** (◆), **H-0i** (◀), **H-0j** (▶); (b) Plot of the swelling ratio at 25 °C as a function of the crosslinker density (**H-0i**, **H-0b** and **H-0j**). 79

4.22 Scheme of the quaternary functional copolymer hydrogels: **H-boroxol**, **H-biotin** and **H-mannose**. 80

4.23 Plots of the normalized swelling ratio as a function of the temperature for aqueous solutions (PBS pH = 7.4) of **H-0** (■), **H-boroxol** (●), **H-biotin** (▲), **H-mannose-Ac** (▼), **H-mannose** (◆). 82

5.1 Scheme of the molding process, *via* monomer infiltration into an opal template followed by polymerization under UV-light. 86

5.2 Schematic representation of the complex structure of IOH, which is composed of a structured opalescent part and a non-structured stabilizing part. 87

5.3 SEM micrographs of a cut through functionalized inverse opal hydrogel **IOH-boroxol**: (a) overview; (b) side view ; (c) detail of the IOH zone, the red hexagons highlighting the basic opal structure; (d) detail as for (c), highlighting the IOH zone near the interface to the bulk hydrogel. . . . 89

5.4 Temperature dependent evolution of the structural color of the non-functionalized sample **IOH-0** (a) and (c)) from 10 to 80 °C in PBS (pH 7.4). Graph (a) shows the evolution of the absorbance spectra, graph (b) the derived Bragg peak's positions; (c) Schematic illustration of a responsive IOH, which exhibits a color change upon exposure to a stimulus. . . . 91

5.5 Photograph of a piece of **IOH-boroxol** swollen (size approx. 5 $mm \times 10$ mm) immersed in water, illuminated by white light from the bottom-left side: (a) at 40 °C; (b) at 45 °C; (c) at 50 °C. 91

5.6 Responsive behavior of inverse opal hydrogel **IOH-0** to selected organic solvents; (a) absorbance spectra of at 25 °C: isopropanol (——), ethanol (——), methanol (——), acetone (——), DMF (——) and PBS (pH = 7.4) as reference (——); (b) position of the Bragg peak maximum of in dependence on the temperature:isopropanol (▼), ethanol (○), methanol (△), acetone (▽), DMF (▲) and PBS (pH = 7.4) as reference (■). 92

5.7 Thermo-responsive and pH-responsive behavior of inverse opal hydrogel **IOH-boroxol** in water; (a) position of the Bragg peak maximum of in dependence on the temperature and pH: pH = 6.0 (▼), pH = 6.8 (▽), pH = 7.4 (●), pH = 8.0 (△), pH = 9.2 (▲); (b) absorbance spectra of at 25 °C modulated by the pH: pH = 6.0 (——), pH = 6.8 (——), pH = 7.4 (——), pH = 8.0 (——), pH = 9.2 (——). 94

5.8 Evolution of the position of the Bragg peak maximum with temperature for the functionalized inverse opal hydrogel **IOH-boroxol** in PBS at pH = 7.4 in the absence (■) and in the presence (50 $mmol\cdot L^{-1}$) of diol analytes: (a) synthetic catechols: Alizatin S (●), catechol-3,5-disulfonic acid (△), pyrocatechol (▽), 3,5-di-*tert*-butyl-catechol (▼); (b) catecholamines: L-DOPA (▽), adrenaline (▲), dopamine (●); (c) saccharides and references: fructose (●), PMA (▲), PVA (▽); (d) glycopolymers: PXM-1 (●), PXM-2 (△), PXM-3 (▼). 96

5.9 Evolution of the position of the Bragg peak maximum of (a,c,d) functionalized **IOH-boroxol** and (b) non-functionalized inverse opal hydrogel **IOH-0** in PBS at pH = 7.4; (a) with increasing concentrations of glycopolymer PXM-1 (content of repeat units) at 37 °C; (b) in absence (■) and in presence (50 $mmol\cdot L^{-1}$) of analyte Alizarin S (●), or PXM-1 (△); (c) before (■) and after adding Alizarin S (●), and after subsequent washing a with solution containing free benzoboroxole(△); (d) induced by the addition of selected analytes at 35 °C. 98

5.10 Fluorescent micrographs of structured inverse opal hydrogel and non-structured hydrogel after incubation with avidin-fluorescein and subsequent washing; top view of (a) **IOH-biotin** and (b) **IOH-0**; side view of (c) **IOH-biotin** and (d) **H-biotin**. The intensities of (b) and (d) were magnified *vs.* (a) and (c). 100

5.11 Evolution of the position of the Bragg peak maximum for (a) functionalized (**IOH-biotin**) and (b) non-functionalized (**IOH-0**) inverse opal hydrogels with temperature in PBS at pH = 7.4, in absence (■) and in presence (0.5 $g\cdot L^{-1}$) of avidin (●). 102

5.12 Evolution of the position of the Bragg peak maximum of functional inverse opal hydrogel (**IOH-biotin**) in PBS at pH = 7.4; with (a) increasing concentrations of avidin at 37 °C; with (b) temperature, before (■) and after adding avidin (●), and after subsequent washing with solution containing free biotin (△). 103

5.13 Evolution of the Bragg peak wavelength at 35 °C for (a) thermoresponsive (**IOH-biotin**) and (b) non-thermoresponsive (**IOH-HEMA-biotin**) inverse opal hydrogels in PBS at pH = 7.4, in absence (——) and in presence (0.5 $g\cdot L^{-1}$) of avidin (——). 103

5.14 Evolution of the position of the Bragg peak maximum for (a) functionalized (**IOH-mannose**) and (b) non-functionalized (**IOH-0**) inverse opal hydrogels with temperature in PBS at pH = 7.4, in absence (■) and in presence (0.5 $g\cdot L^{-1}$) of ConA (●). 105

5.15 Evolution of the position of the Bragg peak maximum of functional inverse opal hydrogel (**IOH-mannose**) in PBS at pH = 7.4 ; with (a) increasing concentrations of ConA at 37 °C; with (b) temperature, before (■) and after adding avidin (●), and after subsequent washing with solution containing free mannose (△). 106

6.1 Scheme of the quaternary functional copolymer hydrogels: protected **H-COO*t*Bu**, deprotected **H-COOH**, anti-body-functionalized **H-AB**. . 108

6.2 Micrographs of anti-body-functionalized (**H-AB E. coli** (a-c) and **H-AB S. thyp.** (d-f)) and non-functionalized hydrogels (**H-COOH** (g-i)) after incubation in bacteria solution (**E. coli** (a,d and g), **S. thyp** (b,e and h) and **P. putida** (e,f and i)) and washing in PBS (pH = 7.4). 109

6.3 Evolution of the bacteria densities of anti-body-functionalized (**H-AB E. coli** and **H-AB S. thyp.**) and non-functionalized hydrogels (**H-COOH**) after incubation in bacteria solution **E. coli**, **S. thyp** and **P. putida** and washing in PBS (pH = 7.4). 110

6.4 Evolution of the position of the Bragg peak maximum of functional inverse opal hydrogel (**IOH-AB E. coli**) and non-functional inverse opal (**IOH-COOH**) with increasing temperature in PBS at pH = 7.4 ; (a) **IOH-COO*t*Bu** (■), deprotected **IOH-COOH** (●), functionalized **IOH-AB E. coli** (△), **IOH-AB E. coli** in presence of **E. coli** before washing (▲), **IOH-AB E. coli** in presence of **E. coli** after washing (▽), **IOH-AB E. coli** in presence of **P. putida** after washing (▼); (b) deprotected **IOH-COOH** in absence (■), and in presence (●) of **E. coli** before washing. 111

A.1 ^{1}H-NMR spectrum of the intermediate **biotin-NHS** in DMSO-d_6. . . . I

A.2 ^{1}H-NMR spectrum of biotin functionalized monomer **biotin-MA** in DMSO-d_6. II

A.3 ^{13}C-NMR (ATP-mode) spectrum of biotin functionalized monomer **biotin-MA** in DMSO-d_6. II

A.4 ^{1}H-NMR spectrum of mannose functionalized monomer **mannose-A** in $CDCl_3$. III

A.5 ^{13}C-NMR (ATP-mode) spectrum of mannose functionalized monomer **mannose-A** in $CDCl_3$. III

A.6 ^{1}H-NMR spectrum of the reference copolymer **P-0** in $CDCl_3$. IV

A.7 ^{1}H-NMR spectrum of benzoboroxole functionalized copolymer **P-boroxol** in $CDCl_3$. IV

A.8 ^{1}H-NMR spectrum of biotin functionalized copolymer **P-biotin** in $CDCl_3$. V

A.9 ^{1}H-NMR spectrum of mannose-Ac functionalized copolymer **P-mannose-Ac** in $CDCl_3$. V

A.10 ^{1}H-NMR spectrum of mannose functionalized copolymer **P-mannose** in $CDCl_3$. VI

List of Tables

2.1 Explored Stöber process parameter. 23

2.2 DLS data of SiO_2 particles. 26

3.1 Characteristic distances and angles of the planes in the fcc lattice. . . . 33

3.2 Vertical deposition of silica particles varying **SiO_2-3** concentration and temperature. 38

4.1 Composition of synthesized linear copolymers **P-**. 66

4.2 Shift of the cloud point (ΔCP) of a solution of **P-boroxol** (3 $g{\cdot}L^{-1}$) in PBS at pH = 7.4, induced by the addition of 1 equivalent (relative to the boroxole content) of a potential diol or polyol analyte. 69

4.3 Composition of hydrogels (**H-0**). 78

4.4 Composition of synthesized hydrogels **H-**. 81

8.1 Type and amounts of the reagents engaged for synthesizing the monodisperse silica particles (**SiO_2-**). 123

8.2 Type and amounts of the reagents engaged for synthesizing copolymers **P-0**, **P-boroxol**, **P-biotin** and **P-mannose-Ac** 126

8.3 Type and amounts of the reagents present in copolymers **P-0**, **P-boroxol**, **P-biotin** and **P-mannose**. 127

8.4 Type and amounts of the reagents engaged for synthesizing the non structured hydrogels (**H-**) and the inverse opal hydrogels (**IOH-**): **H/IOH-0**, **H/IOH-boroxol**, **H/IOH-biotin**, **H/IOH-mannose** and **H/IOH-COO*t*Bu**.129

B.1 Bragg peak positions and intensities of **IOH-0** in selected solvents (see Section 5.4.1). VII

List of Publications

Parts of this Ph.D. thesis were published in scientific journals and were presented in oral presentations as well as on posters at several occasions by the author of this thesis.

Publications and Patents

- Louis. C. Morrill, Lyndsays A. Ledingham, Jean-Philippe Couturier, Jasmine Bickel, Andrew D. Harper, Charlene Fallan Andrew D. Smith, “2-Arylacetic Anhydrides as ammonium enolate precursors”, *Organic & Biomolecular Chemistry* **2014**, *12*, 624–636.
- André Laschewsky, Erik Wischerhoff, Martin Sütterlin, Jean-Philippe Couturier, “Responsive Hydrogel für den Nachweis von Biomolekülen”, patent application PCT/EP2014/077554, **12-12-2014**.
- Jean-Philippe Couturier, Martin Sütterlin, André Laschewsky, Cornelia Hettrich, Erik Wischerhoff, “Responsive Inverse Opal Hydrogels for Sensing Macromolecules”, *Angewandte Chemie International Edition* – very important paper **2015**, *54*, 6641–6644.
- Jean-Philippe Couturier, Erik Wischerhoff, Robert Bernin, Cornelia Hettrich, Joachim Koetz, Martin Sütterlin, Brigitte Tiersch, André Laschewsky “Thermoresponsive Polymers and Inverse Opal Hydrogels for the Detection of Diols”, *Langmuir* – submitted.

Talks

- Jean-Philippe Couturier, André Laschewsky, Martin Sütterlin, Erik Wischerhoff, Cornelia Hettrich, “Inverse Opal Hydrogels for Macromolecules Recognition as a Diagnostic Tool”, *29. Tag der Chemie – Freie Universität Berlin* **2015**.

- Jean-Philippe Couturier, Martin Sütterlin, Erik Wischerhoff, Cornelia Hettrich, André Laschewsky, “Responsive Inverse Opal Hydrogels for Facile Sensing of High Molar Mass Biomolecules”, *4. Berliner Chemie Symposium – Humboldt-Universität zu Berlin* **2015**.

- Jean-Philippe Couturier, Martin Sütterlin, Erik Wischerhoff, Cornelia Hettrich, André Laschewsky, “Responsive Inverse Opal Hydrogels for Facile Sensing of (Bio)Macromolecules”, *Macromolecular Colloquium – Universität Freiburg* **2015**.

- Jean-Philippe Couturier, Robert Niedl, “Responsive Hydrogels for Bacteria Trapping”, *Potsdam Days on Bioanalysis – Fraunhofer IZI-BB - Potsdam-Golm* **2014**.

- Jean-Philippe Couturier, André Laschewsky, Martin Sütterlin, Erik Wischerhoff, Cornelia Hettrich, “New Responsive Inverse Opals for Fast and Facile Sensing of Biomolecules”, *Polydays – Technische Universität Berlin* **2014**.

Posters

- Jean-Philippe Couturier, André Laschewsky, Martin Sütterlin, Erik Wischerhoff, Cornelia Hettrich, “Inverse Opal Hydrogels for Macromolecules Recognition as a Diagnostic Tool”, *29. Tag der Chemie – Freie Universität Berlin* **2015**.

- Jean-Philippe Couturier, Martin Sütterlin, Erik Wischerhoff, Cornelia Hettrich, André Laschewsky, “Responsive Inverse Opal Hydrogels for Facile Sensing of (Bio)Macromolecules”, *Macromolecular Colloquium – Universität Freiburg* **2015**.

- Jean-Philippe Couturier, Martin Sütterlin, Erik Wischerhoff, Cornelia Hettrich, André Laschewsky, “New Responsive Inverse Opal Hydrogels for Sensing Macromolecules”, *Potsdam Days on Bioanalysis – Fraunhofer IZI-BB - Potsdam-Golm* **2014**.

- Jean-Philippe Couturier, Martin Sütterlin, Erik Wischerhoff, Cornelia Hettrich, André Laschewsky, “New Responsive Inverse Opal Hydrogels for Sensing Biomolecules”, *DECHEMA - Kolloquium Spektroskopische Verfahren Für Life Science – Biotechnologiepark - Luckenwalde* **2014**.
- Sandor Dippel, Jens Buller, Jean-Philippe Couturier, Erik Wischerhoff, André Laschewsky, “From monomer synthesis to smart bioconjugable hydrogels”, *Potsdam Days on Bioanalysis – Fraunhofer IZI-BB - Potsdam-Golm* **2013**.

Declaration

I hereby declare that I have made this work by myself using only the referenced materials and sources.

Hiermit erkläre ich, dass ich die vorliegende Arbeit selbstständig angefertigt und keine anderen als die angegebenen Hilfsmittel und Quellen verwendet habe.

Potsdam, 30 Mars 2016 Jean-Philippe Couturier

Bibliography

[1] R. Hooke, *Micrographia*, Martyn J. and Allestry J., London, **1665**.

[2] T. Anderson, *Journal of Applied Physics* **1942**, *13*, 748–758.

[3] K. Gentil, *Zeitschrift für Morphologie und Ökologie der Tiere* **1942**, *38*, 344–355.

[4] A. Parker, *Journal of Optics A: Pure and Applied Optics* **2000**, *2*, R15–R28.

[5] S. Kinoshita, S. Yoshioka, J. Miyazaki, *Reports on Progress in Physics* **2008**, *71*, 076401.1–076401.30.

[6] I. Newton, *Opticks*, Innys W., London, **1730**.

[7] Y. Yin, H.-J. Schneider, M. Shahinpoor, *Responsive photonic nanostructures smart nanoscale optical materials*, Royal Society of Chemistry, Cambridge, **2013**.

[8] S. Kinoshita, S. Yoshioka, *ChemPhysChem* **2005**, *6*, 1442–1459.

[9] A. Eckert, *The world of opals*, John Wiley & Sons, New York, **1997**.

[10] J. Sanders, *Nature* **1964**, *204*, 1151–1153.

[11] P. Darragh, A. Gaskin, B. Terrell, J. Sanders, *Nature* **1966**, *209*, 13–16.

[12] P. Darragh, A. Gaskin, J. Sanders, *Scientific American* **1976**, *234*, 84–95.

[13] J. Jones, J. Sanders, E. Segnit, *Nature* **1964**, *204*, 990–991.

[14] C. Aguirre, E. Reguera, A. Stein, *ACS Applied Materials & Interfaces* **2010**, *2*, 3257–3262.

[15] P. Jiang, J. Bertone, K. Hwang, V. Colvin, *Chemistry of Materials* **1999**, *11*, 2132–2140.

[16] A. Lyon, Z. Meng, N. Singh, C. D. Sorrell, A. St. John, *Chemical Society Reviews* **2009**, *38*, 865–874.

[17] B. Hatton, L. Mishchenko, S. Davis, K. Sandhage, J. Aizenberg, *Proceedings of the National Academy of Sciences* **2010**, *107*, 10354–10359.

[18] Y.-H. Ye, F. LeBlanc, A. Haché, V.-V. Truong, *Applied Physics Letters* **2001**, *78*, 52–54.

[19] L. Goldenberg, J. Wagner, J. Stumpe, B.-R. Paulke, E. Görnitz, *Materials Science and Engineering: C* **2002**, *22*, 405–408.

[20] Y.-J. Lee, P. Braun, *Advanced Materials* **2003**, *15*, 563–566.

[21] J. Lythgoe, J. Shand, *Journal of Experimental Biology* **1989**, *141*, 313–325.

[22] Y. Zhao, Z. Xie, H. Gu, C. Zhu, Z. Gu, *Chemical Society Reviews* **2012**, *41*, 3297–3317.

[23] J.-P. Vigneron, J. Pasteels, D. Windsor, Z. Vértesy, M. Rassart, T. Seldrum, J. Dumont, O. Deparis, V. Lousse, L. Biró, D. Ertz, V. Welch, *Physical Review E* **2007**, *76*, 031907.1–031907.10.

[24] F. Liu, B. Q. Dong, X. H. Liu, Y. M. Zheng, J. Zi, *Optics express* **2009**, *17*, 16183–16191.

[25] E. Gil, S. Hudson, *Progress in Polymer Science* **2004**, *29*, 1173–1222.

[26] D. Roy, J. Cambre, B. Sumerlin, *Progress in Polymer Science* **2010**, *35*, 278–301.

[27] R. Barry, P. Wiltzius, *Langmuir* **2006**, *22*, 1369–1374.

[28] I. Burgess, L. Mishchenko, B. Hatton, M. Kolle, M. Lončar, J. Aizenberg, *Journal of the American Chemical Society* **2011**, *133*, 12430–12432.

[29] M. Hawkeye, M. Brett, *Advanced Functional Materials* **2011**, *21*, 3652–3658.

[30] M. Kumoda, M. Watanabe, Y. Takeoka, *Langmuir* **2006**, *22*, 4403–4407.

[31] S. Asher, A. Sharma, A. Goponenko, M. Ward, *Analytical Chemistry* **2003**, *75*, 1676–1683.

[32] H. Lim, J.-H. Lee, J. Walish, E. Thomas, *ACS Nano* **2012**, *6*, 8933–8939.

[33] J. Shin, P. Braun, W. Lee, *Sensors and Actuators B: Chemical* **2010**, *150*, 183–190.

[34] Y.-J. Lee, S. Pruzinsky, P. Braun, *Langmuir* **2004**, *20*, 3096–3106.

[35] V. Alexeev, *Clinical Chemistry* **2004**, *50*, 2353–2360.

[36] M. Ben-Moshe, V. Alexeev, S. Asher, *Analytical Chemistry* **2006**, *78*, 5149–5157.

[37] J. Walker, S. Asher, *Analytical Chemistry* **2005**, *77*, 1596–1600.

[38] Y. Zhao, X. Zhao, Z. Gu, *Advanced Functional Materials* **2010**, *20*, 2970–2988.

[39] B. Viel, T. Ruhl, G. Hellmann, *Chemistry of Materials* **2007**, *19*, 5673–5679.

[40] C. Fenzl, S. Wilhelm, T. Hirsch, O. Wolfbeis, *ACS Applied Materials & Interfaces* **2013**, *5*, 173–178.

[41] H. Wang, K.-Q. Zhang, *Sensors* **2013**, *13*, 4192–4213.

[42] X. Ma, Y. Cui, X. Zhao, S. Zheng, X. Tang, *Journal of Colloid and Interface Science* **2004**, *276*, 53–59.

[43] E. Wischerhoff, K. Uhlig, A. Lankenau, H. Börner, A. Laschewsky, C. Duschl, J. Lutz, *Angewandte Chemie International Edition* **2008**, *47*, 5666–5668.

[44] D. Roy, W. Brooks, B. Sumerlin, *Chemical Society Reviews* **2013**, *42*, 7214–7243.

[45] M. Sütterlin, PhD thesis, Universität Potsdam, **2014**.

[46] J. Bertone, P. Jiang, K. Hwang, D. Mittleman, V. Colvin, *Physical review letters* **1999**, *83*, 300–303.

[47] W. Stöber, A. Fink, E. Bohn, *Journal of Colloid and Interface Science* **1968**, *26*, 62–69.

[48] H. Bergna in *The colloid chemistry of silica, Vol. 234* (Ed.: H. Bergna), American Chemical Society, Washington DC, **1994**, pp. 1–47.

[49] *Encyclopedia of chemical technology / Kirk-Othmer, Vol. 21: Recycling, oil, to Silicon*, (Eds.: J. Kroschwitz, M. Howe-Grant, R. Kirk, D. F. Othmer), Wiley, New York, 4th ed., **1997**.

[50] *Ullmann's encyclopedia of industrial chemistry., Vol. A 23: Refractory Ceramics to Silicon Carbide*, (Eds.: B. Elvers, F. Ullmann), VCH, Weinheim, 5th ed., **1993**.

[51] A. van Blaaderen, A. Vrij in *The colloid chemistry of silica, Vol. 234* (Ed.: H. Bergna), American Chemical Society, Washington DC, **1994**, pp. 84–111.

[52] J. Brinker, G. Scherer, *Sol-gel science: the physics and chemistry of sol-gel processing*, Academic Press, Boston, **1990**.

[53] R. Iler, *The chemistry of silica: solubility, polymerization, colloid and surface properties, and biochemistry*, Wiley, New York, **1979**.

[54] G. Bogush, C. Zukoski, *Journal of Colloid and Interface Science* **1991**, *142*, 1–18.

[55] T. Matsoukas, E. Gulari, *Journal of Colloid and Interface Science* **1988**, *124*, 252–261.

[56] C. Byers, M. Harris, D. Williams, *Industrial & Engineering Chemistry Research* **1987**, *26*, 1916–1923.

[57] G. Bogush, M. Tracy, C. Zukoski, *Journal of Non-Crystalline Solids* **1988**, *104*, 95–106.

[58] K. Nozawa, H. Gailhanou, L. Raison, P. Panizza, H. Ushiki, E. Sellier, J. Delville, M. Delville, *Langmuir* **2005**, *21*, 1516–1523.

[59] R. Aelion, A. Loebel, F. Eirich, *Journal of the American chemical society* **1950**, *72*, 5705–5712.

[60] V. LaMer, R. Dinegar, *Journal of the American Chemical Society* **1950**, *72*, 4847–4854.

[61] M. Harris, R. Brunson, C. Byers, *Journal of Non-Crystalline Solids* **1990**, *121*, 397–403.

[62] J. Overbeek, *Advances in Colloid and Interface Science* **1982**, *15*, 251–277.

[63] G. Bogush, G. Dickstein, P. Lee, C. Zukoski, *MRS Proceedings* **1988**, *121*, 57–65.

[64] G. Bogush, C. Zukoski in *Ceramic Microstructures ’86* (Eds.: J. Pask, A. Evans), Springer US, Boston, **1987**, pp. 475–483.

[65] J. Feeney, D. Napper, R. Gilbert, *Macromolecules* **1984**, *17*, 2520–2529.

[66] Y. Zeng in *Colloidal dispersions under slit-pore confinement*, Springer, Berlin, Heidelberg, **2012**, pp. 5–21.

[67] J. Koetz, S. Kosmella, *Polyelectrolytes and nanoparticles*, Springer, Berlin, New York, **2007**.

[68] J. Israelachvili, *Intermolecular and surface forces*, Academic Press, London, 2nd ed., **1991**.

[69] L. Allen, E. Matijević, *Journal of Colloid and Interface Science* **1969**, *31*, 287–296.

[70] L. Allen, E. Matijević, *Journal of Colloid and Interface Science* **1970**, *33*, 420–429.

[71] L. Allen, E. Matijević, *Journal of Colloid and Interface Science* **1971**, *35*, 66–76.

[72] R. Horn, D. Smith, W. Haller, *Chemical Physics Letters* **1989**, *162*, 404–408.

[73] G. Peschel, P. Belouschek, M. Müller, M. Müller, R. König, *Colloid and Polymer Science* **1982**, *260*, 444–451.

[74] W. I. Goldburg, *American Journal of Physics* **1999**, *67*, 1152–1160.

[75] W. Schärtl, *Light scattering from polymer solutions and nanoparticle dispersions*, Springer, Berlin, Heidelberg, **2007**.

[76] A. Collins, *Nanotechnology cookbook: practical, reliable and jargon-free experimental procedures*, Elsevier, Boston, Oxford, 1st ed., **2012**.

[77] Y. Xia, B. Gates, Y. Yin, Y. Lu, *Advanced Materials* **2000**, *12*, 693–713.

[78] D. Santamaría Razo, L. Pallavidino, E. Garrone, F. Geobaldo, E. Descrovi, A. Chiodoni, F. Giorgis, *Journal of Nanoparticle Research* **2008**, *10*, 1225–1229.

[79] A. Stein, B. Wilson, S. Rudisill, *Chemical Society Reviews* **2013**, *42*, 2763–2803.

[80] A. Blanco, E. Chomski, S. Grabtchak, M. Ibisate, S. John, S. Leonard, C. Lopez, F. Meseguer, H. Miguez, J. Mondia, G. Ozin, O. Toader, H. van Driel, *Nature* **2000**, *405*, 437–440.

[81] Z.-Z. Gu, A. Fujishima, O. Sato, *Chemistry of Materials* **2002**, *14*, 760–765.

[82] G. Waterhouse, M. Waterland, *Polyhedron* **2007**, *26*, 356–368.

[83] P. Jiang, M. McFarland, *Journal of the American Chemical Society* **2004**, *126*, 13778–13786.

[84] P. Jiang, T. Prasad, M. McFarland, V. Colvin, *Applied Physics Letters* **2006**, *89*, 011908.1–011908.3.

[85] T. Velev, O.and Jede, R. Lobo, A. Lenhoff, *Nature* **1997**, *389*, 447–448.

[86] B. T. Holland, C. F. Blanford, A. Stein, *Science* **1998**, *281*, 538–540.

[87] M. Trau, D. Saville, I. Aksay, *Langmuir* **1997**, *13*, 6375–6381.

[88] M. Holgado, F. Garcia-Santamaria, A. Blanco, M. Ibisate, A. Cintas, H. Miguez, C. Serna, C. Molpeceres, J. Requena, A. Mifsud, F. Meseguer, C. López, *Langmuir* **1999**, *15*, 4701–4704.

[89] A. Rogach, N. Kotov, D. Koktysh, J. Ostrander, G. Ragoisha, *Chemistry of Materials* **2000**, *12*, 2721–2726.

[90] N. Denkov, O. Velev, P. Kralchevsky, I. Ivanov, H. Yoshimura, K. Nagayama, *Nature* **1993**, *361*, 26–26.

[91] E. Adachi, A. Dimitrov, K. Nagayama, *Langmuir* **1995**, *11*, 1057–1060.

[92] S.-L. Kuai, X.-F. Hu, A. Haché, V.-V. Truong, *Journal of Crystal Growth* **2004**, *267*, 317–324.

[93] Z. Zhou, X. Zhao, *Langmuir* **2004**, *20*, 1524–1526.

[94] Y. G. Ko, D. Shin, *The Journal of Physical Chemistry B* **2007**, *111*, 1545–1551.

[95] H. Cong, W. Cao, *Langmuir* **2003**, *19*, 8177–8181.

[96] J.-M. Meijer, F. Hagemans, L. Rossi, D. Byelov, S. Castillo, A. Snigirev, I. Snigireva, A. Philipse, A. Petukhov, *Langmuir* **2012**, *28*, 7631–7638.

[97] A. Hiltner, Y. Papir, I. Krieger, *The Journal of Physical Chemistry* **1971**, *75*, 1881–1886.

[98] A. Ellis, M. Geselbracht, B. Johnson, G. Lisensky, W. Robinson, *Teaching general chemistry: a materials science companion*, American Chemical Society, Washington, **1993**.

[99] E. Yablonovitch, *Physical review letters* **1987**, *58*, 2059–2062.

[100] S. John, *Physical review letters* **1987**, *58*, 2486–2489.

[101] T. Ruhl, P. Spahn, H. Winkler, G. Hellmann, *Macromolecular Chemistry and Physics* **2004**, *205*, 1385–1393.

[102] J. Zhou, J. Wang, Y. Huang, G. Liu, L. Wang, S. Chen, X. Li, D. Wang, Y. Song, L. Jiang, *NPG Asia Materials* **2012**, *4*, e21.1–e21.7.

[103] L. Wang, X. Zhao, *Journal of Physical Chemistry C* **2007**, *111*, 8538–8542.

[104] S. Im, M. Kim, O. Park, *Chemistry of Materials* **2003**, *15*, 1797–1802.

[105] V. Aseyev, H. Tenhu, F. Winnik in *Non-ionic thermoresponsive polymers in water* (Eds.: A. Müller, O. Borisov), Springer, Berlin, **2011**, pp. 29–89.

[106] A. Kumar, A. Srivastava, I. Galaev, B. Mattiasson, *Progress in Polymer Science* **2007**, *32*, 1205–1237.

[107] B. Jeong, A. Gutowska, *Trends in Biotechnology* **2002**, *20*, 305–311.

[108] A. Hoffman, P. Stayton, *Macromolecular Symposia* **2004**, *207*, 139–152.

[109] C. de las Heras Alarcon, S. Pennadam, C. Alexander, *Chemical Society Reviews* **2005**, *34*, 276–285.

[110] M. Gibson, R. O'Reilly, *Chemical Society Reviews* **2013**, *42*, 7204–7213.

[111] M. Ward, T. Georgiou, *Polymers* **2011**, *3*, 1215–1242.

[112] C. Donini, D. Robinson, P. Colombo, F. Giordano, N. Peppas, *International journal of pharmaceutics* **2002**, *245*, 83–91.

[113] A. Kumar, I. Galaev, B. Mattiasson, *Biotechnology and Bioengineering* **1998**, *59*, 695–704.

[114] T. Shimoboji, E. Larenas, T. Fowler, S. Kulkarni, A. Hoffman, P. Stayton, *Proceedings of the National Academy of Sciences* **2002**, *99*, 16592–16596.

[115] A. Lendlein, H. Jiang, O. Jünger, R. Langer, *Nature* **2005**, *434*, 879–882.

[116] G. Filipcsei, J. Feher, M. Zrınyi, *Journal of Molecular Structure* **2000**, *554*, 109–117.

[117] M. Zrınyi, *Colloid & Polymer Science* **2000**, *278*, 98–103.

[118] T. Miyata, N. Asami, T. Uragami, *Nature* **1999**, *399*, 766–769.

[119] T. Miyata, T. Uragami, K. Nakamae, *Advanced drug delivery reviews* **2002**, *54*, 79–98.

[120] A. Bajpai, J. Bajpai, R. Saini, R. Gupta, *Polymer Reviews* **2011**, *51*, 53–97.

[121] A. Kikuchi, T. Okano, *Progress in Polymer Science* **2002**, *27*, 1165–1193.

[122] C. Weber, R. Hoogenboom, U. Schubert, *Progress in Polymer Science* **2012**, *37*, 686–714.

[123] H. Bohidar, *Fundamentals of polymer physics and molecular biophysics*, Cambridge University Press, Delhi, **2015**.

[124] B. Miller-Chou, J. Koenig, *Progress in Polymer Science* **2003**, *28*, 1223–1270.

[125] C. Hansen, *Hansen solubility parameters: a user's handbook*, CRC Press, Boca Raton, 2nd ed., **2007**.

[126] G. Smith, D. Bedrov, *The Journal of Physical Chemistry B* **2003**, *107*, 3095–3097.

[127] J.-F. Lutz, *Journal of Polymer Science Part A: Polymer Chemistry* **2008**, *46*, 3459–3470.

[128] M. Heskins, J. E. Guillet, *Journal of Macromolecular Science: Part A - Chemistry* **1968**, *2*, 1441–1455.

[129] S. Han, M. Hagiwara, T. Ishizone, *Macromolecules* **2003**, *36*, 8312–8319.

[130] M. Ali, H. Stöver, *Macromolecules* **2004**, *37*, 5219–5227.

[131] H. Kitano, T. Hirabayashi, M. Gemmei-Ide, M. Kyogoku, *Macromolecular Chemistry and Physics* **2004**, *205*, 1651–1659.

[132] J.-F. Lutz, O. Akdemir, A. Hoth, *Journal of the American Chemical Society* **2006**, *128*, 13046–13047.

[133] J.-F. Lutz, A. Hoth, *Macromolecules* **2006**, *39*, 893–896.

[134] J. Weiss, A. Li, E. Wischerhoff, A. Laschewsky, *Polymer Chemistry* **2012**, *3*, 352–361.

[135] Y. Bae, S. Lambert, D. Soane, J. Prausnitz, *Macromolecules* **1991**, *24*, 4403–4407.

[136] C. Porsch, S. Hansson, N. Nordgren, E. Malmström, *Polymer Chemistry* **2011**, *2*, 1114–1123.

[137] I. Berndt, C. Popescu, F.-J. Wortmann, W. Richtering, *Angewandte Chemie International Edition* **2006**, *45*, 1081–1085.

[138] K. van Durme, G. van Assche, B. van Mele, *Macromolecules* **2004**, *37*, 9596–9605.

[139] F.-J. Xu, E.-T. Kang, K.-G. Neoh, *Biomaterials* **2006**, *27*, 2787–2797.

[140] H. Schild, D. Tirrell, *The Journal of Physical Chemistry* **1990**, *94*, 4352–4356.

[141] J. Buller, PhD thesis, Universität Potsdam, **2013**.

[142] J. Buller, A. Laschewsky, J.-F. Lutz, E. Wischerhoff, *Polymer Chemistry* **2011**, *2*, 1486–1489.

[143] A. Matsumoto, K. Kataoka, Y. Miyahara, *Polymer Journal* **2014**, *46*, 483–491.

[144] M. Dowlut, D. G. Hall, *Journal of the American Chemical Society* **2006**, *128*, 4226–4227.

[145] M. Bérubé, M. Dowlut, D. Hall, *The Journal of Organic Chemistry* **2008**, *73*, 6471–6479.

[146] G. Wulff, *Pure and Applied Chemistry* **1982**, *54*, 2093–2102.

[147] S. Schumacher, F. Grüneberger, M. Katterle, C. Hettrich, D. Hall, F. Scheller, N. Gajovic-Eichelmann, *Polymer* **2011**, *52*, 2485–2491.

[148] S. Schumacher, M. Katterle, C. Hettrich, B.-R. Paulke, D. Hall, F. Scheller, N. Gajovic-Eichelmann, *Journal of Molecular Recognition* **2011**, *24*, 953–959.

[149] A. Pal, M. Bérubé, D. Hall, *Angewandte Chemie International Edition* **2010**, *49*, 1492–1495.

[150] J. Jay, B. Lai, D. Myszka, A. Mahalingam, K. Langheinrich, D. Katz, P. Kiser, *Molecular Pharmaceutics* **2010**, *7*, 116–129.

[151] V. Alexeev, A. Sharma, A. Goponenko, S. Das, I. Lednev, C. Wilcox, D. Finegold, S. Asher, *Analytical Chemistry* **2003**, *75*, 2316–2323.

[152] S. Asher, V. Alexeev, A. Goponenko, A. Sharma, I. Lednev, C. Wilcox, D. Finegold, *Journal of the American Chemical Society* **2003**, *125*, 3322–3329.

[153] K. Kataoka, H. Miyazaki, M. Bunya, T. Okano, Y. Sakurai, *Journal of the American Chemical Society* **1998**, *120*, 12694–12695.

[154] A. Matsumoto, T. Kurata, D. Shiino, K. Kataoka, *Macromolecules* **2004**, *37*, 1502–1510.

[155] E. Diamandis, T. Christopoulos, *Clinical chemistry* **1991**, *37*, 625–636.

[156] M. Wilchek, E. Bayer, O. Livnah, *Immunology Letters* **2006**, *103*, 27–32.

[157] Y.-Z. You, D. Oupický, *Biomacromolecules* **2007**, *8*, 98–105.

[158] P. Roth, D. Jochum, R. Zentel, P. Theato, *Biomacromolecules* **2010**, *11*, 238–244.

[159] F. Jochum, P. Roth, D. Kessler, P. Theato, *Biomacromolecules* **2010**, *11*, 2432–2439.

[160] Y. Liu, M. Young, O. Moshe, Q. Cheng, R. Hooley, *Angewandte Chemie* **2012**, *124*, 7868–7871.

[161] E. Heydari, J. Buller, E. Wischerhoff, A. Laschewsky, S. Döring, J. Stumpe, *Advanced Optical Materials* **2014**, *2*, 137–141.

[162] J. Becker, G. Reeke, J. Wang, B. Cunningham, G. Edelman, *Journal of Biological Chemistry* **1975**, *250*, 1513–1524.

[163] G. Edelman, B. Cunningham, G. Reeke, J. Becker, M. Waxdal, J. Wang, *Proceedings of the national academy of sciences* **1972**, *69*, 2580–2584.

[164] M. Ambrosi, N. Cameron, B. Davis, *Organic & Biomolecular Chemistry* **2005**, *3*, 1593–1608.

[165] D. Pagé, R. Roy, *Bioorganic & Medicinal Chemistry Letters* **1996**, *6*, 1765–1770.

[166] R. Pieters, *Organic & Biomolecular Chemistry* **2009**, *7*, 2013–2025.

[167] A. Granville, D. Quémener, T. Davis, C. Barner-Kowollik, M. Stenzel, *Macromolecular Symposia* **2007**, *255*, 81–89.

[168] C. Brewer, R. Brown, *Biochemistry* **1979**, *18*, 2555–2562.

[169] J. Geng, J. Lindqvist, G. Mantovani, G. Chen, C. Sayers, G. Clarkson, D. Haddleton, *QSAR & Combinatorial Science* **2007**, *26*, 1220–1228.

[170] L. Su, Y. Zhao, G. Chen, M. Jiang, *Polymer Chemistry* **2012**, *3*, 1560–1566.

[171] V. Srinivas, G. Reddy, N. Ahmad, C. Swaminathan, N. Mitra, A. Surolia, *Biochimica et Biophysica Acta (BBA)-General Subjects* **2001**, *1527*, 102–111.

[172] M. Hetzer, G. Chen, C. Barner-Kowollik, M. Stenzel, *Macromolecular Bioscience* **2010**, *10*, 119–126.

[173] T. Miyata, A. Jikihara, K. Nakamae, A. Hoffman, *Macromolecular Chemistry and Physics* **1996**, *197*, 1135–1146.

[174] J.-T. Zhang, Z. Cai, D. Kwak, X. Liu, S. Asher, *Analytical Chemistry* **2014**, *86*, 9036–9041.

[175] N. Grassie, B. Torrance, J. Fortune, J. Gemmell, *Polymer* **1965**, *6*, 653–658.

[176] G. Springsteen, B. Wang, *Tetrahedron* **2002**, *58*, 5291–5300.

[177] L. Bosch, T. Fyles, T. James, *Tetrahedron* **2004**, *60*, 11175–11190.

[178] J. Buller, A. Laschewsky, E. Wischerhoff, *Soft Matter* **2013**, *9*, 929–937.

[179] X. Ma, X. Huang, L. Zhu, X. Zhao, X. Tang, *Polymer International* **2005**, *54*, 83–89.

[180] X. Ma, J. Xi, X. Zhao, X. Tang, *Journal of Polymer Science Part B: Polymer Physics* **2005**, *43*, 3575–3583.

[181] T. Cai, M. Marquez, Z. Hu, *Langmuir* **2007**, *23*, 8663–8666.

[182] J. Debord, A. Lyon, *The Journal of Physical Chemistry B* **2000**, *104*, 6327–6331.

[183] Z. Hu, X. Lu, J. Gao, *Advanced Materials* **2001**, *13*, 1708–1712.

[184] H. Saito, Y. Takeoka, M. Watanabe, *Chemical Communications* **2003**, 2126–2127.

[185] W. Hong, X. Hu, B. Zhao, F. Zhang, D. Zhang, *Advanced Materials* **2010**, *22*, 5043–5047.

[186] H. Yang, P. Jiang, *Langmuir* **2010**, *26*, 13173–13182.

[187] J. Holtz, S. Asher, *Nature* **1997**, *389*, 829–832.

[188] K. Lee, S. Asher, *Journal of the American Chemical Society* **2000**, *122*, 9534–9537.

[189] Y. Kotsuchibashi, R. Agustin, J.-Y. Lu, D. Hall, R. Narain, *ACS Macro Letters* **2013**, *2*, 260–264.

[190] M. Lin, G. Chen, M. Jiang, *Polymer Chemistry* **2014**, *5*, 234–240.

[191] E. Jeong, C. Park, K. Kim, *Polym. Chem.* **2015**, *6*, 4080–4088.

[192] N. Peppas, H. Moynihan, L. Lucht, *Journal of biomedical materials research* **1985**, *19*, 397–411.

[193] T. Canal, N. Peppas, *Journal of Biomedical Materials Research* **1989**, *23*, 1183–1193.

[194] L. Pugliese, A. Coda, M. Malcovati, M. Bolognesi, *Journal of Molecular Biology* **1993**, *231*, 698–710.

[195] R. Niedl, PhD thesis, Potsdam, **2015**.

[196] V. Bock, H. Hiemstra, J. van Maarseveen, *European Journal of Organic Chemistry* **2006**, *2006*, 51–68.

[197] G. Bertani, *Journal of bacteriology* **1951**, *62*, 293–300.

[198] M. Schaechter, O. MaalØe, N. Kjeldgaard, *Journal of General Microbiology* **1958**, *19*, 592–606.

[199] *CRC handbook of chemistry and physics: a ready-reference book of chemical and physical data,* (Eds.: W. Haynes, D. Lide), CRC Press, Boca Raton, 96th ed., **2015**.